Sede Amministrativa: Università degli Studi di Padova

Dipartimento di Ingegneria Industriale - DII
SCUOLA DI DOTTORATO IN INGEGNERIA INDUSTRIALE
INDIRIZZO: INGEGNERIA DEI MATERIALI
CICLO XXXI

Innovative machining strategies to manufacture biomedical prostheses for improved in-life functional performances

Director of the School: Ch.mo Prof. Paolo Colombo

Coordinator of the School: Ch.mo Prof. Enrico Bernardo

Supervisor of the Thesis: Ch.mo Prof. Stefania Bruschi

Ph.D candidate: Rachele Bertolini

Academic year: 2017-2018

Acknowledgements

I would like to thank Prof. Bruschi and Prof. Ghiotti who gave me the chance to enter in the PhD program, believing in my contributions. I thank them for the support to both my researches and my professional growth.
My sincere thanks to all my colleagues, present and past, for everything they taught me and for their great friendship. A special thanks goes to Marco and Eugenio, who were the best colleagues I could ever hoped to have and to Enrico for always remerber me to be a vessel and not a small boat.
I also thank all the friends who helped me and encouraged me to pursue my goals.
Thanks to Francesca and Bernardetta for the suggestions, laughs and unforgettable moments, and to Katia and Alessandro for being with me since 1990'.
Thanks to Marta and Cristiano, for gave me three special and lovely nephews, and to my favorite brother Matteo.
Thanks to Marco, who has been always by my side even when there was nobody.
The most important thanks goes to my grandmother Assunta, always in my thoughts, for having always supported me.

Abstract

The growing demand of components of higher performances, in terms of reliability and durability, is continuously pushing to find innovative manufacturing methods to realize such components.
Especially in the biomedical field, as a consequence of the raising of population age and consequent increase of the number of revision surgeries, this is a matter of concern, since revision operations are complex and costly for the healthcare, furthermore they cause pain to the patient.
The failure of the biomedical implants is mainly due to excessive wear and corrosion, which leads to implant loosening, and premature failure of the implants inside the biological environment. These phenomena are surface-dependent, since they initiate from the latter.
Efforts have been made by several researchers in the past few decades to investigate the relationships among the machining process parameters, the nature of the surface alterations and their effect on the product functional performances. In the manufacturing scenario, cryogenic machining is emerging as a potential strategy to attain improved functional performance.
Liquid nitrogen is a sustainable, non-toxic, and environmentally-benign means to alternatively cool the surface during machining. Its potential application in the biomedical field is related to the drastic reduction of secondary cleaning processes usually needed to wash off biomedical derived from contamination of flood coolant.
However, the effect of cryogenic cooling on surface integrity, and especially, the link with functional performances is still missing. Therefore, the aim of this study is to evaluate the effect innovative machining strategies, with a particular reference to cryogenic machining, on the functional performances of biomedical products with the aim of improving their durability once placed into the human body.

Sommario

La continua e crescente domanda del mercato volta alla richiesta di prodotti sempre più performanti, è la ragione che motiva la ricerca di tecniche manifatturiere innovative per la realizzazione degli stessi.
Specialmente nel settore biomedicale, ove l'incalzante crescita della popolazione comporta un aumento costante delle operazioni di revisione degli impianti protesici, con conseguente innalzamento del costo della sanità pubblica nonchè del dolore causato al paziente, tale necessità è sempre più urgente. La rottura degli impianti biomedicali è attribuibile a due principali cause, ovvero ad eccessiva usura o allo sviluppo di reazioni di corrosione, che, di conseguenza, comportano la perdita di stabilità dell'impianto causandone, talvolta, una rottura prematura ed inaspettata.
Tali fenomeni sopraindicati sono dipendenti dallo stato della superficie, il quale viene determinato dalle operazioni di manifatturiere di finitura.
Notevoli sforzi sono stati svolti al fine di trovare una relazione tra i parametri di processo, la natura delle alterazioni superficiali e le prestazioni del prodotto in vita di esercizio.
Nell'ambito delle lavorazioni meccaniche, la tornitura criogenica appare come una potenziale strategia per migliorare le caratteristiche della superficie prodotta.
L'azoto liquido è un composto non tossico e totalmente non inquinante utilizzato come mezzo di raffreddamento alternativo durante le operazioni di tornitura. La sua potenziale adozione in ambito biomedicale è legata al fatto che comporta una drastica riduzione dei processi di pulizia usualmente necessari per la rimozione dei residui di oli lubrificanti dai componenti biomedicali. Tuttavia, l'impatto della lavorazione criogenica sull'integrità superficiale, ed in particolare, la relazione che quest'ultima stringe con le prestazioni in vita di esercizio è ancora oggetto di studio da parte dei ricercatori.
L'obiettivo di questo lavoro di ricerca è la valutazione dell'impatto di nuove tecniche innovative di lavorazione, con particolare riferimento alla lavorazione criogenica, sulle prestazioni dei prodotti biomedicali al fine di aumentarne la durabilità all'interno del corpo umano.

Contents

List of Tables

List of Figures

Nomenclature

$3D-VT$ Three Dimensional Vibration Turning

α_1 rake angle

α_2 clereance angle

δ thickness of the deformation zone

γ Shear strain rate

γ' Shear strain

λ Chip compression ratio

ν Coefficiente di Poisson

ACF Autocorrelation Function

AM Additive Manufacturing

AMZ Altered Material Zone

BM Biodegradable metals

$BSED$ Back-Scattered Electron Detector

C_{r} Constraint tool corner radius

CEF Constraint Extrusion Factior

CF Corrosion fatigue

CT Conventional Turning

DoC Depth of cut

DRX Dynamic Recrystallization

E_{corr} Corrosion Potential

EBM Electron Beam Melting

$ECAP$ Equal Channel Angular Process

EIS Electrochemical Impedance Spetroscopy

EIS Electrochemical impedance spectroscopy

EVC Elliptical Vibration Cutting

f feed

FIB Focus Ion Beam

$FUVAT$ Feed Direction Ultrasonic Vibration Assisted Turning

$HSEM$ High Speed Extrusion Machining

I_{corr} Corrosion current density

LN_2 Liquid Nitrogen

$LSEM$ Large Strain Extrusion Machining

MoM Metal on Metal

MoP Metal on Polyethylene

MQL Minumum Quantity Lubrication

OCP Open Circuit Potential

PDP Potentiodynamic polarization

S_{a} Aritmetical mean height

S_{ku} Kurtosis

S_{k} Core roughness depth

S_{pk} Reduced peak height

S_{sk} Skewness

S_{vk} Reduced dale height

SAD Selected Area Diffraction

Sal Autocorrelation length

SBF Simulated Body Fluids

SCC Stress corrosion cracking

SEM Scanning Electron Microscopy

SI Surface Integrity

SPD Severe Plastic Deformed

t_c Controlled chip thickness

t_o Uncontrolled chip thickness

TEM Trasmission Electron Microscopy

THA Total Hip Arthroplasty

UFG Ultra Fined Grained

$UHWMPE$ Ultra High Weight Molecular PolyEthylene

$UNSM$ Ultrasonic Nanocrystal Surface Modification

UVT Ultrasonic Vibration Turning

V_c Cutting speed

XRD X-Ray Diffraction

Part I

Introduction

Chapter 1

Introduction

A growing concern in the aerospace, automotive and biomedical industrial segments of the manufacturing industry is to build in absolute reliability with maximum efficiency of the performance of all machined components.
Especially in the biomedical field, prosthesis with longer duration and reduced inflammatory reactions are needed since the population age is reasing year by year.
The in-life service properties are determined by the state of the surface, which is generated by finishing process, namely the final manufacturing process step. It is therefore of considerable importance to better understand the fundamental relationship between finishing methods and their effect on the in-life service properties.
The functional performance to be optimized depends on the demands placed on product functionalities.
In this work, two materials were took into account, namley titanium and magnesium alloys, and it was made an effort to improve thier performance by optimizing process parameters.
Titanium alloys are widely recognized for their excellent combination of high strength, low density and elevated corrosion resistance; unfortunately, their poor tribological properties limit their applicability in particularly in areas involving wear and friction, such as the biomedical bearing connections.
On the contrary, magnesium alloys are emerging as a novel biodegradable material for temporary internal fixation implants. However, one major limitation preventing the wide application is their unsatisfactory corrosion performance, which are responsible of the premature loss of mechanical properties before the bone have sufficient time to heal.
On these basis, an attempt to improve functional performance of these biomedical material was made.
Emphasis is made in this research work on innovative manufacturing operations, like cryogenic machining, large strain extrusion machining and ultrasonic vibration cutting.

Cryogenic cooling refers to the use of liquid nitrogen as cooling medium during turning. This technique is emerging in the manufacturing scenario, as it is a sustainable, non-toxic, and environmentally-benign means to improve the performance of both manufacturing processes and manufactured products.
It offers the unique opportunity to tailor and precisely engineer the surface/subsurface characteristics of high value components with improved functional performance and product life.
In the context of biomedical engineering, in which the generated product comes in intimate contact with living tissue during service, a key benefit of cryogenic machining is the elimination of secondary cleaning processes usually necessitated to wash off contamination from flood coolant.
For this reason, cryogenic machining is a potential source of costs reduction.
Large strain extrusion machining, is a machining-based approach that combines a simultaneous machining-extrusion operation, thanks to the presence of a constraint across from the tool. It represents an unique way to to obtain a synergistic combination of graded microstructures and high mechanical properties on the workpiece, therefore improving functional properties of the products.
Ultrasonic vibration cutting, is a combined machining method, which changes the material removal mechanism from continuous cutting to intermittent cutting by applying ultrasonic vibration to one or more directions of the tool or workpiece. Compared with conventional cutting, it leads to the reduction of the cutting forces together with an achievement of better surface finishing. Recent years, with ever-growing demand for micro-textured surface processing technology, the ultrasonic vibration turning technique has been used to fabricate microstructures on surfaces, aiming to create surface with unique properties.
On these basis, different innovative manufacturing techniques were used to achieve increased biocompatibility and functional performance in biomedical implants.

1.1 Research objectives

As previously described, innovative manufacturing processes may be used to modify characteristics of the products to a different extent. However, a link between process parameters, surface intergrity and functional performances is greatly needed.
This research is an attempt to address these concerns and its major objectives are:

- Apply innovative manufacturing techniques such as, cryogenic machining, large strain extrusion machining and ultrasonic vibration cutting to manufacture biomedical implants.

Investigate the effect of different process parameters on surface integrity changes such as microstructure, hardness, residual stresses, etc., induced by these manufacturing operations;

- Evaluate the effect of the machining induced surface integrity changes on the functional performances of the products;
- Find the optimized process parameters useful to improve the in-life functional performances for improved durability of biomedical prosthesis.

1.2 Overview of the dissertation

Fig. 1.1 shows how this work is organized in five parts, which in turn are subdivided into ten Chapters.
The first part is the currently Chaper entitled *"Introduction"*, therefore is not included in the flow chart.
The second part *"State of the art"* is composed by two Chapters, namely Chapter two and three. In Chapter two, a literature review is presented. The major experimental studies deal with the effect of machining parameters on surface integrity are presented. In addition, the few availiable studies on the effect of surface integrity induced by machining on fuctional performances were reported.
In chapter three, the biomaterials under investigations on this research work, namely titanium and magnesium alloys, are described. Besides general informations, attention was paid to highlight concerns related to their in vivo functional performances. For titanium alloys, concers are related to its low wear resistance when used as bearing surfaces like in human prosthesis, while in the case of magnesium, the insufficient corrosion resistance into human body environments limits its applicability to a great extent.
The third part *"Materials and methods"* is composed by four Chapters, namely four, five, six and seven. In Chapter four, an overview on the experimental equipments used for carry out machining experiments are presented. In particular, the cryogenic machining experimental setup, the large strain extrusion machining setup and the ultrasonic vibration cutting setup are described in details.
Chapter four summarizes the machining trials used for the biomedical alloys. The effect of machining cooling strategies and number of passes on the wear resistance of acetabular cups, the effects of machining cooling strategies and processing routes on tribocorrosion of dental implants and the effect of cooling strategies and feed on the adesion strenght of a coating, are the case studies relative of titanium alloys.
The effect of machining cooling strategies and feed, the effect of large strain extrusion cutting parameters and the effect of ultrasonic vibration cutting

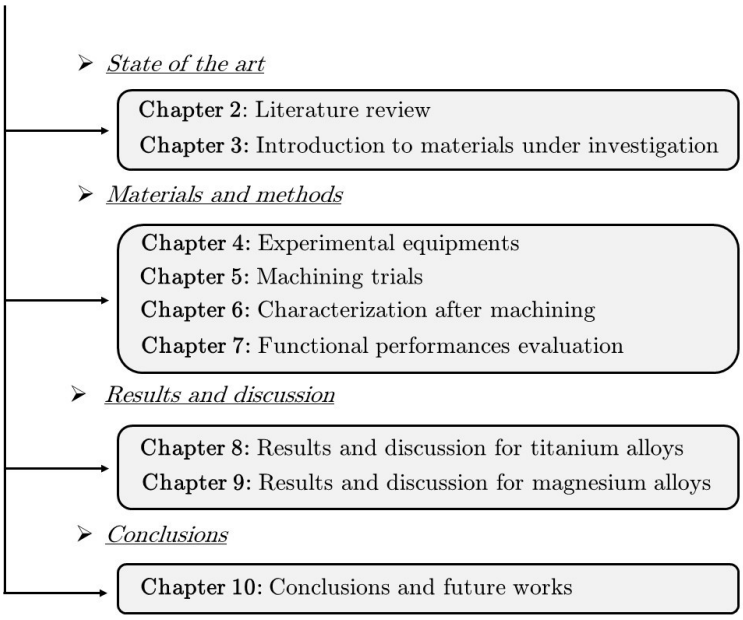

Figure 1.1: Flow chart of this PhD final essay.

parameters on corrosion performances, are the case studies relative of magnesium alloys.
Chapter six, deals with the description of the measurements carried out to assess the surface intergrity of the machined workpiece is reported. These techniques include evaluation of microstructures, residual stresses and nanohardness measurements and surface topography examination.
In Chapter seven, an overview on the techniques used to measure the functional perfomances of the alloys investigated, are presented. Wear tests equipments are described for titanium alloys, while different corrosion tecniques are used for magnesium alloys.
The fourth part *"Results and discussion"* is composed by two Chapters, namely eight and nine. In Chapter eight, experimental results obtained for titanium alloys are reported. The results from these studies provide valuable information for establishing the relationships among machining conditions, surface integrity properties and the wear performance of titanium alloys.
Similarly, in Chapter nine, experimental results for magnesium alloys and the relationship with process parameters and corrosion performances are described.
The fifth part *"Conclusions"* is composed solely by Chapter ten. In Chapter ten, the findings and results of the current work are summarized with final remarks and conclusions.
The directions and recommendations of the future work are discussed briefly based on the results and observations presented in this dissertation.

Part II

State of the art

Chapter 2

Literature review

In this Chapter, the state of the art of machining and its impact on fuctional properties is reported.
The first part deals with the effect of machining, cryogenic machining, large strain extrusion machining and ultrasonic vibration cutting on the surface integrity of the workpiece. This part comprehend also the availible studies which make an attempt into correlate the effect of manufacturing on the service life of the generated products.
The second part deals with the effect of surface integrity induced by manufactuirng on fuctional performances of the two biomaterials under investigation, namely titanium and magnesium alloys.

2.1 The impact of machining on surface integrity

During machining operations, the workpiece material is exposed to thermal, mechanical, and chemical energy that can lead to strain aging and recrystallization of the material. Due to the strain aging process, the material might become harder but less ductile, and recrystallization might cause the material to become less hard but more ductile. These thermal (high temperature and rapid quenching) and mechanical (high stress and strain) effects are the main reasons for the microstructural alterations in the material, as well as

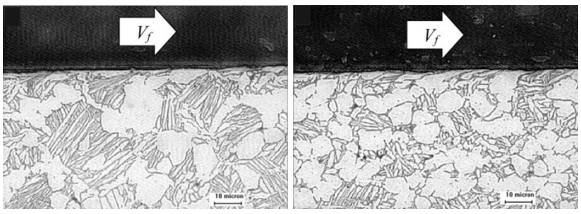

Figure 2.1: Microstructural alterations in Ti-6242S after milling at V_c=100 m/min, f=0.15 mm/tooth, and DoC=2mm (a) at the beginning of machining and (b) after the tool wear of VB=0.3 mm. According to [1].

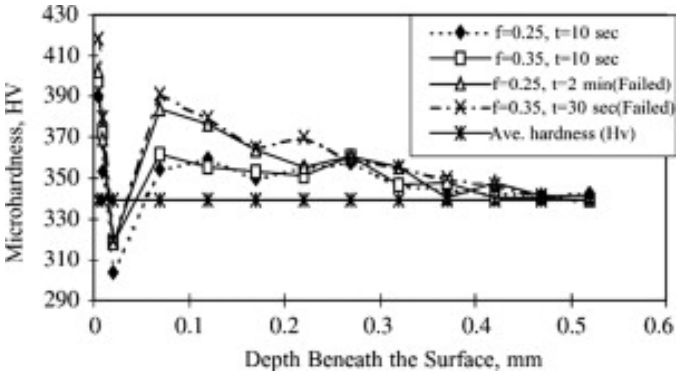

Figure 2.2: The hardness profiles of turned Ti6Al4V at V_c=100 m/min, f=0.25-0.35 mm/rev, and DoC=2 mm. According to [4].

phase transformations and plastic deformations [2].
A very thin layer of plastic deformation was found under the machined layer of a Ti6Al4V alloy in [3]. It was found that the depth of the microstructural alterations is increased when severe cutting parameters were adopted.
Similarly, also the tool wear has a direct relashioship with the altered layer on the workpiece.
Fig. 2.1 shows an example of microstructural alterations in Ti-6242S alloy (used for turbine blade, parts of aeroengine and for replacing some Ti-64-based alloys) before and after milling [1]. After machining, a layer of material deformed along the cutting direction is clearly visible. The surfaces of workpieces are usually created by successive machining passes such as roughing, semi-finishing, and finishing. The characteristics of the machined surface layer created by the proceeding machining passes may have significant influence on the machining performance of the subsequent machining passes.
The hardness under the machined surface is usually higher compared to the one of the bulk material and gradually decrease as a function of the distance from the surface.
In [4], a TiAl64V alloy was machined at cutting speed (V_c)=45-100 m/min, feed (f)=0.25-0.35 mm/rev and depth of cut (DoC)=2 mm. Authors showed that the microhardness values are higher (∼420 HV) than at the bulk material level (∼340 HV), due to the work-hardening effect on the surface and the over-ageing of the sub-surface of the material due to very high cutting temperature (Fig. 2.2). They found that increasing the cutting speed created higher hardness values, while increasing the feed rate had a minimal effect.
Similar results were found for another titanium-based alloy in [5].
After machining processes, the workpiece material is released of the thermo-mechanical load on top of it due to the machining, but not all of the energy can be retrieved. Some of it is spent to plastic deformation, which causes the material to exhibit some stresses, especially at its free ends: the surface.

These stresses that remain in the material after the loading is removed are called residual stresses [6].
Different residual stress results can be found for different workpiece materials and cutting conditions used as well as the differences in tool parameters. In [7] the influence of cutting speed, feed rate and depth of cut on the residual stresses of machined AISI 4340 steel was studied. They showed that peak residual stresses were tensile at low speeds (30 and 60 m/min) for all feed rates, and compressive at high speed (90 m/min) for all feed rates. Peak residual stresses and the depth of stressed region increased with an increase in feed rate and depth of cut, but decreased with an increase in cutting speed.
In [8] a residual stress analysis in orthogonal machining of standard and resulfurized AISI 316L steels was performed. It was showed that increased cutting speed led to larger tensile residual stress on the machined surface but decreased the thickness of the tensile layer. Moreover, the feed rate has a secondary influence on the residual stresses, even if it increases leads to an enhancement of the compressive stress values in the subsurface and to the thickness of the tensile layer. They claimed that it was due to a mechanical effect caused by the augmentation of the compressive zone in the region of the workpiece situated below the cutting edge, leading to greater elastic relaxation after machining.
In general, the measurements of residual stresses is very difficult and thus leads to very different kind of results in literature.
On the contrary, the cutting tool parameters, the wear of the tool, the cutting speed, the feed rate and the depth of cut have a strong influence on the surface roughness induced by manufacturing process.
Feed rate was declared to be the most dominant parameter to affect the surface roughness in machining Inconel 718 at V=30-125 m/min, f=0.075-0.6 mm/rev, and DoC=0.5-2 mm: as feed increased, surface quality was lowered [9]. Similarly, as cutting speed increases lower is the surface quality achieved [4] (see Fig. 2.3).
Unambiguous trend was found for the depth of cut, since when it was increased, surface quality lowered in [9], while in other cases (other materials and cutting conditions), depth of cut does not have a significant effect on surface roughness [1].
In a general sense, it can be said that the surface roughness is strictly conditioned by the material and the parameter adopted. It can be generally postulated that when the process material removal rate decreases the surface quality of the part was observed to be better, and the surface roughness values decreased.

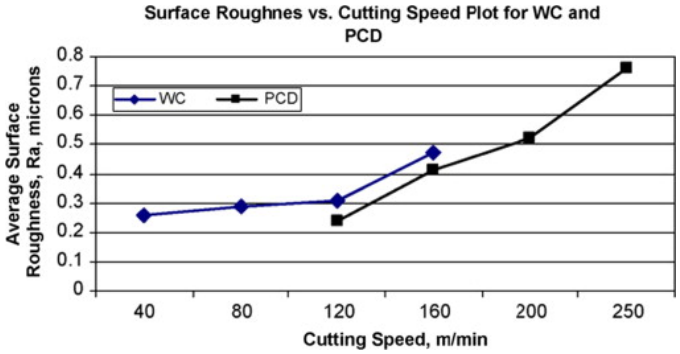

Figure 2.3: Average surface roughness values as a function of the cutting speed for Ti6Al4V at V=40-160 m/min, f=0.1 mm/tooth, DoC=1 mm, according to [10].

2.2 The impact of cryogenic machining on surface integrity

Cryogenic machining is an innovative method of cooling the cutting tool and/or workpiece during material removal processes. The coolant is nitrogen fluid (LN_2) that is liquefied by cooling to $-196°C$.
Nitrogen is a safe, non-combustible, and noncorrosive gas.
In fact, 78% of the air we breathe is nitrogen.
The liquid nitrogen in a cryogenic machining system quickly evaporates and returns to the atmosphere, leaving no residue to contaminate the workpiece, chips, machine tool, or operator, thus eliminating disposal costs.
Additionally, cryogenic machining can be used to machine work materials at higher cutting speeds, and to achieve higher surface quality and better surface integrity, with increased machinability and reduced overall costs.
Proven benefits of cryogenic machining are:

- improved process sustainability (cleaner and safer, environmentally-friendly processes providing no adverse health effects for personnel on the shop floor);
- increased material removal rate (MRR) with no increase in tool-wear rates and tool change time, resulting in reduced over all costs via higher productivity;
- higher tool-life due to lower abrasion and chemical wear;
- enhanced surface integrity through controllable microstructural and phase changes with more favorable dynamic recrystallization and corrosion and wear resistance.

However, even if it is generally recognized that cryogenic leads to improved surface integrity, more detailed researchs are needed.

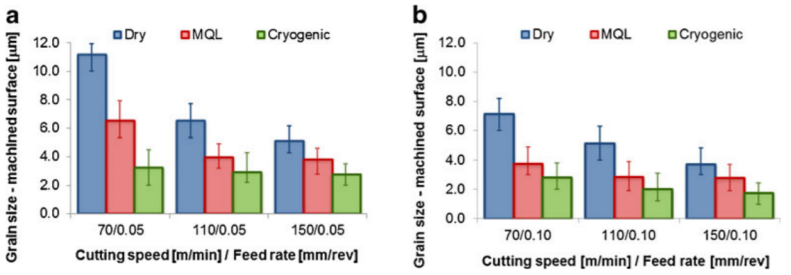

(a) *Comparison of measured grain size variation at varying the cutting speed and a feed of 0.05 mm/rev.*

(b) *Comparison of measured grain size variation at varying the cutting speed and a feed of 0.1 mm/rev.*

Figure 2.4: Comparison between the grain size obtained after machining with different process parameters, according to [11].

Cryogenic process has been reported to successfully introduce thicker surface layers consisting of ultrafine/nano-grain structures.
The effect of dry, minimal quality lubrication (MQL), and cryogenic cooling conditions using coated tools at varying cutting speeds and feed rates on surface integrity of Ti6Al4V alloy was studied in [11]. The grain size as a function of process parameters is reported on Fig. 2.4. The achievement of smaller grains when using cryogenic cooling conditions is related to the fact that this cooling process prevents grain growth after the dynamic recrystallization (DRX), which in turn is the result of the severe plastic deformation process.

The effects of cryogenic cooling on surface integrity in hard machining of AISI 52100 and compare the performance with dry machining at varying process parameters were evaluated in [12]. The white layer formation was drastically reduced by cryogenic cooling compared to the dry condition, since the higher temperatures generated in the machining zone should lead to localized thermal softening of the workpiece material temperature exceeds the austenitizing temperature for subsequent quenching through self-cooling.
A remarkable grain refinement in cryogenic machining of low alloy steel AISI 4140 was found in [13]. The influenced surface layer was 3.2 mm thick for cryogenic condition compared to 2.2 mm under dry machining.
Strictly correlated with microstructures is the hardness of the machined workpiece: in general, hardened surfaces are obtained when cryogenic cooling is applied.
Dry, minimum quantity lubrication and cryogenic cooling were applied as cooling strategies of Inconel 718 and it was found that in the latter case, the surface is harder, but the affected layer is thinner than in the case of dry and MQL cooling.
This was confirmed also in [14], in which was found a reduction of the af-

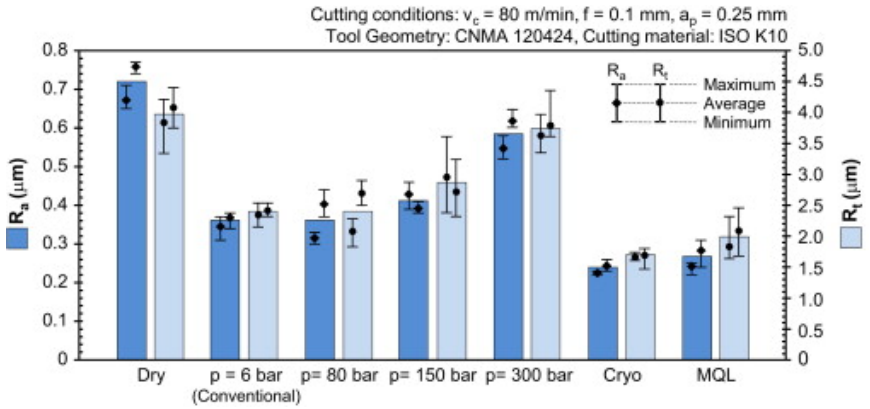

Figure 2.5: Surface roughness in machining of Ti-45Al-8Nb-0.2C-0.2B alloy, according to [14].

fected surface depth in γ-TiAl induced by cryogenic cooling.
Along with the benefits on grain refinement and hardness, cryogenic cooling is also expected to introduce compressive residual stresses on the surface and sub-surface layers.
It is known that residual stress is one of the most relevant parameters used for evaluating the quality of the machined surface, particularly when safety critical parts are machined, with the objective to reach the high reliability levels. Compressive residual stresses are usually aimed at the machined surface to increase the fatigue life.
In [15], the effect of cooling conditions, namely dry and cryogenic, on residual stresses induced on Inconel 718 was investigated both numerically and experimentally. It was assumed that the mechanical deformation and the elastic strain and stress are almost the same for dry and cryogenic machining. It was justified by the fact that the yeld stress of Inconel 718 is almost constant between the range of temperature typical of machining. A confirmation of that is given by the measurements of the cutting forces during the process which do not vary as a function of the cooling conditons adopted. Therefore, the residual stresses changes are attributable only to the thermal component. Cryogenic machining produces less tensile residual stresses on the surface and subsurface than those of the dry ones, because the temperature is approximately 100°C lower during cutting operations.
Results are confirmed in [16], in which residual stresses are measured after machining of a AZ31B magnesium alloy.
In [17], a comparative evaluation of surface integrity in dry, minimum quantity lubrication, and cryogenic turning of Inconel 718 was assessed. In case of cryogenic machining, the zone affected by residual stresses was increased up to 75% compared to the dry case. The higher values correspond to a thicker compressive zone beneath the machined surface and hence to a longer fatigue life of machined parts.

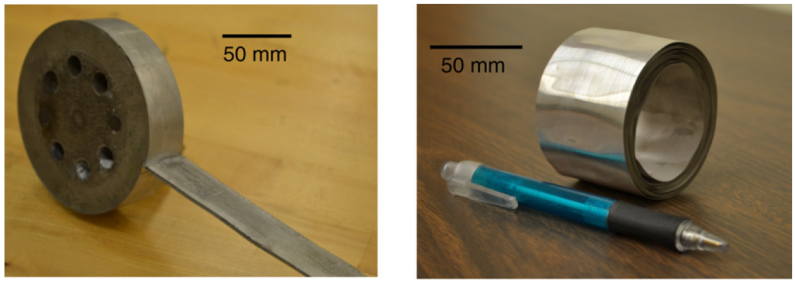

(a) *MgAZ31 sheet of large dimensions (2 mm thick * 25 mm) produced by LSEM, with one end of the sheet is still attached to the bulk workpiece.*

(b) *MgAZ31 sheet of large dimensions (0.18 mm thick * 50 mm) wide coiled strip generated by LSEM.*

Figure 2.6: Examples of sheets production by using LSEM, according to [21].

The effect of cryogenic machining on surface roughness is not uniquely defined.
An improvement in surface quality in terms of R_a is given by the adoption of cryogenic cooling in machining AISI 52100 steel ([11]). Fig. 2.5, reports the experimental evidences. An explanation of that can be attributed to the fact that the adoption of cryogenic cooling resulting in a stable cutting process, which reduced the flank wear decisively. Actually, the cutting force analysis showed a rapid increase in dry machining as a result of tool-wear [18]. In addition, to cryogenic machining is attributed a more efficient heat removal from the cutting tool insert, as well as reduction in thermal softening of the cutting tools [19].
In spite of these evidences, in [20], a surface roughness increase was found as a consequence of the machining and burnishing of pre-cryogenically cooled hardened AISI 5140 steel. It was presumably due to the effect of increased hardness and strengths of the frozen workpiece which have worsened the surface quality.

2.3 The impact of large strain extrusion machining on surface integrity

Large Strain Extrusion Machining (LSEM) is a deformation process which exploits the intense and localized deformation to create sheets directly form the bulk material (Fig. 2.6). Actually, the production of magnesium foils is the principal challenge for weight reduction in the discrete products manufacturing sector.
Although magnesium can be refined and cast and relatively inexpensively, creation of strip is challenge due to the poor formability of the hexagonal

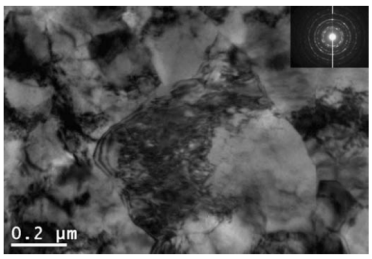

Figure 2.7: Copper surface showing nanoscale microstructure $\gamma \sim 8.0$ (-10° rake angle), according to [22].

closed-packed (hpc) structure. Therefore, a lot of studies deal with the effect of LSEM process parameters on the sheet' production.
Aniway, in this work LSEM was applied to evaluate its effect on surface integrity of the machined bar; unfortunately only few researchs aim to aimed to this goal.
By means of using LSEM, a bulk and particulate nanostructured materials can be achieved, thanks to the considerable deformation imposed on the surface of the bulk workpiece.
In [22], LSEM was applied to achieve a nano-scale grain size on copper workpiece. Fig. 2.7 shows a Trasmission Electron Microscopy (TEM) micrograph and selected-area diffraction (SAD) pattern (inset) representative of the fine-scale microstructure on the machined surface of copper (strain $\sim$8). The microstructure consists of nanoscale structures with an average size of 175 $\pm$ 30 nm. This was achieved by LSEM-ed a bulk material with an initial grain size of 35 $\pm$ 5 μm. From these basis, it can be concluded that LSEM is machining-based approach that can be used as a potential way to obtain a synergistic combination of graded microstructures and high mechanical properties on both chips and machined workpiece.
The effect of different process parameters, namely cutting speed and hydrostatic pressure, in LSEM of the AZ31B magnesium alloy was investigated in [21]. The suppression of the chip segmentation was achieved and sheets with an Ultra-Fine Grain (UFG) microstructure were obtained thanks to the careful choice of the investigated process parameters.
In [23] the feasibility of exploiting LSEM as a low-cost production technique for manufacturing magnesium sheets was investigated. Results showed that completely different chip microstructures, ranging from heavily cold-worked to fully recrystallized ones, could be achieved by controlling the adiabatic heating in the deformation zone. The corresponding grain size varied from UFG (100-500 nm) to conventional fine-grained (2-5 μm).
High Speed Extrusion Machining (HSEM) were applied in [24], with the aim of improving the AZ31B surface integrity. Experiments with different Constraint Extrusion Factor (CEF) were carried out, demonstrating that when the factor exceeded a certain value a lower roughness of the machined

surface could be achieved.

2.4 The impact of ultrasonic vibration turning on surface integrity

Ultrasonic Vibration Turning (UVT) is an innovative machining techniques in which a high frequency alternative motion is given to the cutting tool. It is applied to a wide variety of difficult-to-cut materials, such as superalloys, ceramics and glass, resulting effective in an ultraprecision turning of components of tight geometric tolerances. Moreover, the cutting tip oscillating motion lowers the cutting forces and increases the heat removal.
At the same time, UVT induces on the workpiece surface a distinctive structured texture that could improve mechanical, biological and optical properties.
However only few studies deals with the effect of UVT on the surface integrity.
The comparison between conventional turning (CT) and UVT and their effect on mechanical properties of a titanium alloy were invetigated in [25]. It was found that UVT does not alter mechanical properties compared to the unprocessed material; on the contrary CT leads to the formation of harder surfaces after machining operations. Thus was not expected since the strain hardening of UVT is higher compared to the one obtained with CT.
The same conclusions were achieved in [26], in which UVT is applied to an Inconel 718 alloy. Softer surfaces, with hardness values closer to the ones of the bulk material were obtained in the case of UVT. Simliarly, the layer affected by mechanical process is wider in the case of CT than that of UVT. This was attributed to the fact that UVT leads to a considerably reduction in the cutting forces.
The effect of process parameters when cutting Inconel 718 by applying both the UVT and CT was investigated in [27]. Figs. 2.8 a) and b) reveal that the surface finish with the UVC method is improved by approximately 75%-85% over the CT method. Therefore, a high-quality surface finish for tough cutting could be achieved thanks to the ultrasonic motion of the tool.
The tool-workpiece contact ratio is 100% in the CT method, therefore, the generation of thick, uneven and severe cracked chips, built-up edge, high-cutting force components, frictional heat, and high-cutting instability, deteriorated the machined surface and finally produced a rough and coarse surface.
On the contrary, during UVT a reduction of cutting forces, frictional forces and frictional heat, the production of comparatively sharper fine chips that have less influence on the machined surface due to the limited contact ratio between the tool and the workpiece are obtained.
Thus, the surface finish induced by UVT method is regular and smooth, and

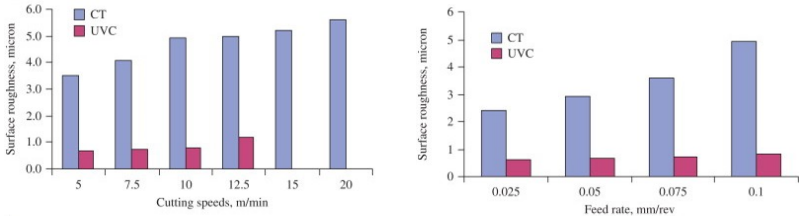

(a) *Average surface roughness values, Ra in both the cutting methods after 10 min of cutting against cutting speeds at a feed rate of 0.1 mm/rev.*

(b) *Average surface roughness values, Ra in both the cutting methods after 10 min of cutting against feed rates at a cutting speed of 10 m/min.*

Figure 2.8: The effect of process parameters and cutting technology on surface roughness, according to [27].

usually much better than that those obtained with the CT method.

2.5 The impact of ultrasonic vibration turning on functional performances

Ultrasonic vibration turning is used as a mean to modify functional performances of the machined materials, especially in terms of wettability and wear behaviour.
Elliptical vibration cutting (EVC) was used as a mean to realize two-level hierarchical micro-structures in [28], to modify the anisotropy of the water droplet.
Anisotropy refers to differences between angles measured in two different directions, namely parallel and perpendicular (Fig. 2.9). Controllable sinusoidal micro-textures with a wavelength one order of magnitude smaller than the widths of the first-order micro-channels were applied to the surface in order to modify the isotropy of the water droplet. In this way, super hydrophobic surfaces can be created.
Feed-direction ultrasonic vibration-assisted turning (FUVAT) was used to generate micro-textured surface on copper 1100 in [29]. Several parameters including amplitude, feed rate, and spindle speed and their effects on patterns and shapes of microstructures were investigated. It was found that, compared with the surface fabricated by the turning without ultrasonic vibration, the hydrophilicities of two textured surfaces are enhanced because of the water contact angles decreasing from 84.02° to 69.67° and 70.85°, respectively. The latter angles correspond to the surfaces FUVATed with different amplitudes, namely 5 μm and 10 μm respectively, while the other cutting parameters remained fixed.

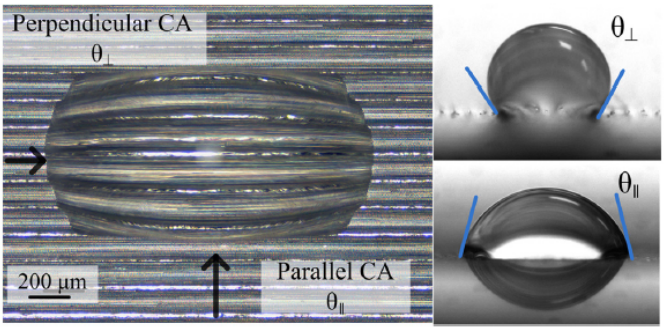

Figure 2.9: Anisotropic droplet and contact angle definition, according to [28].

Elliptical vibration texturing (EVT) technique has been applied to generate different microtextures on cylindrical aluminum surfaces for experimental studies on surface wettability control in [30]. Micro-dimples, microchannels, and grid patterns were generated by carefully choosing the processing parameters. It was shown that the dimple patterns overall increase hydrophobicity compared to the smooth pre-machined cylinder. Morevoer, between dimples texture, increasing the feed, leads to the a decrease in the area fraction of the solid-liquid contact, which, according to the Cassie-Baxter model, decreases the water droplet contact angle. In addition, it was demonstrated that the effect of DoC is more controversial, because above a certain level, dimples can overlap each others. When the DoC is smaller than the critical value, the surface topography is in the form of dimples. In this situation, the area fraction of the solid-liquid contact increases with the increase in the DoC, and so, the water droplet contact angle increases at the same time. When the DoC is larger than the critical value, micro-channels are beginning to form. With the increase in the DoC, both of the width and depth of the micro-channels increase.
As well as to modify wettability, UVT is gerally used also for improve wear performances.
In [31], the effect of three vibration modes, namley one-dimensional, two-dimensional, and three-dimensional (3D-VT), during ultrasonic turning on the tribological properties is examined. Compared with conventional face-turning surfaces, average friction coefficient of the surfaces face-turned by LVT, EVT, and 3D-VT processes, shows a maximum decrease of 13%, 18%, and 21% respectively. Moreover, compared with CT process, because of the unique features of UVAT process in creating micro-dimples, the contact between chrome-steel pin and the sample surface decreases; this in turn leads to further reduction in wear rate for the processes of LVT, EVT and 3D-VT respectively.
The friction behaviour of three different types of surfaces, namely ground, lapped and textured against a stainless steel ball were investigated in [32].

In the presence of surface texture, the coefficient of friction was reduced by 30% in some of the cases, attributed to the effective lubrication at the concentrated point contact in the presence of dimples.
On these basis, it can be concluded that UVT is a potential method to modify both wettability and wear behaviour of the workpiece.

2.6 Titanium alloys

The poor tribological properties of titanium alloys are still a limit for their widespread use in many industrial fields. The wear resistance of these materials can be improved by using surface treatments, which are able to increase the surface hardness of titanium alloy components decreasing the wear rate. A literature review on the different strategies applied to improve wear performance of titanium alloys will be presented in the following sections.

2.6.1 The impact of mechanical processing on wear resistance

Microstructure and mechanical properties

In [33], the dry sliding wear behavior of Ti6Al4V alloy sliding against itself at different sliding velocities and applied load was studied. The low wear resistance was attributed to the poor protection exerted by the surface oxide, since it is brittle and tended to be continuously fragmented [34].
A currently used approach for enhancing the tribological properties of titanium alloys for improved wear resistance is to perform surface modifications for increased hardness and, as a consequence, reduce the friction coefficient. Thermal oxidation is a popular process which substantially improves the wear resistance. This technique is based on the hardening of the surface oxide layer.
Wear tests carried out on both untreated and oxidised samples, in dry sliding conditions, show that the thermal oxidation substantially improves the wear resistance [35]. Actually, as a consequence of the oxidation (1173 K for 2 h at 10^5 Pa) and hardening of surfaces layers was produced.
The process of shot peening was employed in [36], to led an improvement in the wear resistance of titanium alloy Ti6Al4V due to improved mechanical properties. Unfurtunately, the process induced also a considerable increase in surface roughness.
PVD coating (TiN, TiC), ion implantation (N+), thermal treatments (nitriding, diffusion hardening) [37], or laser alloying with TiC [38] were succesfully apply to titanium in order to improve wear resistance. Unfortunately, these procedures affected only few microns under the surface, offering a limited protection from wear with long prospective.
Alternatively, techniques likes mechanical attrition treatment (SMAT) [39],

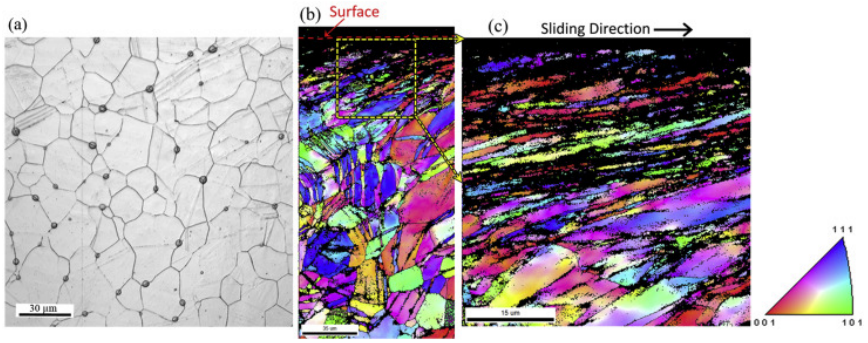

Figure 2.10: (a) Laser microscope image displaying initial microstructure of the untreated TNTZ alloy. Cross-sectional EBSD analysis of UNSM-treated TNTZ alloy specimen. (b) Inverse pole figure (IPF) map. (c) High magnification IPF map from the top area of (a). Data according to [43].

shot peening (SP) [40], ultrasonic shot peening (USP) [41], and laser shock peening (LSP) [42] basically reduce the size of material grains to the nanoscale that can be used to improve their wear resistance and performance.
Ultrasonic nanocrystal surface modification (UNSM) technology has been introduced as an efficient method for generating gradient nanostructures on metal surfaces by application of ultrasonic impact through a hard tip to induce high-strain-rate plastic deformation on the surface. The comparison between the initial microstructure and the one after the process is reported on Fig. 2.10. It can be seen that the ultrafine lamellar grains of the top surface were almost parallel to the treated surface and the presence of the mostly non-indexed dark region in the area close to the surface suggested the generation of nanostructures in this region. The experimental results showed that UNSM-treatment not only improves the wear resistance of TNTZ alloy, but also enhances its biocompatibility. In the case of wear resistance, UNSM-treated specimen showed 7 times higher wear resistance than the untreated specimen.
In conclusions, it can be said that the mechanical properties of the surface conditions in very severe way the wear performance of titanium alloys.

Surface roughness

The influence of surface roughness of commercial CoCrMo femoral heads on the wear rate of ultra High Weight Molecular PoliEthylene (UHMWPE) during in-vitro tests was studied in [44], where it was found that either the total roughness (Rt) or the skewness (Rsk) were better indicators of the polyethylene wear than the average surface roughness (Ra).
The influence of the manufacturing-conditioned roughness on the wear behaviour of knee prostheses using a wear simulator system was investigated in [45], but it was stated that the considered surface parameters did not

substantially influenced the implant in-vitro performances.
The influence of taper junction roughness on the wear rate basing the study on 50 retrieved Metal on Metal (MoM) bearings was evaluated in [46]: it was found that only few surface parameters, among which reduced peak height (Rpk) and skewness (Rsk), were significant in determining the amount of wear volume loss.
On the base of these studies, it can be concluded that a clear relationship between surface roughness parameters and the wear performance of titanium alloys is still not well understood.

2.7 Magnesium alloys

Biodegradable alloys usually refers to the alloys which, once placed in the human body, do not cause adverse pathophysiological and toxicological effects [47].
Among all the metallic materials, magnesium possesses one of the best biocompatibilities with human physiology and the best mechanical compatibility with human bone [48]. Actually, it has a density and an elastic modulus similar to the one of the fuman body, succesfully preventing the stress shielding phenomena due to the excessive stifness of the implant. Magnesium is also essential for the human metabolism, since it is a cofactor for many enzimes [49].
However, the unsatisfactury corrosion performances of magneium lead to the loosening of mechanical properties before the bone has the necessary time to heal.
A strategy to strenghten the corrosion behaviour is needed.
Alloying and coating are two major approaches widely studied [50].
However, alloying may introduce elements that lead to adverse biological reactions.
Stability of the coating is jeopardized by the stress applied to the implants during its in-vivo service life. In addition, coating tecniques are costly and time-consuming.
Mechanical processing of magnesium alloys provides an alternative approach to controlling the biodegradation rate through the modification of the surface integrity.
A literature review on how these surface integrity changes influence the corrosion resistance will be presented in the next section.

2.7.1 The impact of mechanical processing on corrosion resistance

Grain size

The grain size of magnesium alloy plays a key role into determining its corrosion resistance. Grain boundaries increase the rate of diffusion and the electron activity and reduce atom coordination. Reducing atom coordination results in a lower work function of the surface, which makes removal and adsorption of species more feasible and probably increases rate of the charge transfer.
Increased reactivity has also supported the notion that grain boundaries have adverse effect on corrosion resistance and function as initiation sites for corrosion.
However, magnesium can be a special case since its oxide layer is not stable in aqueous solutions owing to high geometrical mismatch between the oxide layer and substrate.
Additionally, the cubic magnesium oxide in aqueous solutions transforms to hexagonal magnesium hydroxide upon hydration, which has a volume approximately double of that of magnesium oxide. This process leads to disturbances in the film, causing compressive rupture which results in continual corrosion process.
A fine-grained microstructure most likely provides a mean for relieving this stress via high fraction of grain boundaries and reduces the degree of oxide cracking [51]. Hence, if the initial magnesium oxide layer formed on fine-grained surfaces provides better surface coverage and inhibits subsequent rupture of the exterior magnesium hydroxide layer, then slower corrosion rates in the case of fine-grained structures can be explained [51], [52].
Higher corrosion resistance observed from fine-grained Mg has been attributed to a better passive film as demonstrated by repassivation scratch experiments and decreased corrosion rates in NaCl electrolytes [53]. The notion of a more protective passive film is also supported by the observation of reduced cathodic kinetics in 0.1 M NaCl on grain-refined Mg.
A severe grain refinements is achieved in [54], by means of using burnishing with different cooling conditions, namely dry and cryogenic. The grain boundaries near the surface after cryogenic burnishing were not visible (Fig. 2.11b) while those after dry burnishing are still discernable (Fig. 2.11a). The reduction in grain size was approximately of 88% for dry case and further reduced in the case of cryogenic burnishing. Electrochemical tests of the burnished surfaces evidenced a reduction of the cathodic polarization current densities, but an increase in the anodic ones. In addition, both the Nyquist plots and hydrogen evolution tests confirm that burnishing surfaces have better corrosion behaviour to that of grounded alloys. This study reveal that grains size has an unquestioned role, since it burnished surfaces

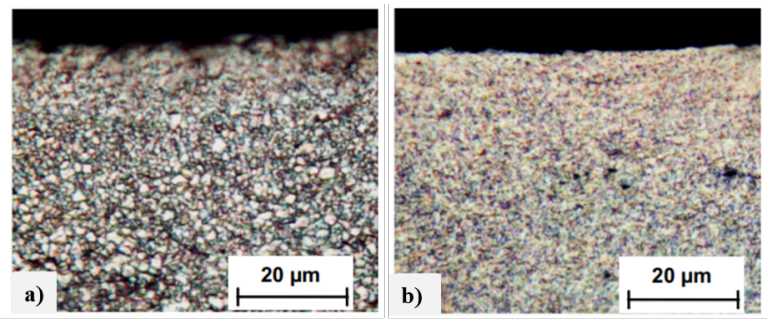

Figure 2.11: The effect of different cooling strategies on the microstructured of burnished AZ31 Mg alloys: a) dry, b) cryogenic, according to [54].

performed better than the grounded ones.
On the contrary, only a slightly differences were found between dry and cryogenic ones, although the latter was characterized by finer grain size. This suggests the presence of a threshold value, beyond which the corrosion resistance is affected no more by the grain size.
In [55], liquid nitrogen was sprayed onto the machined surface from the clearance side of the tool during orthogonal machining of AZ31B alloy. Different radius of the cutting tool were investigated, namley 30 μm and 70 μm. In the case of a radius of 30 μm, a featureless later is formed only with the application of the liquid nitrogen. A featureless layer, in which grain boundaries are not visible, is found in the case of the highest radius, regardless the cooling condition. It was shown that the extension of the featureless layer was directly proportional to the radius of the cutting tool. The formation of a ultra-fined grain structure was attributed to the dynamic recrystallization. Corrosion behaviour was measured by means of immersion tests in two different solution, namely 0.5% NaCl for 8 hours and simulated body fluid (SBF) for 10 days. Resutls show a directly relationship between the thickness of the featureless layer, which leads to a strengthen of the oxide film, and the corrosion performance for both the solutions studied.
The achievement of a 30 μm thick featureless layer after cryogenic machining was obtained also in [56], in which a ZK60 alloy was machined with a feed of 0.015 mm/rev and a cutting speed of 120 m/min.
In [57], Equal Channel Angular Process (ECAP) was applied to AZ31 magnesium alloys and then its performances in vivo was studied. Different passes was applied in order to achieve differents grain refinement grades. It was observed that ECAP induced severe grain refinement in AZ31 magnesium alloy. Actually, the grain size was refined from a starting value of 47 μm to 15 μm after four passes. It is worth to note that twins and deformation features appear after the second pass. Corrosion current density, Icorr, was reduced for the ECAPed samples compared with AZ31 sample in the as-delivered condition indicating improved corrosion behavior. However, the

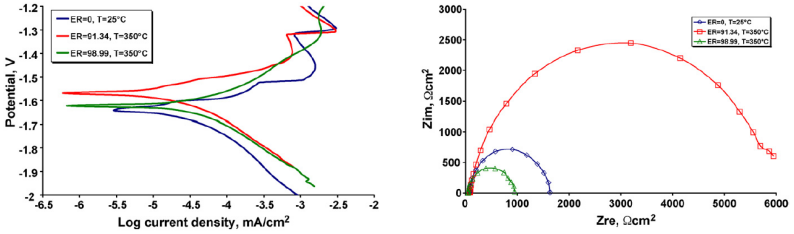

(a) *Potentiodynamic polarization curve of AZ31 Mg alloys in different extrusion ratios (ER).*

(b) *Nyquist plots comparing the corrosion behavior of AZ31 Mg alloys in different extrusion ratios.*

Figure 2.12: The effect of severe plastic deformed structure on the corrosion behaviour of AZ31 Mg alloy, according to [59].

Icorr was found to increase as the number of ECAP passes was increased, indicating a reduction in corrosion resistance. This means that, even if they the latter samples are characterized by finer grains, they have worse corrosion performances. This was attributed to the large amount of crystal defects like stacking faults and dislocations, that are preferentially sites of corrosion initiation [58]. In [59], the corrosion behavior of the as-received, conventional extruded, and ECAE-ed samples was studied by potentiodynamic polarization. Test results indicated that the corrosion rate of the as-received is lower than the alloy after plastic deformation. The corrosion resistance after conventional extrusion was higher than after the ECAE process. It was said that the corrosion results were influenced by two factors: grain size and extrusion ratio which, in turn, refers to the density of dislocations. After the conventional extrusion the grain size decreases. Small grain size creates more grain boundaries that act as a corrosion barrier. After the ECAE process the grain size was similar to the grain size after conventional extrusion, but the density of dislocations, that are responsible of faster anodic dissolution, was increased (see Fig. 2.12).

Residual stresses

The underlying stresses and strains induced by processing may impart cracks or defects in the material and diminish any positive effect from increasing grain boundary densities. Residual stress will alter the free energy state of the material, which, in turn, can change the work function of the material surface.
According to [54], the residual stress state induced by the cryogenic burnishing process it was identified as the responsible of the anodic corrosion current density increase.

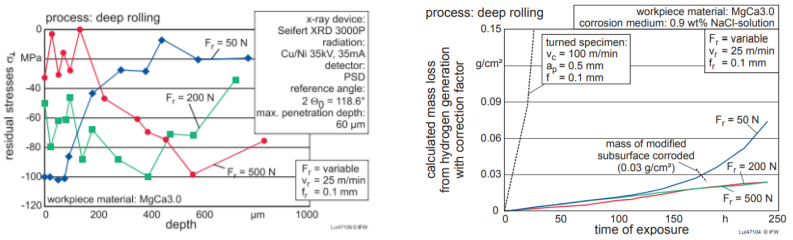

(a) *Residual stress depth profile of deep rolled samples.* **(b)** *Corrosion progression of deep rolled samples.*

Figure 2.13: Effects of deep rolling parameters on residual stress and corrosion performances according to [60].

Different residual stress states were generated in the subsurface by a turning and deep rolling process to reduced the corrosion rate of MgCa alloys [60]. Only in the latter case, parameters-dependent state of compression was found. Mass loss experiments evidenced that the corrosion rates of the turned workpieces were approximately a hundred times higher than the corrosion rates of the deep rolled surfaces, confirming that compressive residual stresses are beneficial for corrosion resistance improvement (Fig. 2.13).
In [61], it was shown that the corrosion rate of a peened surface is drastically reduced by at least 100-fold and depended heavily on the laser power and peening overlap compared to unpeened surface.
In conclusion, it is generally aknowledge that compressive residual stresses are beneficial toward corrosion resistance.

Surface texture

It was consistently confirmed that the rolled surface with (0001) plane has better corrosion resistance with a slightly thinner, but more compact, film than those in $(10\bar{1}0)$ and $(11\bar{2}0)$ planes in spite of having the similar grain size [62].
A closely packed plane has a higher binding energy due to a higher atomic coordination, which lowers the surface energy.
In addition, the electrochemical dissolution rates of basal and prismatic planes calculated can be calculated with the following Eq. 2.1:

$$I = nFk * exp(\frac{Q + anFE}{RT}) \tag{2.1}$$

where n is the number of electrons involved in the electrochemical reaction; k is a reaction constant; a is a transit coefficient; F, R, T and E are Faraday constant, gas constant, absolute temperature and the electrode potential, respectively.
Q is the activation energy for a metallic ion to escape from the metal lat-

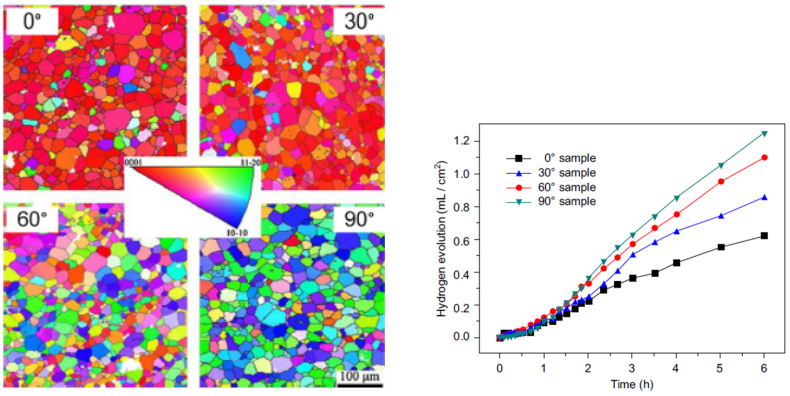

(a) *Inverse pole figure maps of 0°, 30°, 60°, and 90° samples.*

(b) *Hydrogen evolution rates of the AZ31 Mg samples immersed in 3.5 wt% NaCl.*

Figure 2.14: The effect of surface texture on corrosion resistance, according to [62].

tice and dissolve in the electrolyte solution, which is higher for the densely packed surfaces than those in the loosely packed ones.
The closely packed (0001) surface showed a more positive open circuit potential (OCP) value than that of less densely packed $(10\bar{1}0)$ and $(11\bar{2}0)$ ones. Different obtained OCPs imply the formation of microgalvanic cells between grains with different orientations [63] [64].
The surface energy has indirect, hence less significant, influence on the activation energy of hydrogen reaction than that for metal dissolution. Therefore, the difference between planes is less at the cathodic current density than at the anodic one [64].
In [54], different burnishing condition were applied to manufacture AZ31B. The heights of the basal plane (0002) increased after the process, regardless the cooling condition adopted. It was shown that, corrosion initiates preferably far from the machined surface in which, although of finer grains, the presence of basal plane diasppear.
In [63], the electrochemical activities of different surfaces after rolling was studied. The rolling surface of AZ31 mainly consisting of closely packed crystallographic plane (0001) has lower surface energy and thus its anodic dissolution and cathodic hydrogen evolution are more difficult than a cross-section surface on which most grains are $(10\bar{1}0)$ and $(11\bar{2}0)$ orientated. As a result, the rolling surface is more corrosion resistant than a cross-section surface in 5 wt.% NaCl solution. The effect of surface texture on hydrogen evolution rates is reported on Figs. 2.14a) and b).

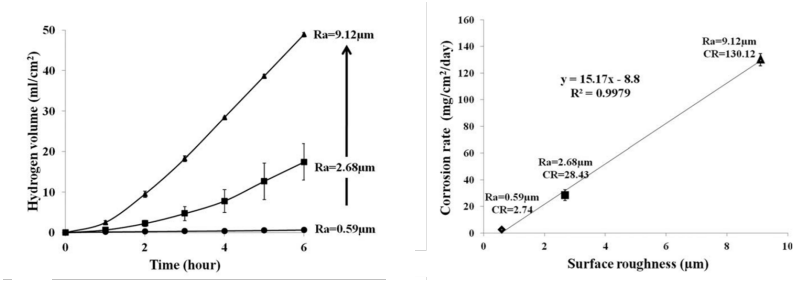

(a) *Hydrogen evolution for samples with different surface roughness degree.*

(b) *Corrosion rate as a function of time for samples with different surface roughness degree.*

Figure 2.15: Effect of surface roughness on corrosion behaviour, according to [66].

Surface roughness

The relationship between surface roughness and degradation behavior in magnesium (Mg) biomaterials is still a controversial issue.
In [65], different surface roughness values were obtained by grinded/polished with different degree on a sand-cast AZ91 magnesium alloy. The corrosion behaviour of the alloy was then studied using different electrochemical techniques, namely potentiodynamic polarisation and electrochemical impedance spectroscopy (EIS). The corrosion potential (Ecorr) of the alloy shifted towards the noble direction as the surface roughness decreased. Notably, the corrosion current (Icorr) decreased as the surface roughness decreased. Interestingly, as the surface roughness decreased the alloy revealed a passive-like behaviour before a sharp break-down: the alloy with the lowest surface roughness showed a passive-potential region of about 79 mV, whereas the highest surface roughness alloy showed no evidence of passive region.
The same conclusions were achieved in [66], in which a direct proportionality between the hydrogen evolution and surface roughness values were found as reported on Fig. 3.7a). A linear correlation (R^2=0.9979) was found between surface roughness and mass loss (see Fig. 3.7b).
However, it is worth to note that availiable studies on the effect of surface roughess on corrosion performances involved completely different surface roughness levels, which do not reflect the situation that is obtained by changing machining parameters during turning process.

Chapter 3

Introduction to materials under investigation

In this Chapter an overview on the biomaterials under investigation is provided. General information about the main concern related to their in vivo functional perfomances are given. The different real case studies which will be investigated in this research study are presented, with a particular reference to the concerns related to their in vivo functional perfomances. According to the general structure of this thesis, first data on titanium are presented followed by the ones pertainent to magnesium alloys.

3.1 Titanium alloys

Titanium alloys are nowadays the most attractive metal alloys for biomedical applications thanks to their chemical (i.e.corrosion resistance, biocompatibility) and mechanical properties (i.e.stiffness, density).
However, they usually present a low wear resistance to the combined action of body fluids and micromotions, which usually accelerates the release of metal debris and reduces the implants lifetime due to adverse tissue reactions. Therefore, wear behaviour represents the functional property which has been optimized in the case of titanium alloys.
In the biomedical field, the application of wear can be studied under two major areas, namely, orthopedic surgery science and dentistry.
A brief introduction of the case study evaluated is given below.

3.1.1 Orthopedic

Titanium based implants are widely used in the orthopedic science, especially hip and knee joints replacements.
However, since only the hip joint was used as a reference case-study in this thesis, a brief description of it was given in the following sections.

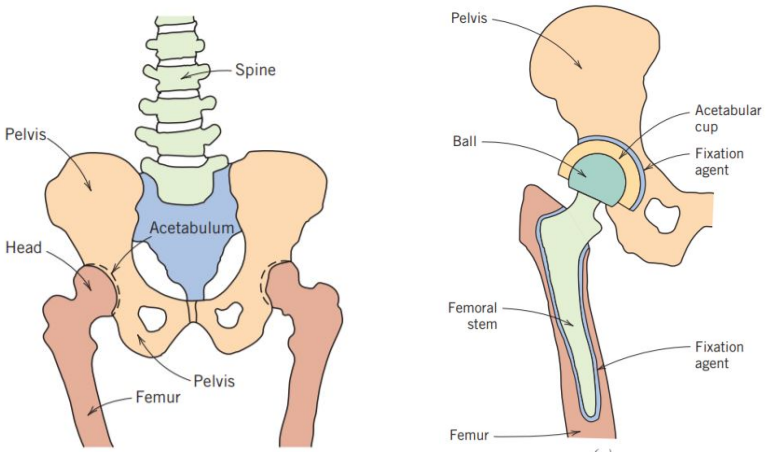

(a) *Schematic diagram of human hip joints and adjacent skeletal components.*

(b) *Schematic diagram of an artificial total hip replacement.*

Figure 3.1: Schematic diagram of an artificial total hip replacement, according to [68].

Anatomy of the hip joint

The joint is an important component of the skeletal system.
It is located at bone junctions, where loads may be transmitted from bone to bone by muscular action; this is normally accompanied by some relative motion of the component bones.
The human hip joint (Fig. 7.2a) occurs at the junction between the pelvis and the upper leg (thigh) bone, or femur. A relatively large range of rotary motion is permitted at the hip by a ball-and-socket type of joint; the top of the femur terminates in a ball-shaped head that fits into a cuplike cavity (the acetabulum) within the pelvis.
A total hip replacement is basically composed by: (1) the femoral stem, (2) the ball that attaches to this stem, (3) the acetabular cup that is affixed to the pelvis, and (4) a fixation agent that secures the stem into the femur and the cup to the pelvis (Fig. 7.2b).
To date, there are several hip joint configurations, with the Metal-on-Polyethylene (MoP) the most commonly used. MoP consists in a metal head linked to the femur with a taper or a stem; the metal head articulates with a polyethylene liner (usually UHMWPE), fixed in an acetabular component that is anchored in the pelvis.
However, aseptic loosening continues to be the main limiting factor in the longevity of MoP Total Hip Arthroplasty (THA), being associated with the substantial release of polyethylene wear particles [67]. To face this problem, alternative bearings MoM prosthesis, became a popular choice, especially for younger patients. MoM pair refers to the metal head coupled directly

with a metallic acetabular cup part. Besides reduction in wear, another advantages lye in the improving range of movement and a lower dislocation rate; however problems related to the generated wear debris's size began to rise.
MoM bearings generate approximately $6.7 * 10^{12}$-$2.5 * 10^{14}$ nano-scale particles per year. This is 13 500-times the number of ultra-high molecular weight polyethylene particles produced from a typical MoP bearing.The smaller MoM particles result in lower volumetric wear than MoP hips but wider particle dissemination, beyond the peri-prosthetic tissues [69]. The number of failures, coupled with growing concerns about the possible genotoxic effects of long-term exposure to metal wear debris, has led to the growth of caution when considering the use of MoM bearings [70].

3.1.2 Failures of arthroplasty

Approximately around the 10% of the implanted devices will fail and will require a second surgery, called revision, to remove the old one and restore with new components.
The revision operation is a difficult procedure which requires a long scheduling prior to surgery. The 90% of the implants will satisfy all the requirements and will be able to work fine to 10 or even 20 years in a human body. In fact, this kind of implants are mostly designated to elder persons which have a low level of activity and consequently tends to load less the joints. But, considering that more and more young patients get subjected to this surgery and old people live longer, a raising number of patients will live longer than their prosthesis.
Beside this, the new biomaterials employed reach a better fixation with the bone tissues and the wear rate is modest.
There are several reasons for an implant failure, but the most widespread are the following: 1) loosening, 2) infection, 3) luxation and 4) patient's related factors.
The aseptic loosening is one of the most frequent cause of joint implants failure. It refers to the loosen of the implant, due to the fact that the body destroys the links between implant and bones in its trying to digest the wear debris. The latter are the results of a friction phenomena between rubbing surfaces, and they are collected nearby the articulation. Since the implants became loosen, the patient feel pain or instability. Also, during this process, the body digest also part of the bone (phenomenon known as lisi) [71]. This can weaken or even fracture the bone and compromise the success of a revision operation.
Infection refers to the reaction of the body to the extraneous implants which leads to the growing and multiplication of bacteria. As a consequence, an altered blood flux will sourround the prosthesis [72]. In these cases, the pain and the swelling will often make necessary a revision of the implant. Also,

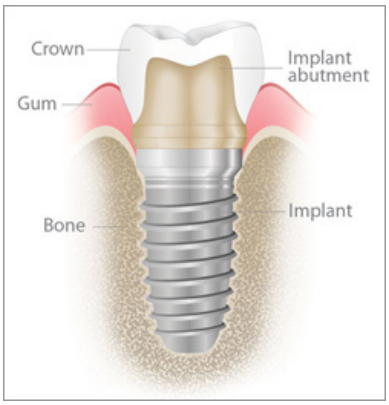

Figure 3.2: Schematic representation of a dental implant-supported prosthesis, according to [76].

if the infection is not nursed it can weaken the patient even to the point of risking its life. The risk of getting an infection due to these kind of surgery is around 0.5%.
The luxation is an unexpected migration of the prosthesis from its natural position. It is a typical problem for the hip implants, which affects one patient on 50. Some of these patients incurred in more luxation and therefore require a further surgery revision. The luxation can be consequence of the loosening, of the inadequate moving tissues, of a conflict scarring, of bad positioning of the prosthetic elements, of neurological problems (as Parkinson), or of nonconforming movements.
The younger and more active patients have a higher probability to be subjected to a revision surgery.
The obese patients have a higher incidence of wear and loosening of the implant.
The patients which have their primary operation due to the Rheumatoid Arthritis and the patients with vascular necrosis are more frequently subjected to loosening or luxation. All these conditions could lead to the revision surgery.

3.1.3 Dentistry

Nowadays, oral implants are not only used to replace missing teeth, but also to rebuild the craniofacial skeleton or to provide anchorage during orthodontic treatments [73].
It is currently estimated that over 2 million dental implants are placed annually [74]. Moreover, this number is expected to boost in the near future, not only due to an increasingly aged population, but also because implant therapies have become highly successful, with implant survival rates above 89% after 10 15 years [75]. Besides, unlike implants employed in other

areas of medicine, dental implants have two roles to fulfill, aesthetic and functional.
Endosseous implants are the most frequently used type of dental implants, these days.
Fig. 3.2 shows a schematic representation of an implant-supported prosthesis, consisting in an artificial tooth root (implant fixture) directly anchored into the maxillary bone to hold a replacement tooth crown. The abutment is a little cap that is screwed into the implant fixture and used to support the crown, connecting both structures.
However, these types of implants are subjected to cyclic micro-movements at the contact surfaces of the components, especially at the level of the implant abutment connection. Micro-movements are mainly caused by the transmitted loads during mastication, being the orientation of these stresses of high importance. Axial loads propagate the stress through the dental implant system to the bone tissue, while oblique loads can originate overload on implant structural materials and bone tissue, promoting failures by fatigue-wear of the implant-based system [77].
Moreover, microorganisms can colonize micro-gaps, and this fact could have relevance both on the magnitude of the micro-movements and on the long-term health of the peri-implant tissues.
Different types of metallic and ceramic structural materials can be used in dental implants and prostheses. Metals are highly used in dentistry due to their high strength, durability and resistance to fracture. On the other hand, they are more chemically susceptible to environmental attack, besides their poor aesthetics. For instances, commercially pure titanium is frequently used to fabricate dental implant fixtures while the abutment can be produced from several metallic alloys such as titanium-based alloys, chromium-cobalt molybdenum, gold and silver-palladium alloys; or from ceramic materials such as zirconia and alumina.

3.1.4 Failures of dental implants

Although success rates are high, dental implants still fail and must be replaced. The collapse of a dental implants is usually related to biomechanical or biological factors.
Biomechanical probems are due to the mico-movements which take place in correspondence of the implant system. In fact, an adequate fit between a crown-abutment or abutment-implant joint results in a more uniform adaptation and distribution of mastication forces. A poor fit of these parts can result in increase of relative displacement between the structural parts under mastication of occlusal forces, leading to tribological damage.
Concerning biological-originated failures, the main mechanisms leading to the collapse of the implant are related with microbial infection (peri-implantitis), low osseointegration kinetics, bone resorption, formation of fibrous tissues,

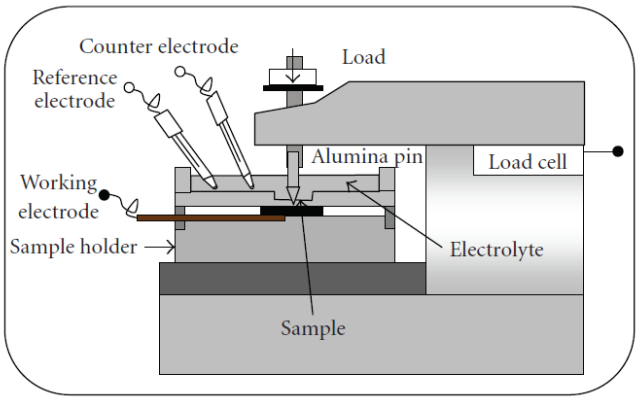

Figure 3.3: Example of modified tribocorrosion experimental setup with a reciprocating sliding tester, according to [84].

or the effect of wear debris and/or corrosion products/ions released due to the low amplitude sliding (micro-movements) between the implant root and the surrounding tissues [78] [79]. Among all, biological-originated failures involving microbial colonization are considered the most common. Usually, these microorganisms form complex structures, named biofilms [76], where they are embedded in an intricate extracellular matrix.

3.1.5 Chemical environment

The oral cavity chemical environment is extremely complex and harsh, contributing for the degradation of implants [80].
Saliva is the main fluid present in the oral cavity and plays a crucial role on the initial breakdown of food and on the lubrication of oral tissues, facilitating the manipulation of food and the swallowing process [81]. The viscous characteristics of saliva, provided by glycoproteins, can protect dental surfaces against wear. In fact, mucin, a protein from saliva, is known to have the ability to coat many surfaces of the human body, including teeth, respiratory and gastrointestinal tract, and reproductive organs [82].

3.1.6 Tribocorrosion tests

Tribocorrosion phenomena deals with synergistic effects of corrosion and wear that take place at the same time [83]. Electrochemical tests coupled to tribological tests are the currently useful method to assess tribocorrosion. A schematic illustration of a tribocorrosion set up is shown in Fig. 3.3. As seen, a potentiostat is assembled to a tribometer, in which a three-electrode electrochemical cell is placed, allowing both tribological and electrochemical parameters to be measured synchronously [85]. Different electrochemical techniques are being used to investigate the biotribocorrosion of materials,

but open circuit potential monitoring and potentiostatic control during sliding are the most common techniques used in tribocorrosion research.
OCP measurements consist in monitoring the electrochemical potential difference between the sample under investigation (working electrode) and a reference electrode, both immersed in the solution being tested. The electrochemical potential is a measure of the tendency to corrosion. However, in a sliding contact, it represents the galvanic coupling between the unworn area (which has a passive film, in the case of most biomaterials) and the worn region, where the bare metal might be exposed to the solution, due to the destruction of the passive film during sliding. This behavior is illustrated in Fig. 3.4a), where an abrupt decrease of the electrochemical potential (E) towards more active values is observed at the onset of the sliding test, indicating the destruction of the passive film. As observed in the figure, some fluctuation of electrochemical potential occurs during sliding, essentially due to depassivation/repassivation phenomena (destruction followed by regrowth of the passive film) occurring at the surface of the material which is being scratched. In the case illustrated in Fig. 3.4a), at the end of sliding, when the mechanical action stops, total repassivation of the material is observed, as the electrochemical potential recovers to values similar to those observed before sliding. However, OCP measurements cannot predict at what rate electrochemical reactions occur.
In potentiostatic tribocorrosion tests, an electrochemical potential is imposed to the sample under study during sliding while the corrosion current is measured. The applied potential can be either in the anodic or the cathodic domain of the electrochemical system under study, depending on the targets of the investigation. For instances, cathodic potentials are usually applied when the aim is to understand the behavior of the material in the absence of corrosion reactions on the material surface (for example to obtain data allowing the quantification of synergistic effects).
Anodic potentials can be applied for conditioning the properties of the passive film and control repassivation kinetics during sliding. The measurement of the corrosion current as a function of the sliding time allows the evaluation of the electrochemical kinetics of the tribocorrosion system. Again, the corrosion current measured by this technique corresponds to the sum of the current produced by all anodic and cathodic processes occurring in the entire surface exposed to the solution. However, in the case of passive materials, the local destruction of the passive film due to sliding makes the worn region as the major supplier of anodic currents, corresponding to dissolution. In fact, as shown in Fig. 3.4b), at the beginning of the sliding the corrosion current increases as a result of the local destruction of the passive film at the wear track. Oscillations in the corrosion current during sliding result from the depassivation/repassivation phenomena occurring at the wear track, as referred above. As soon as the sliding action finishes, the corrosion current decreases to values similar to those recorded before sliding, due to the rapid

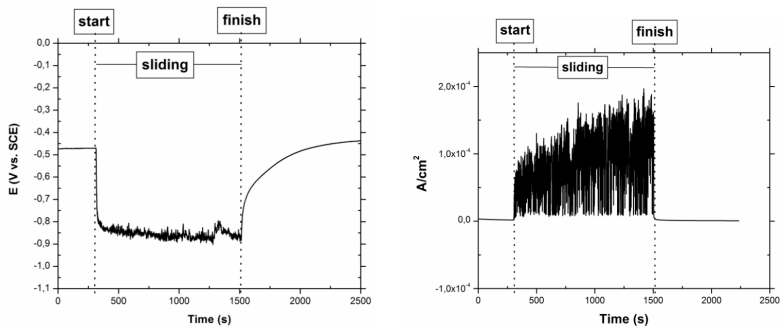

(a) *OCP monitoring during a reciprocating sliding test.*

(b) *Evolution of the corrosion current during a reciprocating sliding test.*

Figure 3.4: Examples of tribocorrosion measurements, according to [86].

repassivation imposed by the applied anodic potential.

3.2 Magnesium alloys

Biodegradable metals (BM) are emerging as an alternative for biomedical implants, since they expected to corrode gradually in vivo, with an appropriate host response elicited by released corrosion products, then dissolve completely upon fulfilling the mission to assist with tissue healing with no implant residues. BM is general terms which includes both metallic and polymeric materials.
With reference to the latter, in recent years, researchers and clinicians have highly exploited the variety of compositions, properties and form in which polymers are available to best match the specifications of the materials desired biomedical function [87]. However they tend to be too flexible and too weak for the load-bearing applications required in orthopaedic surgery. Moreover, they may also absorb liquids and swell, leach undesirable products such as monomers, fillers and antioxidants, and, furthermore, the sterilization process may affect their properties [88].
Thus, to overcome this drawback of polymeric materials, researchers and clinicians attention is attracted by metallic biodegradable materials.
Several of them have been studied but most of the scientific efforts focus on magnesium and its alloys due to the fact that, among all metallic engineering materials, Mg possesses one of the best bio-compatibilities with human physiology and the best mechanical compatibility with human bone. Indeed, its low density and elastic modulus best mimic the properties of natural bones. Moreover, Mg is the fourth most abundant element in the human body (it is recommended that an adult receive 240-420 mg daily) and it is needed for the human metabolism and biological mechanisms, since Mg

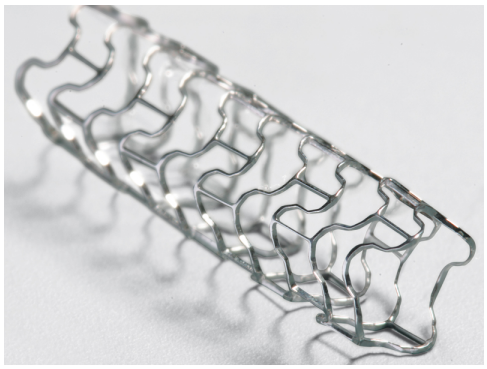

Figure 3.5: Bioadsorbable magnesium stent, according to Biotronik.

is a cofactor for many enzymes [89]. Finally, Mg^{++} ions, resulting from the degradation process (see section 3.2.4), are reported to aid the healing and growth of tissue and any excess of these ions is harmlessly excreted with urine [90].
Despite these advantageous properties of bioactive Mg and its alloys, some disadvantages limits their applicability as temporary implantable devices.
The major drawback is their high corrosion rate in the physiological environment that may lead to a loss of their mechanical integrity before the tissues have sufficient time to heal. Moreover, hydrogen as a corrosion product, and the generation of hydrogen pockets can influence the healing process or, if the pockets are large, they may cause death of patients through blocking of the blood stream [91].
Finally, the simultaneous action of the corrosive human-body fluid and the mechanical loading can cause the further complication of sudden fracture of implants due to corrosion-assisted cracking, such as stress corrosion cracking (SCC) and corrosion fatigue (CF).
To date, in the biomedical field magnesium is used mainly for two types of application, namely as cardiovascular stents and as orthopaedic and implant devices. A brief description of each one is given in Sections 3.2.1 and 3.2.2.

3.2.1 Cardiovascular implants

In general, a stent is an artificial tubular device that is surgically inserted into a natural passage in the body to counteract or prevent it from clogging. The most common type is the cardiovascular or, alternatively, coronary stent. Such medical device essentially consists of a thin-walled mesh tube with typical overall dimensions being 3 mm in diameter and 20 mm in length. Wall thickness and strut size can be as low as 50-150 μm. An image of a commercially availiable stent is reported on Fig. 3.5.
The current generation of stents are made of stainless steel, Nitinol or similar non-degradable metallic materials.

Table 3.1: Desirable requirements of a biomedical stent device, according to [90].

Aspect	Description
Absorption	Scaffolding integrity 36 months Full dissolution within 12 years
Biocompatibility	Non-toxic, no inflammatory tissue response No harmful release of particles
Mechanical properties	Tensile yield stress TYS >200 MPa Ultimate tensile strength UTS >300 MPa Tensile elongation >1518% Elastic recoil <4% (in conjunction with stent design)

Table 3.2: Basic design properties of various implant materials in comparison to natural bone, according to [90].

Material	Density (kg/m_3)	Elastic modulus (GPA)	Compressive yield stress (MPa)
Natural bone	1800-2100	3-20	130-180
Magnesium alloys	1740-2000	41-45	65-100
Titanium alloys	4400-4500	110-117	758-1117
Cobalt-chrome alloys	8300-9200	230	450-1000

A stent is implanted by shrinking it onto a balloon catheter and subsequently expanding it upon proper positioning in the artery. Thus, the stent material must comply with such mechanical requirements as strength and ductility in addition to biological demands, as is indicated in Table 3.1. Further, there are supplementary requirements that are not listed but nevertheless relevant, such as manufacturability, geometrical accuracy and fatigue resistance. Apart from that, stent design (that is, the actual mesh pattern) is an important aspect associated with these requirements; for instance, in relation to the plastic strains during shrinking and expanding and in relation to elastic spring-back, the so-called recoil, upon placement.
On these basis magnesium is an optimal candidate for the manufacture of biodegradable stent; as a matter of fact, the development of magnesium cardio-vascular stents is currently being undertaken with initial successes reported in [92].

3.2.2 Orthopaedic and other implants

The early efforts to introduce magnesium-based materials for implants were directed towards orthopaedic and, in particular, towards traumatological applications such as fixation plates, pegs and screws to secure bone fractures. An example of commercially availiable compression screw is reported on Fig. 3.6.

Figure 3.6: Herbert type magnesium compression screw, according to [93].

Table 3.3: Candidates for magnesium-based or magnesium-containing hard-tissue implants.

Joints	Knee implants, hip implants, shoulder implants, ankle implants, elbow implants, bone grafts
Spine	Internal spinal fixation devices, fusion cages, bone allografts, disc replacements, spacers
Dental/oral	Alveolar bone grafts
Other	Fixtures (plates, screws, pins, staples), tamponades, craniomaxillofacial patches, gauzes, sutures and suture anchors

Table 3.2 compares some relevant properties of natural bone with those of magnesium alloys, some conventional metallic implant materials. From this it appears that, among these materials, magnesium does most closely resemble the natural tissue that is to be temporarily supported and hence has the best structural biocompatibility. A specific role for the modulus of elasticity of the implant material is that a mismatch with the host material is known to introduce a so-called stress-shielding effect, being a common cause of loosening of permanent implants as the natural tissue retracts in a situation where it is under-loaded.
Further, in vivo animal trials have led to the notion that magnesium degradation enhances osteoblastic activity that promotes bone growth and thus healing, based on the observation of high mineral apposition rates and increased bone mass around magnesium-alloy bone implants as compared to a degradable polymer reference [94].
Magnesium thus appears to be an obvious candidate for such hard-tissue applications. Table 3.3 lists suitable applications for orthopaedic and related implants.

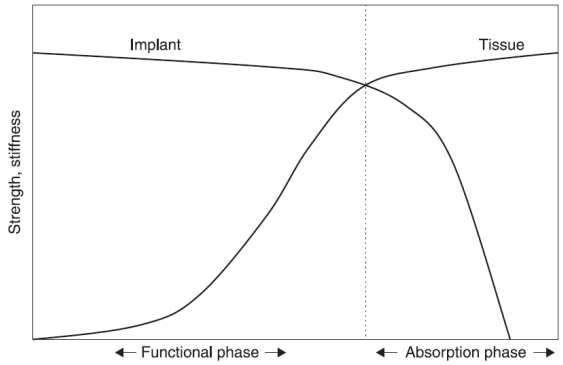

Figure 3.7: Schematic of the targeted mechanical behaviour of degradable implants (linear scales). According to [95].

3.2.3 Functionality of magnesium implants

As mentioned in the Section 3.2, the essential qualities of a degradable implant are that it maintains its integrity in the body for a certain time in order to fulfil its supporting function, after which it gradually dissolves, without leaving harmful residues behind.
Fig. 3.7 presents the generally desirable mechanical behaviour of a degradable implant in conjunction with that of the healing tissue, regardless the type of implant under consideration.
During its functional phase, the implant has to maintain mechanical integrity until the supported tissue has gained sufficient strength to support the natural loads. After this period, the implant has become redundant and mechanical integrity is of no further concern, so that strength may be lost during the absorption phase until the remaining implant structure collapses and in time disappears. While the desired duration of this process does highly depend on the particular circumstances, typical times for healing would be between a few months and a year.
With the previous in mind, it is clear that the degradation behaviour should be controlled, which effectively poses the biggest challenge for magnesium implant development.

3.2.4 Degradation mechanism

The following section deals with understaing the basic fundamental of corrosion of magnesium alloys.
Magnesium dissolution in aqueous environments generally proceeds by an electrochemical reaction with water to produce magnesium hydroxide and hydrogen gas, so that magnesium corrosion is relatively insensitive to the oxygen concentration.
The corrosion attack in aqueous environments often involves micro-galvanic

coupling between cathodic and anodic areas.
The overall corrosion reaction is:

$$\mathrm{Mg} + 2\,\mathrm{H_2O} \rightarrow \mathrm{Mg(OH)_2} + \mathrm{H_2} \tag{3.1}$$

This overall reaction may be expressed as the sum of the following partial reactions:

$$Mg \rightarrow \mathrm{Mg^{2+}} + 2\,\mathrm{e^-}(\text{anodic reaction}) \tag{3.2}$$

$$2\,\mathrm{H_2O} + 2\,\mathrm{e^-} \rightarrow \mathrm{H_2} + 2\,\mathrm{OH^-}(\text{cathodic reaction}) \tag{3.3}$$

$$\mathrm{Mg^{2+}} + 2\,\mathrm{OH^-} \rightarrow \mathrm{Mg(OH)_2}(\text{product formation}) \tag{3.4}$$

The anodic reaction (3.2) probably involves intermediate steps which may produce the monovalent magnesium ion $\mathrm{Mg^+}$ that has a short lifetime.
The poor corrosion resistance of Mg and its alloys can be mainly attributed to two key factors. These include: (i) the highly electronegative potential of Mg which allows corrosion to proceed even in the absence of oxygen, whereby the cathodic water reduction reaction predominates at such negative potentials and (ii) the poorly protective properties of any surface film formed upon Mg. This implies that any oxide or hydroxide layer that forms upon Mg is soluble in most aqueous environments or in the presence of humidity. Furthermore, Mg surface layers incompletely cover the underlying Mg metal surface and are highly defective [96].

3.2.5 Methods of analysis for Mg corrosion research

In this section, the main methods to investigate corrosion resistance of magnesium alloys are presented, subdividing them into electrochemical and non-electrochemical techniques.

Electrochemical tecniques

Among the electrochemical techniques, Potentiodynamic polarization (PDP) and Electrochemical Impedance Spectroscopy (EIS) are the commonly used.

Potentiodynamic polarization PDP employs a potentiostat, reference electrode, and counter electrode to scan the potential of an electrode over a fixed interval at a fixed rate. The PDP measurements also allow for the determination of the instantaneous Icorr at Ecorr. Assuming activation controlled kinetics of both the anodic and cathodic half reactions, Tafel extrapolation from potentials far enough from the Ecorr should intersect at (Icorr, Ecorr). Alternatively a computer can fit an idealized form of the curve to the experimental data to extract these values and the Tafel slopes [97].

Electrochemical impedance spectroscopy The EIS method consists of measuring the response of an electrode to a small amplitude sinusoidal potential perturbation at different frequencies. The fitting of the results to an equivalent circuit provides another means is used to determine R_p as well as information about the capacitive and inductive responses of the interface [98].

Non electro-chemical tecniques

Among the non electrochemical techniques, weight loss, hydrogen collection and pH measurements are the commonly used.

Weight loss The most common method for the study of metal corrosion is the weight loss method.
In weight loss testing, the specimen mass and specimen geometry is measured before and after exposure to a corrosive environment for a period of time.
The exposure conditions include immersion in an aggressive solution like the ones found into the human body. Prior to measuring the specimen mass after exposure, it is necessary to clean the sample to remove the corrosion products from the surface. This is a critical step as it can lead to inaccuracies including overestimation or underestimation of the corrosion rate as a consequence of an insufficient or excessive cleaning after immersion, respectively. In the case of Mg, it is recommended to use a dilute chromic acid solution that may contain silver and barium nitrate [97].
Weight loss measurements are limited by the resolution of the gravimetric device. For this reason, an accurate microbalance and multiple replicates to provide confidence in weight results result are required.
Even though weight loss measurements are simple and well established, they only provide an average corrosion rate over the exposure period and this rate will often change with time. Nonetheless, weight loss tests can also provide an exposed surface from which assessment of corrosion morphology can be ascertained.

Hydrogen collection Different experimental approaches have been used to perform hydrogen collection measurements. The volumetric method is extremely simple and widely used. The corroding sample is covered with a funnel inserted into an inverted burette. The hydrogen gas produced as the result of the corrosion reaction accumulates as bubbles that eventually detach from the surface and are collected in the top of the burette by displacing the solution contained in it. The volume of the H_2 evolved is then assessed by noting the level of the electrolyte inside the burette at various times during the experiment [99].

pH measurements It is also possible to assess the corrosion rate of dissolving Mg by chemical titration.
In this method, the pH of the electrolyte is maintained to a fixed value throughout the time of experimentation by titrating with an appropriate solution. The rationale behind this method is that, as the corrosion reaction proceeds, the pH will increase as a result of the cathodic half-reaction (see Eq.3.3) and the volume of titrant needed to maintain the pH constant allows for the amount of charge consumed to be determined [100].

Part III

Materials and methods

Chapter 4

Experimental equipments

This Chapter describes the experimental apparatus used to carry out machining trials on the biomaterials alloys under investigation. Three differents innovatives manufacturing technologies were applied in order to improve functional products of biomedical devices: i) cryogenic machining; ii) large strain extrusion machining; iii) ultrasonic vibration turning.
This Chapter not only reports a general overview of these manufacturing strategies but also provides details about the design process and the experimental procedure.

4.1 Cryogenic Machining

Cryogenic machining is demostrated to be an efficient methods to manufacture biomedical implants in order to obtain products with improved surface integrity (see Section 2.2).
In the following section the experimental setup for carrying out cryigenic machining operation is described in details.

4.1.1 Design of the equipment

The cryogenic experimental setup basic consists in a vacuum tank (Dewar) that is specifically designed to contain the liquid nitrogen at high pressure (15 bar).
The pressure of the liquid is generated by a cap of gas which consists in gasified nitrogen that pressurizes the liquid phase. The pressure is controlled and mantained at a constant level by means of a pressure control gas valve mounted on the top of the tank. When liquid nitrogen is introduced into Dewar, once it starts to gasify the repressuring system keeps the gas pressure at constant desired value which correspond at the pressure of the liquid emitted from the liquid phase connection. A pressure lieve valve is also installed on the Dewar to avoid the pressure to reach dangerous levels,

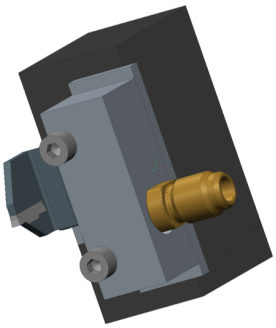

(a) *3D-view of the experimental setup designed for cryogenic cutting operations.*

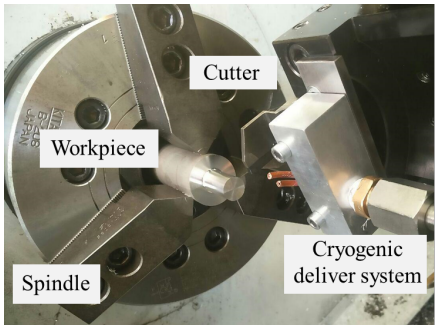

(b) *Experimental setup for cutting off operations.*

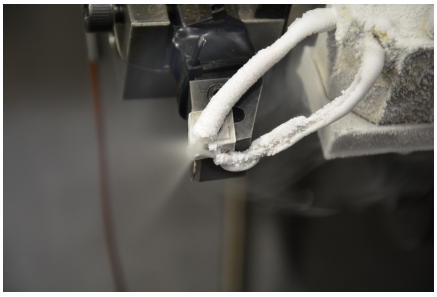

(c) *Magnified photo of the liquid nitrogen delivery apparatus.*

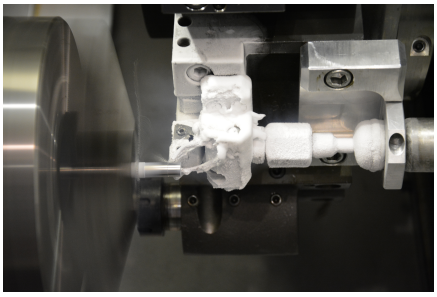

(d) *Cryogenic turning of cylindrical samples.*

Figure 4.1: Cryogenic machining set-up.

in particular during the summer season.
The liquid nitrogen is than carried towards the cutting zone through a vacuum insulated pipe, to avoid formation of gas bubbles into the cooling line, inducing annoying fluctuations and instability in the liquid flow. Between the Dewar and the vacuum insulated pipe, an electro actuated security valve was installed to stop the flow in case of emergency.

Liquid nitrogen is then supplied by means of two external copper nozzles, directed onto the rake and flank faces with a direction of 45°, supported by a specifically designed tool holder.
The resulted a mass flow is equal to 0.9 Kg/min. The latter was designed starting from taking the dimensions by reverse engineering of the turrets that are installed on the revolver of the used CNC lathe, namely the Mori Seiki^{TM} NL 1500.
An example of especially designed tool for cryogenic cutting off operations, is visible in Fig. 4.1b) together with the relative 3D model (Fig. 4.1a).
The copper capillary tubes present an internal diameter of 0.9 mm and they can be easily adjusted to cover the entire cutting zone (Fig. 4.1c).

In this way, the adopted solution can be suitable for all the cylindrical turning operations even carried out with different tool holders.
A representative image of the cryogenic machining processing is visible on Fig. 4.1d).

4.2 Large Strain Extrusion Machining

Large strain extrusion machining is demostrated to be an efficient methods to obtain nano crystalline grain size on the machined workpiece, therefore improving its surface integrity (see Section 2.3).
In the following section the experimental setup for carrying out large strain extrusion machining operation is described in details.

4.2.1 Background

A scheme of the LSEM process is shown in Fig. 4.2.
The cutting tool removes a depth, namely the undeformed chip thickness t_0 and width (w) of material, in form of a chip of controlled thickness t_c produced by a simultaneous machining-extrusion operation, thanks to the presence of a constraint across from the tool.
In this configuration, the LSEM tool moves into a rotating disk-shaped workpiece rotating at a constant cutting speed V_0.
The chip obtained in LSEM is a sheet produced directly from the bulk material in a single stage of deformation. In addition, contrary to conventional machining, the thickness of the chip, arbitrarily fixed a priori, on the basis of the constraint position, can be set smaller than t_0.
The chip compression ratio (λ) is defined as $\lambda = t_c / t_0$. In LSEM the deformation is highly localized and imposed in a narrow zone idealized as a shear plane: in these conditions the shear strain (γ) and shear strain rate (γ') can be estimated as follows according to [101],[102],[103].
It is worth to note that the extent of deformation imposed on the chip has a direct correspondence with the one found in the machined bar; therefore, the chip strain is a good indicator of the deformation in the machined bar [22].
The chip shear strain is determined by the chip compression ratio and tool rake angle (α), and can be calculated on the basis of 4.1:

$$\gamma = \frac{\lambda}{cos\alpha} + \frac{1}{\lambda * cos\alpha} - 2 * tan\alpha \tag{4.1}$$

A wide range of strain can be imposed to the chips by varying α and λ, while the shear strain rate can be varied modifying the cutting speed on the basis of Eq. 4.2 :

$$\gamma' = \frac{\gamma * V_0}{\triangle * \sqrt{3}} \tag{4.2}$$

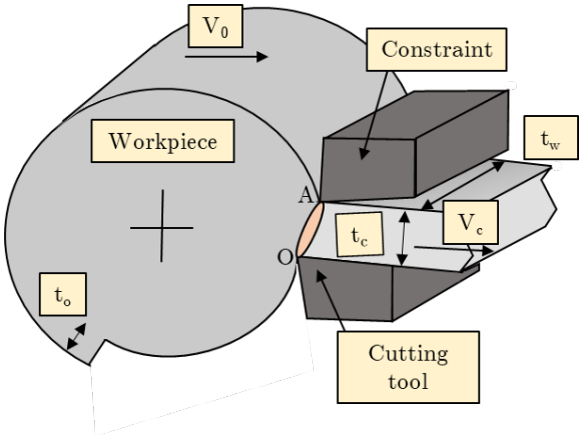

Figure 4.2: Scheme of the LSEM process.

where $\triangle$ represents the thickness of the deformation zone at the shear plane while γ is calculated through Eq. 4.1.
The thickness of the deformation zone typically decreases at increasing cutting speed; however, for a wide range of metals and for cutting speed higher than 100 mms^{-1}, $\triangle$ was found to be almost constant and equal to 50 μm, which was the value assumed in this study according to the imposed cutting speeds [104].

4.2.2 Design of the equipment

The design of the LSEM experimental setup started with the choice of the cutting tool. The requirements necessary for the potential cutting tool were the following:

1. The cutting tool must be suitable for machining magnesium alloys;
2. The presence of chip breaker must be avoided;
3. Rake angle must be high enough to avoid the collision with the workpiece.

The adopted cutting tool was a Sandvik Coromant^{TM} semi-finishing insert VBMW160404H13A, with rake and clearance angles of 0° and 5°, respectively (see Fig. 4.3).
Technical characteristics of VBMW160404H13A insert summarized on Table 4.1. Large strain extrusion machining requires an orthogonal cutting condition, therefore the following hypothesis must be fulfilled:

1. The cutting length of the cutting tool has to be larger than the thickness of the workpiece machined;
2. The cutting tool must be orthogonal to the workiece;

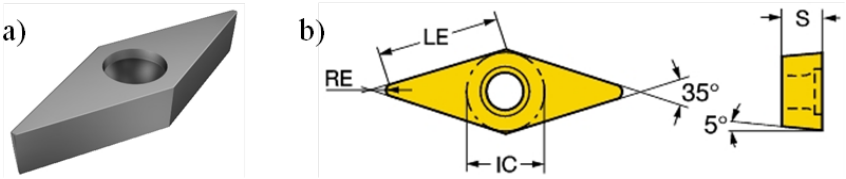

Figure 4.3: 3D-image of the VBMW160404H13A insert; b) characteristics angles of the VBMW160404H13A insert. Parameters are described on Table 4.1

.

Table 4.1: Technical characteristics of VBMW160404H13A insert

Length of the cutting tool (LE)	Grade	Coating	Rake angle
16.206 mm	H13A	Uncoat	5 deg

The hypothesis number 1) is was easily fulfilled by choosing a right thickness of the workpiece.
On the contrary, the hypothesis number 2) was accomplished by means of the presence of a wedge located on the base of the tool-holder.
In order to force the material to pass through the "extrusion" die formed by the bottom rake face and the top constraining edge, a constrain tool, made in hard material, has been designed. With the aim of control the chip thickness, the tool was equipped with two guides for a fine movement along both x and z axis.
Similarly to section 4.1, the application of liquid nitrogen, was performed by means of a specially designed tool. Since cutting operations were performed in orthogonal cutting configuration, the copper nozzles were directed on both side of the cutting tool.
An image of the experimental setup is reported on Fig. 4.4 .

4.3 Ultrasonic Vibration Cutting

Ultrasonic vibration cutting is demonstrated to be an efficient methods to obtain unique surface texture on the machined workpiece, therefore drastically modify its wettability and its response to wear (see Section 2.4).
In the following section the experimental setup for carrying out ultrasonic vibration cutting operations is described in details.
Eng. Eugenio Di Iorio took care of the design of the equipment.

4.3.1 Design of the equipment

The current UVT system was designed making use of a piezoelectric transducer, a sonotrode, a tool tip, a mechanical setup to fit in the turret of the Mori-Seiki^{TM} NL-1500 CNC lathe, and driving electronics.

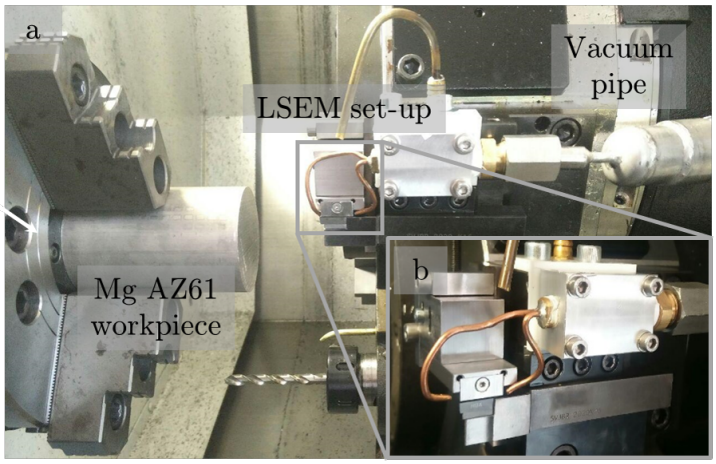

Figure 4.4: a) Experimental setup for LSEM process; b) magnification of the cryogenic deliver apparatus.

The transducer is a bolt clamped Langevin type [105]: two piezoelectric rings are preloaded under the action of an aluminium truncated cone shape and a cylindrical steel head.
Particular attention was paid to the sonotrode shape design as its performance directly affects the amplitude of the cutting tool.
The overall length of the sonotrode, known as ultrasonic horn, is, as first approximation, independent from its shape, and is the only parameter that identifies the natural resonance frequency, besides the speed of sound in the material.
On the other hand, the natural resonance frequency has to match the bare transducer resonance frequency within a narrow tolerance, in the order of half a kHz. In order to pursue this goal, an iterative measuring-adjustment experimental method was adopted, after a preliminary analytic modelling of the sonotrode behavior [106].
The cutting tool was firmly fixed to an aluminum tip offering a threaded hole to fit the sonotrode.
The scheme of the UVT system with indication of the different parts is shown in Fig. 4.5.
Analytical and numerical models suggested a starting value of the horn overall length in order to manufacture one of first attempt.
The minimum impedance method was used to check the horn resonance and match the transducer one.
The applied procedure consisted in monitoring the current crossing a reference 100 Ohm resistance in series with the piezoelectric transducer with the 2 channel digital oscilloscope Tektronix TBS1052B^{TM}: the monitored frequency-dependent current was variable and the power was supplied by a signal generator (Siglenet SDG800^{TM}) set up to feed a sine sweep of 4

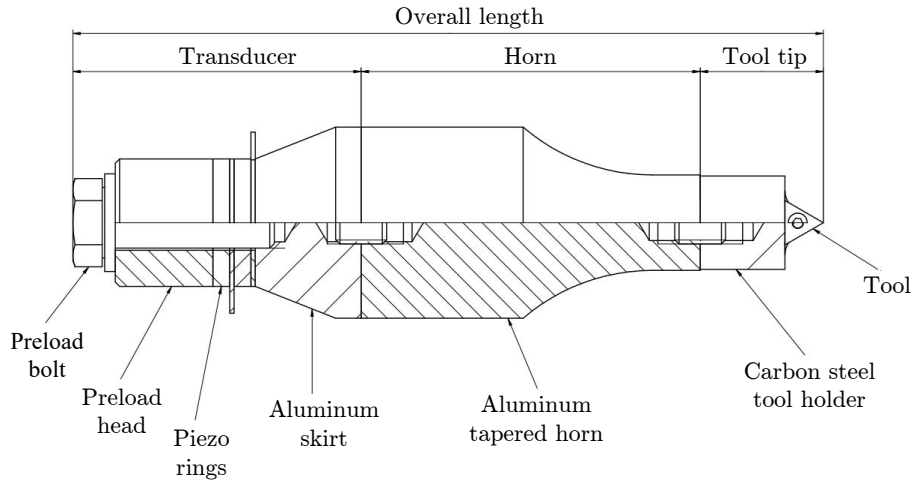

Figure 4.5: Sketch of the UVT system.

Vpp constant amplitude starting at 20 kHz and ending at 40 kHz for a total duration of 100 microseconds. The current trend was registered through the oscilloscope and the resulting plot showed sharp peaks and troughs representing the minimum and maximum impedance frequencies, respectively.
The overall length of the sonotrode had to be shortened until the minimum impedance point was located in correspondence of the natural resonance frequency of the transducer previously measured with this method.
This method helped in identifying in a few steps the right horn length but did not provide any useful information about the impedance real value.
The impedance value of the transducer-horn-cutting tip system versus the frequency spectra is indeed a fundamental data set to design the ultrasonic piezoelectric driver. In order to estimate the impedance value of the sonotrode-piezotransducer assembly, the voltage magnitude and the phase shift between the 2 channels of the oscilloscope were measured: the first channel of the scope monitored the voltage drop of the transducer-sonotrode assembly with a 100 Ohm resistance in series, while the transducer poles were just wired to the second channel. The signal generator (Siglenet SDG800) was operated to feed a sine signal by manually varying its period around the minimum impedance frequency, which was previously located: in such a way, it was possible to draw the impedance versus frequency graph and reveal its minimum of 86 Ohm at 30 kHz.
Fig. 4.6 shows the workflow for the overall design of the UVT system, while

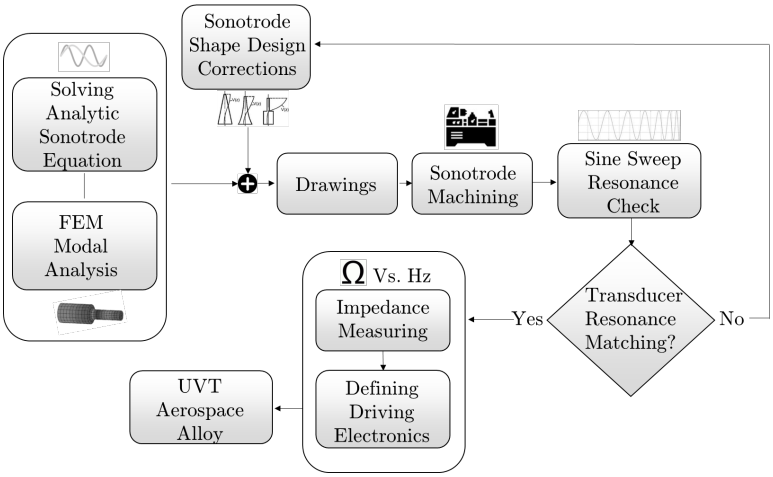

Figure 4.6: Workflow of the design procedure.

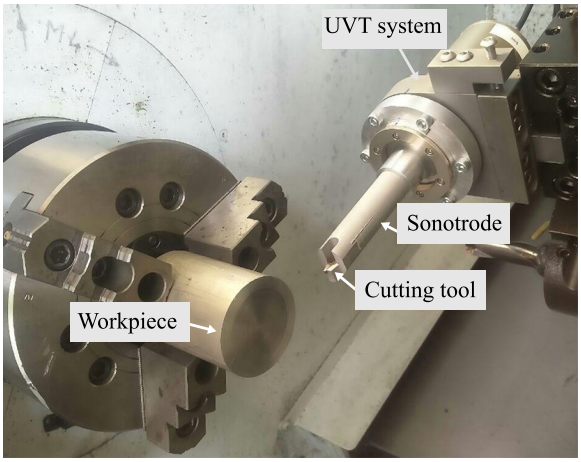

Figure 4.7: Experimental set-up for UVT.

Fig. 4.7 reports the experimental apparatus for UVT tests.

Chapter 5

Machining trials

In this Chapter, the different machining trials adopted for the case studies investigated are described. Data on the experimenal campaign and of materials, are preceded by a brief introduction which explains the reasons behind the studies. Data on titanium alloys were presented first, then followed by the ones pertain to magnesium alloys. Three applications for each biomaterials are described.

5.1 Titanium alloys

Table 5.1 summarizes the different cases studies investigated for titanium alloys.

5.1.1 Ti-APP#1

The wear behaviour of hip implants subjected to cyclic stresses due to the human gait cycle strictly depends on their surface condition, which is usually generated during the final machining steps of the process chain.
During the implant service life, wear phenomena induce the formation of wear debris that are harmful for the patients health since they can cause osteolysis and provoke inflammatory reactions with the surrounding tissues. A reduction of wear and, consequently, of debris generation is highly desirable, especially for young and active patients [107] that have a long expectation of life.
This has recently contributed to renew the interest in Metal-on-Metal (MoM) connections, composed by a Ti6Al4V acetabular cup and a CoCrMo femoral head, as an alternative to the conventionally used metal-on-PolyEthylene (PE) ones, as it was demonstrated that the former were characterized by approximately 40-100 times lower wear rate than the latter [108].
The scientific literature presents several studies addressing either the influence of the manufacturing parameters on the obtained surface characteristics

Table 5.1: Test identification.

Test ID	Title of the work
Ti-APP#1	Machining-conditioning to improve the wear resistance of Ti6Al4V surfaces for human hip implants
Ti-APP#2	Influence of the machining cooling strategies on the dental tribocorrosion behaviour of wrought and Additive Manufactured Ti6Al4V
Ti-APP#3	Influence of the machining cooling strategies on coating adhesion on titanium substrates for biomedical applications

(see Section 2.2 on page 12), or the effect of the surface characteristics on the service life performances (see Section 2.6.1 on page 20).
However, none of the aforementioned studies presented a clear correlation between the surface roughness parameters and surface integrity, generated by the adoption of specific process parameters, and the wear volume loss in a human-like environment, which is the objective of the present research work.
To this aim, Ti6Al4V acetabular cups were machined under wet and cryogenic cooling conditions varying the number of finishing passes to obtain different surface finishes; afterwards, their wear behaviour was analysed making use of an in-vitro wear test and a novel procedure for the wear volume evaluation, considering the complete information coming from the measured topography.

Ti-APP#1: Materials

The metal alloys usually employed in MoM hip replacements are the Ti6Al4V titanium alloy for the acetabular cups and the CoCrMo cobalt alloy for the femoral heads.
In this study, the ASTM F1537 CoCrMo cobalt alloy was provided in form of a 15 mm diameter bar, which was turned, ground, polished, and then cut into cylinders with a diameter of 12.5 mm diameter and length of 5 mm. The cylindrical surface roughness was Ra =0.08 $\pm$0.01 μm, comparable to that of most commercial head devices [109].
The Ti6Al4V titanium alloy was manufactured through the Additive Manufacturing (AM) technology known as Electron Beam Melting (EBM) by using an ARCAM^{TM} Q10 machine in form of 40 mm diameter and 180 mm

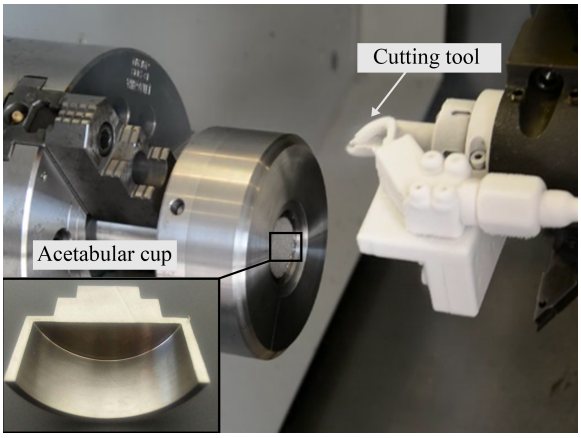

Figure 5.1: Experimental set-up for the cryogenic turning of the EBM Ti6Al4V cups.

long cylinders.

Ti-APP#1: Machining tests

The Ti6Al4V acetabular cups in a simplified geometry, visible on the box of Fig. 5.1, were machined from the EBM cylinders on a Mori Seiki^{TM} NL 1500 CNC lathe equipped with a specially designed line assembled to fulfil cryogenic cooling using liquid nitrogen as described in Section 4.1.1.
The experimental set-up is shown in Fig. 5.1.
A Sandvik Coromant^{TM} A20M-SDXCR 11-R boring bar with a DCGT 11 T3 08-UM GC1105 coated carbide insert supplied by the same manufacturer was used as cutting tool.
A fresh cutting edge was adopted for each test, in order to avoid the influence of the tool wear on the machined surface characteristics.
The machining parameters under investigation were the cooling strategy and the number of passes needed to obtain the final shape.
Cryogenic machining has appeared to be a suitable technique for manufacturing biomedical devices and it has demonstrated to be capable of improving the machined surface integrity, as reported on Section2.2.
On the contrary, there is no evidence in the literature about the effect of the number of passes on the surface integrity. As the cryogenic machining is a severe plastic deformation process that significantly modifies the surface and sub-surface characteristics of the workpiece until several microns beneath its surface, it is worth to evaluate the effect of the number of passes on the basis of the adopted cooling strategy.
The acetabular cups were machined to a final internal diameter equal to 34 mm according to standard commercial dimensions. After a roughing operation, two finishing approaches were adopted: in one case, the final diameter was reached with a single finishing pass of 0.25 mm, while in the other, five

Table 5.2: Experimental plan adopted for the turning tests.

Ti-APP#1		
Test ID	Cooling condition	Number of passes
Wet-1 passes	Wet	1-pass
Wet-1 pass	Wet	5-passes
Cryo-1 pass	Cryogenic	1-pass
Cryo-5 passes	Cryogenic	5-passes

finishing passes were used, each of 0.25 mm. The aforementioned strategy was selected as it was the result of a preliminary experimental campaign in which the number of passes was varied, namely from one to five with a pitch equal to one. It was decided to choose one and five passes because they mostly affected the resulting surfaces, with a special reference to the surface topography.
The other chosen cutting parameters were a cutting speed equal to 60 (m/min) and a feed rate equal to 0.1 (mm/rev). The machining tests were performed under wet and cryogenic cooling and repeated five times for each cutting condition.
Table 5.2 summarizes the experimental plan adopted for the turning tests.

5.1.2 Ti-APP#2

As seen in Section 3.1.3, titanium alloys is frequently used as dental implants, even if cyclic micro-movements at the implant/bone interface or implant/abutment interface may occur, inducing significant wear, which, together with the chemical interactions with the environment, can lead to the destruction of the repassivation protective layer causing a progressive material loss and to a premature replacement of the implant.
Each chewing process can be regarded as a tribocorrosion cycle since sliding occurs between the tooth and the food particles in presence of corrosive saliva. The repeated removal of the oxide films induced by the chewing cycles produces wear at the implant/abutment interface leading to adverse biological reactions and, possibly, to the mechanical failure of the device.
Alternative processing routes, together with different processing techniques are being investigated to increase the wear resistance of the titanium alloys. The use of cryogenic cooling during machining has been demonstrated to be an effective mean to enhance the surface properties of implant devices, based on the findings of the results reported on Section 2.2 and of the results of the previous work Ti-APP#1 whose results are described in section 8.1.
For these reasons, in this work, different cooling strategies were applied in

machining wrought and AM Ti6Al4V samples and their influence on the alloys tribocorrosion behaviour was investigated and critically assessed.

Ti-APP#2: Materials

The wrought Ti6Al4V samples were machined into cylinders from a commercially available annealed bar of 30 mm diameter and 200 mm of height. The AM Ti6Al4V samples were machined into cylinders from a cylindrical billet produced EBM using an ARCAM^{TM} Q10 machine. Each billet was manufactured with the symmetry axis parallel to the growing direction, with a diameter of 30 mm and a height of 180 mm.
Both the wrought and EBM Ti6Al4V machined cylinders had a diameter of 20 ($\pm$0.02 mm) and a length of 5 ($\pm$0.02 mm). The Ti6Al4V cylinders were made to slide against zirconia plates in order to recreate an actual biotribological pair.
The zirconia ZrO_2 was chosen as counterpart material because it is commonly used for the fabrication of dental implant abutments [110].

Ti-APP#2: Machining tests

The machining tests were conducted on the Mori Seiki^{TM} CNC lathe equipped with a special designed line assembled to fulfil the cryogenic cooling (see Section 4.1.1). The adopted cutting tool was a semi-finishing coated tungsten carbide insert CNMG1-20404SM-GC1105 (substrate composition: 93%WC and 7%Co) with a radius of 0.4 mm, mounted on a PCLNR/L tool holder with an approach angle of 75°, both supplied by Sandvik Coromant^{TM}. The cutting tool consisted of a fine grain WC substrate, giving good heat and plastic deformation resistance; while the coating consisted of a TiAlN layer deposed by PVD, allowing good toughness, uniform flank wear, and overall high machining performances. The resultant rake and clearance angles were equal to 7° and 0°, respectively. Both the insert grade and micro geometry were chosen on the basis of the tool manufacturers advices for machining titanium alloys.
In order to avoid the influence of the tool wear on the surface topography of the machined cylinders, a fresh cutting edge was adopted for each test.
The values of the cutting speed and feed rate adopted for the tests, namely 80 m/min, and 0.1 mm/rev, respectively, were chosen on the basis of a previous study [111]. The depth of cut was maintained constant and equal to 0.25 mm in order to achieve a semi-finishing cutting condition.
The machining tests were performed with three different cooling conditions, namely, dry, wet and cryogenic.
The experimental plan for the machining tests is reported in Table 5.3.

Table 5.3: Experimental plan for the machining tests.

Ti-APP#2	
Processing route	Cooling condition
Wrought	Dry
EBM	Dry
Wrought	Wet
EBM	Wet
Wrought	Cryogenic
EBM	Cryogenic

5.1.3 Ti-APP#3

Titanium and titanium alloys are usually employed in the manufacturing of both orthopaedic and dental implants, thanks to their low density, high strength-to weight ratio, resistance to chemical degradation, and biocompatibility (see Section 3.1). Unfortunately, wear resistance and bioactivity of especially pure titanium are relatively low. To this regard, the use of a bioactive coating layer might enhance the implant durability and osteoconductivity. Traditional biocoatings are made of bioceramics and bioglasses, which, however, usually suffer of poor adhesion to the substrate.
The latter is realized through machining operations, therefore, is noticeable influenced by the process parameters adopted as reported in Section 2.1 on page 9. In this context, the objective of the present work is to further improve the adhesion between the biomedical coating and pure titanium substrate by means of a suitable preparation of the substrate surface by means of using different process parameters.
Cryogenic cooling represents an innovative efficient solution for machining biomedical implants on the basis of results of Ti-APP#1 (see Section 8.1 on page 95) and Ti-APP#2 (see Section 8.2 on page 105), while feed, is recognized to condition roughness in a substantial way (see Section 2.1 on page 9).
In this work, the effectiveness of using cryogenic machining and different feed to prepare the surfaces of Cp-Ti samples before the sphene coating application was evaluated in terms of coating deposition and adhesion and compared with a conventional processing route making use of wet machining.

Ti-APP#3: Materials

The dental implant prototypes were machined from fully annealed bars of commercially pure titanium (Grade 2), with diameter of 10 mm and length

Table 5.4: Experimental plan adopted for the turning tests.

Ti-APP#3		
Test ID	Feed (mm/rev)	Cooling condition
Sample A	0.1	Wet
Sample B	0.2	Wet
Sample C	0.1	Cryogenic
Sample D	0.2	Cryogenic

of 200 mm.

Ti-APP#3: Machining tests

The Mori Seiki^{TM} CNC lathe was used to machined the titanium alloy.
After an initial roughing turning operation to reduce the diameter to 5 mm, a semi-finishing one was carried out on the lathe in order to have a final bar diameter of 4 mm, the same of commercially available dental implants in pure titanium. For the last operation, different process parameters were adopted.
In order to evaluate the effect of the machined surface roughness on the coating adhesion performances, two feeds were adopted, namely 0.1 (mm/rev) and 0.2 (mm/rev). These values were chosen in order to achieve a surface finish condition comparable to the one of the commercial dental implants.
In order to evaluate the effect of machining cooling conditions, tests were performed using of a standard oil-based emulsion and liquid nitrogen.
The other cutting parameters were fixed for all the tests, namely a depth of cut equal to 0.25 mm, and a cutting speed equal to 30 m/min.
Tests were performed three times in order to assure repeatability.
The experimental plan for the machining tests is reported in Table 5.4.

5.2 Magnesium alloys

Table 5.5 summarizes the different cases studies investigated in the case of magnesium alloys.

5.2.1 Mg-APP#1

As seen in section 2.7.1, a proper surface modification may enhance the corrosion resistance of magnesium alloys to a great extent.
Machining can be used to induce a severe improvement on surface integrity without adding any additional step in the process chain.

Table 5.5: Test identification.

Test ID	Title of the work
Mg-AP1	Machining-induced surface transformations of magnesium alloys to enhance corrosion resistance in human-like environment
Mg-AP2	Large strain extrusion machining of magnesium alloys for biomedical applications
Mg-AP3	Ultrasonic vibration assisted turning of magnesium alloys for biomedical applications

The primary objective of this work is to give a fundamental insight into the role of machining-induced surface transformations on the surface micro-topography, and sub-surface mechanical and microstructural properties in enhancing the corrosion performances of AZ31 magnesium alloy, making it suitable for the manufacture of temporary prosthetic devices.
In support to this objective, thorough physical characterizations of the transformed surfaces integrity were carried out, and correlations to corrosion resistance were made.

Mg-APP#1: Materials

The workpiece material was AZ31 magnesium alloy, supplied in bars of 30 mm diameter and 180 mm length, with an average grain size of 15 μm.

Mg-APP#1: Machining tests

The turning tests on Mg AZ31 alloy were carried out on a Mori Seiki^{TM} lathe, using a Sandvik Coromant^{TM} semi-finishing insert VCEX110301LF1125.
The depth of cut was set to 0.25 mm and cutting speed to 100 m/min. The feed was varied, adopting 3 different values, namely 0.2, 0.1 and 0.01 mm/rev, all within the range recommended by the tool manufacturer.
The tests were conducted under dry and wet conditions, the latter using the machine tool conventional cutting fluid, as well as under cryogenic cooling, using a specially designed supply that delivered the liquid nitrogen to both the tool rake and flank faces as described in 4.1.1 .
Each test was carried out using a fresh cutting edge and repeated three times.
Table 5.6 reports the experimental plan for the machining tests.

Table 5.6: Experimental plan for the machining tests.

Mg-APP#1			
Feed (mm/rev)	Cooling condition	Cutting speed (m/min)	Depth of cut (mm)
0.2	Dry	100	0.25
0.1	Dry	100	0.25
0.01	Dry	100	0.25
0.2	Wet	100	0.25
0.1	Wet	100	0.25
0.01	Wet	100	0.25
0.2	Cryogenic	100	0.25
0.1	Cryogenic	100	0.25
0.01	Cryogenic	100	0.25

5.2.2 Mg-APP#2

Intense grain refinement pursued by machining is an efficient strategy used to increase corrosion resistance of magnesium alloys, as concluded by the previous research studies (see Section 2.7.1 on page 23). It was also confirmed by the results of the Mg-APP#1 work (see Section 9.1 on page 127), in which the formation of nano-crystalline layer together a compressive residual stress state induced by cryogenic machining was found to be beneficial for corrosion resistance.
In this work, LSEM is applied to machining of the AZ61 magnesium alloy by exploiting the severe deformation induced on both, the workpiece and the chips, to increase the corrosion resistance in human-like environment of magnesium alloys.
Different cutting speeds and cooling strategies were applied during LSEM of AZ61 and their effects on the surface integrity and corrosion behavior of both the machined workpiece and the LSEM-ed chips were investigated. It is worth to note that liquid nitrogen as cooling medium, since it was proved to be an efficient solution to improve surface quality of the workpiece (Section 2.2).

Mg-APP#2: Materials

The material objective of the study was the commercially available AZ61 magnesium alloy supplied in form of bars of 60 mm of diameter and 500 mm of length. The bars were subjected to an annealing treatment at 360°C for

Table 5.7: Cutting characteristics for the LSEM tests.

Mg-APP#2	
Rake angle (α_1)	0°
Clearance angle (α_2)	5°
Underformed chip thickness (t_0)	0.2 mm
Controlled chip thickness (t_c)	0.25 mm
Chip compression ratio (λ)	0.25 mm
Constraint tool corner radius (C_r)	0.4 mm

2 hours, which led to a homogenous average grain size of 15 μm.

Mg-APP#2: Machining tests

The adopted undeformed chip thickness t_0 was 0.2 mm while the λ was set equal to 1.25.
Since the aim of the study was to investigate the effect of cryogenic cooling applied to LSEM, λ was kept fixed for all the tests. The constraint tool corner radius was set equal to 0.4 mm in order to maximize the effective strain that could be produced on the workpiece, according to [22].
Table 5.7 summarizes the cutting characteristics adopted for the experimental campaign.
Different cutting speeds, namely 30 m/min, 60 m/min and 120 m/min, and different cooling conditions, namely dry cutting and cryogenic cooling, were applied and their effect on the surface integrity and corrosion resistance of the workpiece was investigated. It is worth to notice that also a standard cutting fluid was initially used, however the machine tool system sprayed it at too high pressure, without any chance of modification, leading to the formation of discontinuous, thus not suitable, chips.
The LSEM experiments were repeated three times in order to assure repeatability.
Table 5.8 summarizes the experimental plan.

5.2.3 Mg-APP#3

Surface textures play an important role to determine the product in-service performances, namely the corrosion behaviour in the case of magnesium alloys.
In the previous research study Mg-APP#1 (see Section 9.1.3 on page 131), it was demonstrated that lower wettability, induced by the state of the surface, can be beneficial to improve corrosion resistance, since it generates surfaces less prone to be attacked by body fluids.

Table 5.8: Cutting characteristics for the LSEM tests.

Mg-APP#2		
Test ID	Cutting speed (m/min)	Cooling condition
D1	30	Dry
D2	60	Dry
D3	120	Dry
C1	30	Cryogenic
C2	60	Cryogenic
C3	120	Cryogenic

In this study, UVT was applied to machine magnesiuma alloys with the aim of achieving a distinctive structured texture on the surface, tailoring wettability. Different cutting speeds and depth of cut were applied during machining of AZ31 and their effects on the surface integrity, wettability and corrosion behavior were investigated.

Mg-APP#3: Materials

The material under investigation was the commercial AZ31B magnesium alloy, was supplied in form of bars of 30 mm of diameter.

Mg-APP#3: Machining tests

The machining tests were conducted on the Mori Seiki NL-1500 CNC turning center equipped with a customized steel structure for holding the developed UVT system.
This structure was designed to allow a fine height adjustment of the tool cutting edge in the lathe Y-axis (center-line) housing in a standard 20 mm tool shank slot. Referring to the lathe coordinate system, the alignment of the sonotrode axis in the X direction was obtained with a precision set-square.
Before ultrasonic turning, the magnesium alloy bar was prepared with a CT finishing pass with the same UVT system where ultrasonic vibration was turned off in order to guarantee the nominal value of imposed depth of cut.
Fig. 5.2 shows the direction of motion of the UVT system during cutting.
Table 5.9 summarizes the cutting parameters applied in the experimental campaign in terms of cutting speed, depth of cut and feed.

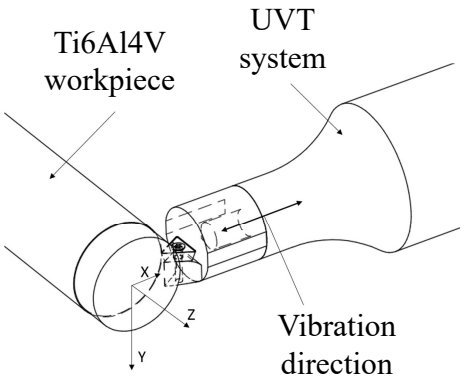

Figure 5.2: UVT vibration axis along X axis, feed along Z axis.

Table 5.9: Cutting characteristics for the UVT tests.

Mg-APP#3				
Test ID	Turning	DoC (mm)	Cutting speed (m/min)	Feed (mm/rev)
Sample 1	CT	0.05	100	0.05
Sample 2	UVT	0.05	100	0.05
Sample 3	CT	0.05	200	0.05
Sample 4	UVT	0.05	200	0.05
Sample 5	CT	0.1	100	0.05
Sample 6	UVT	0.1	100	0.05
Sample 7	CT	0.1	200	0.05
Sample 8	UVT	0.1	200	0.05

Chapter 6

Characterization after machining

In this Chapter, the different techniques used for characterized samples after machining into the different case studies are described. A fully characterization of mechanical properties and of surface finish is carried out by means of microstructure, hardness, residual stresses, surface defects evaluation and surface roughness measurements.
These techniques are subdivided on the basis of the different biomaterial investigated.

6.1 Introduction

It is well known that machining has a remarkable effect on surface integrity of the workpiece (see Section 2.1).
Surface integrity is the sum of all of the elements that describe all the conditions existing on a surface [112], and it is usually composed two aspects.
The first aspect refers to the surface metallurgy of the workpiece which describes the nature of the altered layers below the surface with respect to the base material.
The second aspect refers to the surface topography which describes the roughness, lay or texture of the outermost layer of the workpiece.
The second aspect refers to the surface metallurgy of the workpiece which describes the nature of the altered layers below the surface with respect to the base material.
In other words, SI represents the assessment of the impact of manufacturing processes on the properties of the workpiece material. Indeed, after a machining operation, the subsurface layers lie in a different condition to those of the body of the material. This altered zone is usually referred as altered material zone (AMZ).
Changes can be caused by chemical, thermal, elettrical or mechanical en-

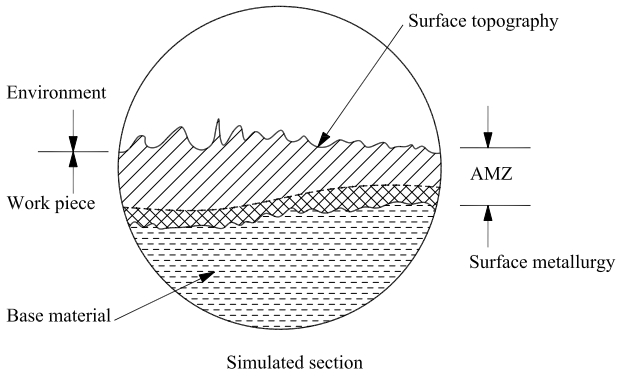

Figure 6.1: Schematic rapresentation of the material state after a machining process.

ergy and affect both the physical and the metallurgical properties of the material [113]. Fig. 6.1 describes the state of the surface after a machining process.
The aim of this chapter is to briefly describe the overall type of characterization which were carried out on different machined samples in order to assess, as much as possible, the impact of machining operations on surface integrity of the workpiece.

6.2 Titanium alloys

In this section, characterization techniques carried out on titanium samples after machining operations will be presented. Characterization methods are divided into two parts which deals with the impact of machining on the surface metallurgy and mechanical properties and on the surface finish.
In this part, characterization tecniques applied to titanium alloys are described.

6.2.1 Microstructural and mechanical characterization

In this section, characterization techniques aimed to evaluate the effect of manufacturing operations on the microstructure and mechanical properties of the machined titanium samples are presented.

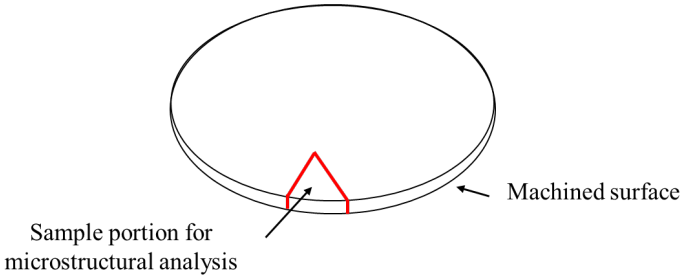

Figure 6.2: Sectioning of the metallurgical sample and view for microstructural analysis.

Microstructure evaluation

Metallurgical titanium samples were cut from the machined samples for metallographic investigations.
The inspected zone is schematically reported on Fig. 6.2.
After mounting, grinding and polishing, the Krolls etchant was used to reveal the grain boundaries.
The microstructure was observed using a FEI QUANTA 450^{TM} Scanning Electron Microscope (SEM) equipped with a Back-Scattered Electron (BSED) detector.
In order to quantify the extent of the machining-affected layer, the following procedure was adopted: the layer thickness was measured from the SEM images recorded at 2000X magnification every 15 μm; the measures were repeated in two different zones of the sample, and finally the average value was calculated.

Hardness measurements

Vickers micro-hardness measurements were performed using a Leitz Durimet^{TM} micro-hardness tester with a load of 50 ($\pm$ 0.5) gr for 30 s; three values were recorded for each measurement point and the average value reported. The hardness measurements were taken every 30 μm from the machined surface to a depth of 200 μm.

Residual stresses determination for titanium alloys

The residual stresses on the machined surfaces were measured by means of the X-Ray Diffraction (XRD) technique using the sin2ψ method [114]. The XRD analysis was carried out on an Enixè^{TM} TNX diffractometer, using CuKα radiation at 85 μA and employing 9 tilt angles (ψ). The residual stresses along the axial and circumferential directions were measured on the surface and at a depth of 25 μm below the surface, by removing the material layers through an electro-polishing process to avoid modifications of the machining-induced stresses.

6.2.2 Surface finish characterization

A large amount of surface roughness parameters can be taken into consideration in order to describe the machining induced surface.
In the following section, a brief description of the parameters used in this thesis is given. All parameters are included in ISO 13562-2 standard.

Surface texture parameters

Height parameters

Arithmetic Mean Height (S_a)
The arithmetic mean height or Sa parameter is defined as the arithmetic mean of the absolute value of the height within a sampling area and it is defined by Eq. 6.1:

$$S_a = \frac{1}{A} \iint_A z(x, y)\, dx\, dy \tag{6.1}$$

Skewness (S_{sk})
Skewness is the ratio of the mean of the height values cubed and the cube of Sq within a sampling area, as defined by Eq. 6.2:

$$S_{sk} = \frac{1}{S_q^3} \frac{1}{A} \iint_A z^3(x, y)\, dx\, dy \tag{6.2}$$

This parameter can be positive, negative or zero, and is unit-less since it is normalised by Sq.
The Ssk parameter describes the shape of the topography height distribution. For a surface with a random (or Gaussian) height distribution that has symmetrical topography, the skewness is zero. The skewness is derived from the 20 F. Blateyron amplitude distribution curve; it is the measure of the profile symmetry about the mean line.
This parameter cannot distinguish if the profile spikes are evenly distributed above or below the mean plane and is strongly influenced by isolated peaks or isolated valleys.
Skewness represents the degree of bias, either in the upward or downward direction of an amplitude distribution curve. A symmetrical profile gives an amplitude distribution curve that is symmetrical about the centre line and an unsymmetrical profile results in a skewed curve.
The direction of the skew is dependent on whether the bulk of the material is above the mean line (negative skew) or below the mean line (positive skew).
Kurtosis (S_{ku})
The Sku parameter is a measure of the sharpness of the surface height distribution and is the ratio of the mean of the fourth power of the height values

and the fourth power of Sq within the sampling area, as defined by Eq. 6.3:

$$Sku = \frac{1}{S_q^4}\frac{1}{A}\iint_A z^4(x,y)\,dx\,dy \tag{6.3}$$

Kurtosis is strictly positive and unit-less, and characterises the spread of the height distribution.
A surface with a Gaussian height distribution has a kurtosis value of three. Unlike Ssk, use of this parameter not only detects whether the profile spikes are evenly distributed but also provides a measure of the spikiness of the area.
A spiky surface will have a high kurtosis value and a bumpy surface will have a low kurtosis value.
The Ssk and Sku parameters can be less mathematically stable than other parameters since they use high order powers in their equations, leading to faster error propagation.

Function related parameters

Height Distribution and Material Ratio Curve

The height distribution can be represented as a histogram of the surface heights that quantifies the number of points on the surface that lie at a given height. The material ratio curve is the cumulative curve of the distribution.
The material ratio curve is counted from the highest point on the surface (where the curve equals 0 %) to its lowest point (where the curve reaches 100 %). The equivalent lined is defined as the secant line of an areal material ratio curve (obtained from subtracting the curve at areal material ratio difference of 40%) from areal material ratio of 0%, the position that has the least steep secant is called the center portion of the areal material ratio curve. The equivalent line is the line where the sum of squared deviation in the vertical-axis direction is the smallest in the center portion. The core surface (Sk) is obtained by removing the predominant peaks and valleys (portions not included in the range of heights at an equivalent line areal material ratio of 0% to 100%) from the definition area of the scale limited surface.
The peaks with a height above the core surface are called reduced peaks (Spk) and the valleys below the core surface are called reduced valley (Svk).
An example of calculation of functional parameters are given in Fig. 6.3.

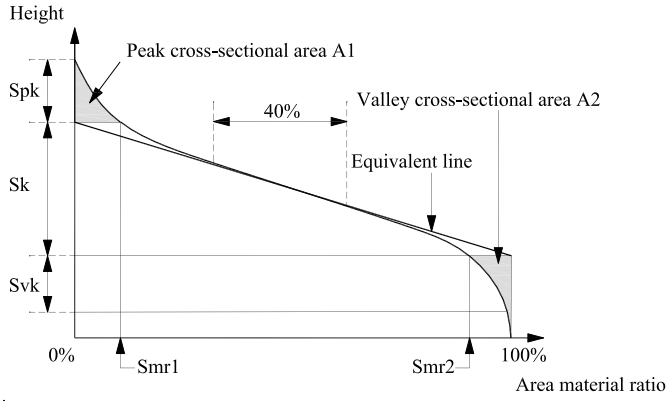

Figure 6.3: Graphical construction of Sk parameters

Spatial parameter

Autocorrelation Function (ACF)

The autocorrelation function (ACF) evaluates the correlation of a part of an image with respect to the whole image.
The ACF is defined as a convolution of the surface with itself, shifted by (τ_x, τ_y) (Eq. 6.4):

$$ACF(\tau_x, \tau_y) = \frac{\iint_A z(x,y)z(x-\tau_x, y-\tau_y)\,dx\,dy}{\iint_A z(x,y)^2\,dx\,dy} \tag{6.4}$$

The ACF corresponds to the autocovariance normalised by Sq^2. The ACF produces a value between -1 and $+1$ for each point on the surface. An ACF of $+1$ means a perfect correlation and zero means no correlation. The maximum of the ACF is always at the centre (for a zero shift).
The ACF is used to study periodicities on a surface, i.e. when a texture motif is reproduced several times on the surface, or is used to assess the isotropy of a surface.

Autocorrelation Length (Sal)

The autocorrelation length, Sal, is defined as the horizontal distance of theACF(tx, ty) which has the fastest decay to a specified value s, with $0 \leq s < 1$. The Sal parameter is given by Eq. 6.5:

$$Sal = min\sqrt{(\tau_x)^2 + (\tau_y)^2} \tag{6.5}$$

The Sal parameter is a quantitative measure of the distance along the surface by which a texture that is statistically different from that at the original location would be found.

Surface topography examination

The machined surface textures were measured using a Sensofar^{TM} Plu-Neox optical profiler with a 20x magnification Nikon^{TM} confocal objective. Data processing, filtering and evaluation of the surface texture parameters were performed according to the ISO 25178-2:2012-Part 2.
Different process parameters were analyzed on the basis of the applications. For each application, are listed below the parameters that were took into consideration.

Ti-APP#1: Surface roughness parameters evaluated

The following surface texture parameters were considered:

- Arithmetical mean height of the scale-limited surface (Sa), the most popular areal parameter, commonly reported also in hip-replacements wear studies [44] and representing the baseline for comparison with other research works.

- Core roughness depth (Sk), a parameter representing the working part of the surface, which, therefore, is correlated to the tribological performances [115].

- Reduced dale height (Svk), an effective parameter to describe the relevance of valleys that can affect the fluid retention in wet applications [116].

- Reduced peak height (Spk), a parameter giving information about the damaging top portions of the surface which influence the initial period of sliding in which the peaks are gradually worn out.

- Skewness of the scale-limited surface (Ssk), showing whether a surface is dominated by peaks or valleys, measuring the symmetry of the profile about the mean line [117], [118]. Even though rarely reported in wear studies, it was indicated as a significant parameter for hip replacement wear prediction [115].

- Kurtosis (Sku), a parameter that describes the sharpness of the surface height distribution [118].

Surface defects examination

The machined surface defects were examined using SEM. At least ten images, taken in different zones, and acquired at different magnification, namely 500X and 1000X, were used to characterized the sample surface.

6.3 Magnesium alloys

In this section, characterization techniques carried out on magnesium samples after machining operations will be presented.
Characterization methods are divided into two parts which deals with the impact of machining on the surface metallurgy and mechanical properties and on the surface finish.
In this part, characterization tecniques applied to magnesium alloys are described.

6.3.1 Microstructural and mechanical characterization

In this section, characterization techniques aimed to evaluate the effect of manufacturing operations on the microstructure and mechanical properties of the machined magnesium samples are presented.

Microstructure evaluation for magnesium alloys

Similarly to the previously described procedure, metallurgical Mg samples were cut from the machined cylinders.
After cold mounting, grinding and polishing, acetic and picric acid aqueous solution was used as the etchant to reveal the grain boundaries.
The microstructure observations were conducted using a Leica DMRE^{TM} optical microscope equipped with a high definition digital camera and SEM.
In the case of magnesium alloys, samples were further investigated by means of TEM. Samples were extracted from the machined workpieces for TEM. The cross-sectional TEM samples were prepared using a FEI^{TM} Nova 200 dual-beam Focused Ion Beam (FIB) system. The TEM lamellas were then ion-milled with a 30 kV beam and finally polished at 5 kV. After reaching a thickness of $\sim$ 100 nm, a Fischion^{TM} NanoMill was used to further clean the FIB damaged surface at both sides.
Selected Area Diffraction and Bright Field (BF) TEM imaging were performed at 300 keV using a Hitach^{TM} HF3300 TEM.

Hardness measurements for magnesium alloys

The same procedure adopted for titanium samples was adopted for magnesium's ones.
Moreover, nano-hardness and indentation modulus at the surface of the machined samples were measured with a diamond Berkovich indenter tip using the Hysitron^{TM} TriboIndenter.
A minimum of 20 nano-indentations was performed for each sample with a maximum load of 25 mN and data acquisition frequency of 5 Hz.

Residual stresses determination for magnesium alloys

The residual stresses were determined with CuK α-radiation using the (2,1,3) interference lines. The analysis was based on the sin2ψ-method for which the lattice spacings d were measured at five ψ angles between $-35°$ and $+35°$.
Young's modulus and Poissons ratio were set to 45 GPa and 0.25, respectively, for the calculation of the residual stresses.
The measurements were performed using a Spider^{TM} X GNR portable diffractometer working at 30 KV and 90 μA. The counting time for each of the five measures at the different ψ -angles was 500 s. The depth distribution of the residual stresses was determined by electrolytic removal of thin surface layers and subsequent X-ray measurements.
The electrolytic polishing used a solution containing 90 ml of water, 730 ml of ethanol, 100 ml of butoxyethanol and 78 ml of perchloric acid working at 18 V for 30 s at 20°C.

6.3.2 Surface finish characterization

The same procedure for titanium was adopted for magnesium alloys.

Mg-APP#1 & Mg-APP#3: Surface roughness parameters evaluated

Only the surface parameters which are physically relevant for affect the sustaining the of the water droplet were analysed;

- Sa, it is the most popular areal parameter and it was chosen because it represents the baseline for comparison with other research works;
- Spk, which refers to the mean height of peaks above the core surface and that can sustain the water droplet;
- Sku, which refers to the contact area which between the workpieces and the droplet;
- Ssk, which refers to the amount of peaks that can sustain the water droplet;
- Sal, is an indicator of the periodicity of a surface;

Surface defects examination

The same procedure used for titanium alloys was adopted for for magnesium alloys.

Chapter 7

Functional performance evaluation

In this Chapter, different techniques used for assess functional performances of different biomaterials are presented. Functional properties to be improved are wear resistance for titanium alloys and corrosion performaces for magnesium alloys and are specified in details in Chapter 3 on page 29.

7.1 Titanium alloys

In the following sections, the experimental methods used to evaluate functional properties of titanium alloys are described.

7.1.1 Wear tests

With the aim to evaluate the effect of process parameters on functional performances of titanium alloys, reciprocating sliding wear tests were carried out on a tribometer using a cylinder-on-plate configuration. The cylinders were made to slide against the plates parallel to their axis, in a linearly reciprocating path. The alloys used for the wear tests are representative of the materials pair currently used in hip joint replacements.
With the aim of reproducing as much as possible the human conditions, tests were performed wet and temperature controlled environment (37°C ±1°C). The temperature was constantly monitored through a thermometer immersed in the water basin.
The calculation of the force for each case study was made according to the Hertz's theory, which is briefly introduced in the following section.
The other wear parameters were changed on the basis on the case study analized.

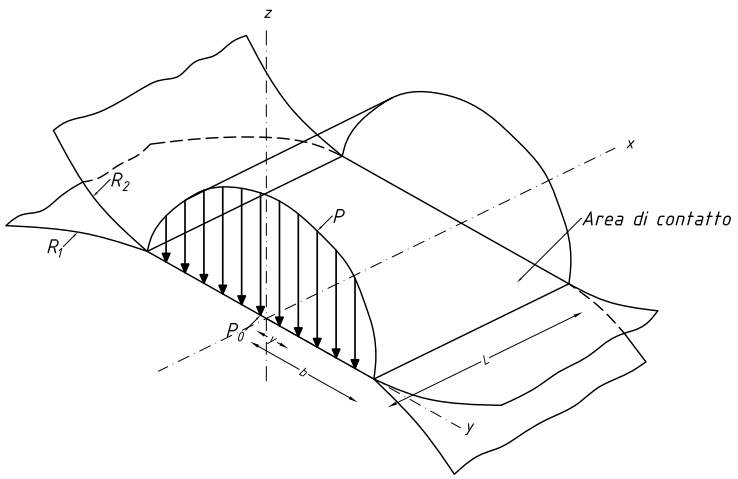

Figure 7.1: Example of Hertzian pressure on two mating cylinders.

Force determination

Theoretically, the contact area of two spheres is a point, and it is a line for two parallel cylinders. As a result, the pressure between two curved surfaces should be infinite for both of these two cases, which will cause immediate yielding of both surfaces.
However, a small contact area is being created through elastic deformation in reality, thereby limiting the stresses considerable.
These contact stresses are called Hertz contact stresses, which was first studies by Hertz in 1881 ([119]). The Hertz contact stress usually refers to the stress close to the area of contact between two spheres of different radii. Concerning the theory of elasticity it is based on some hypothesis:

- the radius of curvature of the solid are well defined in the point of contact;
- the bodies are perfectly elastic, homogeneous and isotropic;
- the forces are parallel to each other and orthogonal to the plane of contact;
- the frictional forces are neglected.

The firsts three assumptions imply that a very minor compare to R, dove a is the contact area radius and R is the effective radius of curvature of the two solids.

Cylinder on plane configuration

In this section, Hertzian's formulas for a cylinder on plane configuration, which is the one adopted in order to evaluate the effect of turning process

parameters on functional performances of Ti alloys, are reported.
The following equations refers to Fig. 7.1.

$$a = \sqrt{\frac{2 \cdot F \cdot (M_1 + M_2)}{B \cdot L \cdot \pi}} \tag{7.1}$$

In which F is the force, M_1 ed M_2 are material-dependent parameters, L is the contact area lenght whereas B is defined by the radius of the mating interfaces.

$$M_1 = \frac{1 - \upsilon_1^2}{E_1} \tag{7.2}$$

Where with υ_1 e υ_2 refers to Poisson' coefficient and elastic modulus E_1 ed E_2 of the mating interfaces, respectively.

$$M_2 = \frac{1 - \upsilon_2^2}{E_2} \tag{7.3}$$

$$B = \frac{1}{2} \cdot (\frac{1}{R_1} + \frac{1}{R_2}) \tag{7.4}$$

Where R_1 refers to the cylinder's radius while R_2 refers to the plane radius equal to infinity.

$$P_{MAX} = \frac{2 \cdot F}{\pi \cdot a \cdot L} \tag{7.5}$$

The pressure trend in the contact area is given by:

$$P(x) = P_{MAX} \cdot \sqrt{1 - \frac{x^2}{a^2}} \tag{7.6}$$

The maximum pressure is obtained in correspondence of x=0, according to [120].

Calculation of the force

The force applied on the wear tests was calculated on the basis of the following equation, obtained by substituting Eq. 7.1 in Eq. 7.5:

$$F = \frac{\pi \cdot L \cdot P_{MAX}^2 \cdot (M_1 + M_2)}{2 \cdot B} \tag{7.7}$$

For the calculation of the B parameter, it was necessary to define the length of the cylinder equal to 5 mm.
On the basis of the configuration chosen, a proper value of the force was calculated.

Table 7.1: Wear tests parameters.

Stroke (mm)	3
Load (MPa)	3 ± 0.1 N
Pressure (MPa)	50
Frequency (Hz)	1
Temperature (°C)	37 ± 1
Environment	Saline solution
Cycles	3600
Duration (hour)	1

Ti-APP#1: Wear tests

In this case study, sectioned acetabular cup (Fig. 7.2a) were made to slide against a CoCrMo cylinder to represent the metal-head acetabular cup connections.
The schematic test configuration and the experimental set-up for the wear tests is visible on Fig. 7.2b) and c), respectively.
Wear tests were conducted on a Rtec Instruments^{TM} tribometer featuring an integrated optical profiler.
A 3 mm long reciprocating sliding wear track, calculated on the basis of the maximum angle passed through by the hip during a gait cycle, in accordance to the ISO 1424-1:2002 standard, and a 50 MPa contact pressure suitable for acetabular cup-femoral head connections, were adopted.
On the basis of these parameters, the wear tests were carried out under a constant vertical load of 3 (± 0.1 N), at a frequency of 1 Hz. The tests lasted one hour corresponding to 3600 cycles, and were repeated five times for each cutting condition. Wear tests parameters are summarized on Table 7.1.

Ti-APP#2: Wear tests

In this case study, Ti6Al4V cylinder were made to slide against a ZrO_2 flat-plate in order to reproduce the dental prosthesis-abutment connection.
The zirconia ZrO_2 was chosen as counterpart material because it is commonly used for the fabrication of dental implant abutments [110]. Before tests, the zirconia plates were ground to obtain an initial surface roughness equal to 0.02 ± 0.09 μm.
Reciprocating sliding corrosion experiments were carried out coupling an electrochemical cell to the Rtech^{TM} Instruments tribometer equipped with an integrated optical profiler. The schematic representation of the overall experimental setup is reported in Fig. 7.3.

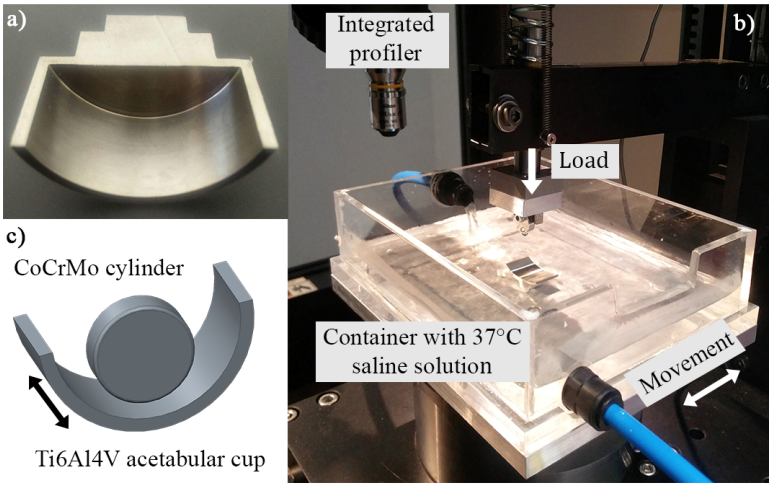

Figure 7.2: a) Ti6Al4V acetabular cup machined in a simplified geometry; b) experimental set-up for wear testing c) sketch of the wear testing configuration.

The contact interface was immersed in artificial saliva constantly maintained at a temperature of 37 ±1°C. The experiments were performed at a frequency of 1 Hz and lasted 3600 s. A normal force of 45 N was applied, which resulted in an initial contact pressure of 220 MPa on the basis of the results of a previous literature work [121].A stroke of 1 mm was imposed. Wear tests parameters are summarized on Table 7.2.

The sliding tests were carried out both at OCP and at an applied passive potential of 0.2 V. The experimental sequence adopted for the biotribological tests was the following:

1. Either system stabilisation at OCP for 5 min or application of the selected potential;

Table 7.2: Wear tests parameters.

Stroke (mm)	1
Load (MPa)	45 ± 1 N
Pressure (MPa)	220
Frequency (Hz)	1
Temperature (°C)	37 ± 1
Environment	Artificial saliva
Cycles	3600
Duration (hour)	1

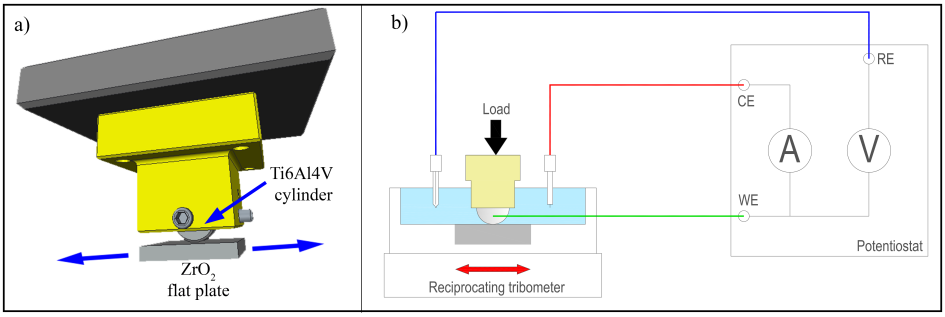

Figure 7.3: a) Cylinder on flat-plate configuration; b) Sketch of the experimental apparatus used for biotribological tests.

2. Sliding for 60 min while continuous measurement of either the OCP or the current;

3. Removal of the load while keeping constantly measured the OCP for 5 min or constantly applied the established potential.

7.1.2 Evaluation of the wear volume

In this section methods used to assess the wear volume are described, distinguishing on the base of the differents case-studies investigated.

Ti-APP#1: Wear volume calculation

Thanks to the optical profiler integrated in the tribometer, it was possible to measure the same zone before and after the wear test using a 10x magnification Nikon^{TM} confocal objective.
The positioning along the x and y directions (being the x-y plane the plane orthogonal to the optical axis of the profiler, i.e. the z axis) was ensured by the machine motorized axes, enabling better identification of corresponding surfaces and higher repeatability. The wear volume was evaluated in the middle of the wear track, which was the zone affected by the maximum pressure. To standardize the procedure, an area of 1.75 x 1.60 mm^2, centred on the mean line of the wear track (see Fig. 7.4c), was considered as reference. The area dimensions were identified on the basis of the most worn sample (evaluated on a preliminary experimental campaign). The evaluation procedure, shown schematically in Fig. 7.4, included the following main steps:

1. On-machine confocal acquisition of the surface topography, before and after wear testing (see Fig. 7.4a) and b).

2. Surface data processing. The removal of the measurements artefacts was achieved using a median filter and a threshold value for the iden-

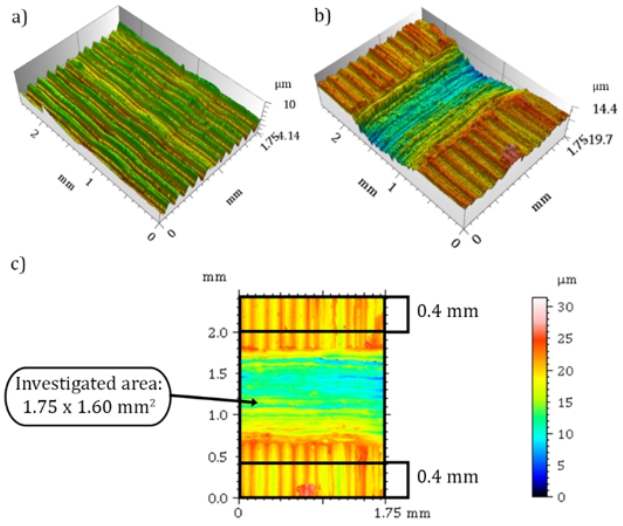

Figure 7.4: Procedure for the wear volume evaluation: a) unworn surface measured before wear testing; b) worn surface measured after wear testing; c) representation of the central area of interest and of the two lateral bands used for the evaluation procedure.

tification of outliers, based on the distribution of residuals. The corresponding pixels were classified as void pixels and ignored on further filtering operations. Filtering and removal of cylindrical form were obtained by polynomial fitting on the zones unaffected by the wear process, followed by interpolation of the void pixels.

3. Identification and fitting of corresponding zones of the same sample, before and after wear testing. The alignment of two corresponding topographies was based on two zones of 0.4 mm width, external to the area of interest mentioned above (see Fig. 7.4c). These steps were developed using the MountainsMap^{TM} software.

4. Computing of wear volume. The volume in between the unworn and worn surfaces was measured considering only the area of interest. The height difference between corresponding measured points and wear volume was calculated applying a trapezoidal method developed using Matlab^{TM} software.
   As previously described, the area for the wear volume calculation was maintained fixed for all the samples in order to reduce inaccuracies related to the wear track edge identification. Results are reported in terms of volumetric wear.

Ti-APP#2: Wear volume calculation

After the biotribological tests, the volumetric wear was evaluated using the Sensofar Plu Neox^{TM} profiler.
Three different profiles of the wear track were measured in the area characterized by the maximum pressure, which is located at the middle of the reciprocating sliding path at a distance of ± 1 mm from the centre. The average cross section worn area was then multiplied by the wear track length in order to assess the wear volume.

7.1.3 Coating synthesis and deposition

In this section, the procedure adopted for coating the Ti substrate are illustrated. Activities refers to the Ti-APP#3. The sphene precursor suspension and deposition techniques were carried out in collaboration with Prof. Lisa Biasetto (University of Padova).
A briefly description is given, but further details can be found elsewhere [122]. In summary, SILRES MK silicone resin (polymethylsiloxane, Wacker-Chemie GmbH, München, Germany) was used as SiO_2 precursor, in powder form, and was dissolved in isopropanol under magnetic stirring. CaO and TiO_2 precursors were added as active fillers, in the molar ratio corresponding to the composition of sphene ceramics ($CaO*TiO^2*SiO^2$) as a final product after ceramization. The ceramic yield of the MK polymer after heating in air at 1000°C was approximately 84 wt%. CaO, which was provided by $CaCO_3$ in the form of nano-sized particles (PlasmaChem, Berlin, Germany, 90 nm) and $TiO_2$2 (25 nm, Evonik Degussa GmbH, Germany), was added for a solid total content load of 48 vol%.
A commercially available automatic airbrush (Prona-RA-C2, Prona Tools, Toronto, Canada M3J 3A1) was used to coat the implants.
The main process parameters that were observed to influence the characteristics of the coatings were the inlet pressure, deposition time, rotation speed of the samples during coating, nozzle opening and its distance from the sample.
For these experiments, the chosen values are reported in Table 7.3. The conversion from suspension to sphene bioceramic coating was performed in air at 950°C for 3h (37 C/min heating speed).

7.1.4 Evaluation of the adhesion strength of a coating

Coating-substrate adhesion was evaluated by means of measurements of coating thikness and nano-hardness measurements.
The coating thickness was analysed using the FEG-SEM. The investigations were performed on the cross-section of the coated samples, which were embedded in resin and then polished with the same procedure described in section 6.2.1 on page 69.

Table 7.3: Main process parameters used to coat the dental implant prototypes.

Process parameter	Value
Inlet pressure (bar)	3
Deposition time (s)	1
Rotation speed (rpm)	9000
Nozzle diameter (mm)	1
Nozzle to sample distance (mm)	350

The coating thickness was measured through optical microscopy; at least ten measurements were taken in different zones of the samples and the averaged. The microstructure at the coating-substrate interface was analysed through optical microscopy after etching.
Nano-indentation measurements were carried out using the iMicro^{TM} from Nanomechanics Inc. nano-indenter to evaluate the hardness and elastic modulus of the zones that include the coating, the coating-substrate interface and a part of the substrate. Indentation maps were obtained using a high speed mechanical property mapping technique called NanoBlitz^{TM}, which enables mapping over large areas in a short amount of time and also accessing to large data sets for statistical analyses. The procedure included the sample positioning under the tip, approach to the surface, loading, unloading and retraction. From the load and depth data at each test location, the contact stiffness, hardness and modulus can be calculated using the standard Oliver and Pharr method. A diamond Berkovich tip was used for all the tests. Indentation maps consisted of a square of 300*300 μm^2 area on which 400 indentations were performed using a load of 70 mN on three different zones across the sections of each sample. Indentations were spaced sufficiently far apart so that the indentation behaviour was not affected by the presence of adjacent indentations, in accordance with the ISO standard 14577-4:2016. The obtained results were processed using the following procedure:

- the maximum values of both hardness and elastic modulus were extrapolated from the raw data of the nanoindenter;
- all the data were normalized with the respect to the maximum value found at point 1 for hardness and elastic modulus;
- the Matlab^{TM} software was used to create a contour map of hardness and elastic modulus that provided an easy and effective comparison between different samples.

Table 7.4: Chemical composition of the SBF solution in 1 L of distilled water.

NaCl	1.5881 g
NaHCO3	0.0709 g
Na2HPO4*7H2O	0.0492 g
MgCl26H2O	0.0617 g
KCl	0.0746 g
CaSO4*H2O	0.0171 g
CaCl2	0.0403 g

7.2 Magnesium alloys

In the following sections, the experimental method used to evaluate functional properties of magnesium alloys are described.

7.2.1 Potentiodynamic polarization tests

The potentiodynamic polarization tests, carried out on an Amel^{TM} 2549 potentiostat, made use of a standard three-electrodes cell, where the machined sample was the working electrode, immersed in SBF solution, which composition is described in Table 7.4, at 37°C ±1°C to reproduce the human body conditions.
The potentiodynamic polarization curves were obtained applying a potential from -2 V to -1.3 V at a scan rate of 0.5 mV^{-1}. The corrosion potential and corrosion current density were determined using the Tafel extrapolation method, according to the ASTM G5-14 standard.
Tests were repeated three times to assure repeatability.

7.2.2 Evolved hydrogen gas measurements

Evolved hydrogen gas measurements were performed in order to evaluate the corrosion rate of machined samples exposed to the SBF solution whose composition was previously described.
The hydrogen produced by the machined sample was collected by a funnel, located just above the sample, and then into a burette, placed over the funnel.
The amount of evolved hydrogen was determined by measuring the displacement of the solution level in the burette. All of the test equipment was placed in a climatic chamber that assured a constant temperature of 37°C ±1°C.
The tests, repeated four times for each machining conditions, lasted 3 weeks, after which SEM and profile surface analyses were performed to examine the

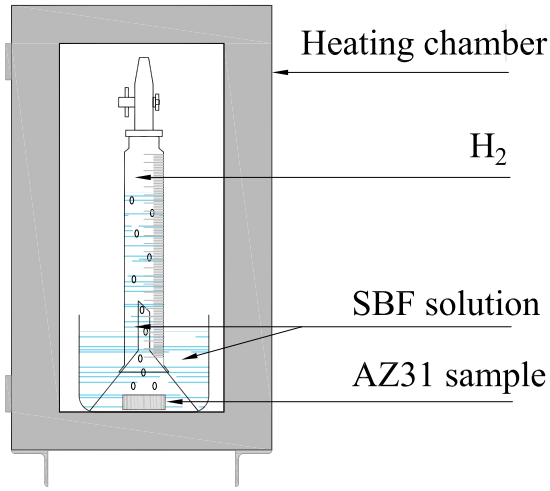

Figure 7.5: Sketch of the experimental apparatus built up to measure the volume of hydrogen involved.

morphology of the corroded surfaces.

A schematic representation of the experimental apparatus designed for the evolved hydrogen gas measurements is shown in Fig. 7.5 .

7.2.3 Contact angles measurements

The measure of the contact angle to evaluate the wettability of the machined samples was carried out applying a static sessile drop technique.

The used experimental apparatus (see Fig. 7.6) consisted of a horizontal stage used to place the sample, which allowed to be adjusted in the z-directions, a micrometer syringe to form a liquid drop, a halogen and intensity adjustable light source to illuminate the sample, and a Prosilica GT^{TM} camera for the images acquisition.

Before measuring, the samples were cleaned in an ultrasonic bath for 15 min to remove any residual. A liquid droplet of distilled water characterized by a volume of 10 μL was used.

In order to investigate the effect of machining process parameters on wettability, the liquid droplet was fall on the lateral surface of the cylindrical sample.

Tests was conducted at room temperature (25°C); each experiment was repeated eight times and the experimental results were taken as the mean value to assure reproducibility.

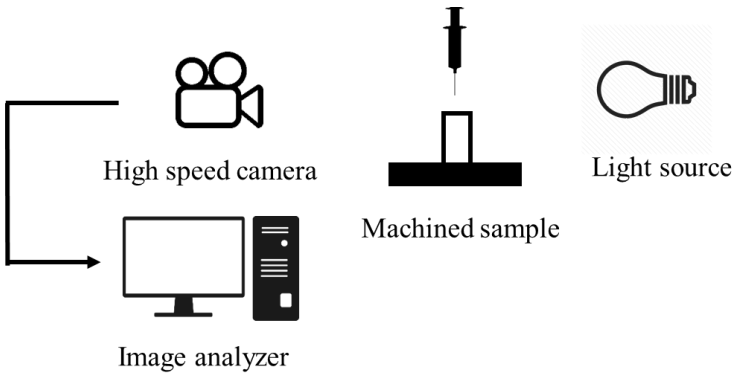

Figure 7.6: Sketch of the experimental apparatus used for contact angles measurements.

7.2.4 Citocompatibility

Cytocompatibility of the surfaces is an important factor for a biomedical devices, therefore it was decided to investigate evaluate if the cooling condition adversely affecting this parameter. It is worth to note that cells cannot adhere to a curved surface, as the one obtained through machining operation.
Therefore, it was decided to realize discs in which the flat face is realized by face turning operations. A special designed tool for carry out cryogenic face turning operation was designed as reported in 4.1.1. The effect of different cooling condition, namely dry and cryogenic, on citocompatibility were evaluated.
This study was performed in collaboration with prof. M. Conconi of the department of pharmaceutical and pharmacological Sciences at the University of Padova.

Cell cultures

MC3T3-E1 cells, a murine preosteoblastic cell line, were cultured with proliferation medium composed of alfa MEM without nucleosides (Invitrogen, Grand Island, NY, USA), 10% fetal bovine serum (FBS) (Sigma-Aldrich), 1% antibiotic antimycotic solution (AAS) (Sigma-Aldrich) and 1% glutamax (Invitrogen). The cell culture was maintained at 37°C in a humidified atmosphere with 5% CO2 and checked under the microscope daily. Trypsin-EDTA solution was used to detach cells from subconfluence cultures.
Cryo and dry samples were put into each well of a 24-well plate (Sarstedt, Nümbrecht, Germany) and irradiated with UVA light overnight. Thenafter, 300,000 cells were seeded in each well in proliferation medium. After 24 hours, medium was removed and replaced with osteogenic medium which contained alfa MEM without nucleosides (Invitrogen, Grand Island, NY, USA), 10% FBS (Sigma-Aldrich), 1% AAS (Sigma-Aldrich), 1% glutamax

(Invitrogen), 10 mM β-glycerophosphate (Sigma-Aldrich), 50 μg/ml ascorbic acid (Sigma-Aldrich) and 10 nM dexamethasone (Sigma-Aldrich). The medium was changed every day and the cultures were maintained for 1, 3 and 7 days.

Cell proliferation

Cell proliferation was determined using the CellTiter 96 ^{TM} AQueous One Solution Cell Proliferation Assay (Promega, Wisconsin, USA). Cells were cultured with osteogenic medium for 1, 3 and 7 days.
At each time point, the medium was removed. One mL of medium, composed of alfa MEM without nucleosides (Invitrogen), 5% fetal bovine serum 16000 (FBS 16000, Invitrogen) and 10% of the reagent MTS [3-(4,5-dimethylthiazol-2-yl)-5-(3-carboxymethoxyphenyl)-2-(4-sulphophenyl)-2H-tetrazolium], was added and the plate was incubated at 37°C for 4 h. After incubation, 100 μL of the medium were transferred into a 96-well plate and the absorbance was measured at 490 nm by using the EL 311 SX microplate autoreader (BioTek Instruments, Inc., Winooski, VT, USA).
The MTS tetrazolium compound (Owens reagent) is bioreduced by cells into a colored formazan product that is soluble in tissue culture medium. This reaction is achieved by NADPH or NADH produced by dehydrogenase of metabolically active cells. The amount of formazan is directly proportional to the number of living cells. Results were expressed as percent of control cultures grown on tissue culture-treated polystyrene plates.

Scanning electron microscopy

A 1 and 3 days, cultures were fixed with 4% glutaraldehyde in 0.1 M cacodylate buffer (pH 7.2) and dehydrated.
After critical point drying and gold sputtering, samples were examined by a scanning electron microscope (SEM; Stereoscan-205 S, Cambridge, UK).

Alkaline Phosphatase (ALP) and Bicinchoninic acid (BCA) Protein assay

MC3T3-E1 cultures were tested at 3 and 7 days. The Alkaline Phosphatase (ALP) activity in the cells and in the medium was measured by using the Alkaline Phosphatase Assay kit (Colorimetric) (abcam, Cambridge, UK). The samples were washed with PBS and trypsin was added to detach the cells. The cells were centrifuged at 1200 rpm for 5 minutes, and then were resuspended in 250 μL of assay buffer and lysed using a needle 21G x 1.5 (BD Biosciences, San Jose, CA, USA). Any insoluble material was removed by centrifugation at 12000 rpm at 4°C in a cold microcentrifuge. Eighty μL of the supernatant were placed into the well of a 96-well plate (Sarstedt) and 50 μL of 5mM p-nitrophenyl phosphate (pNPP) solution was added to

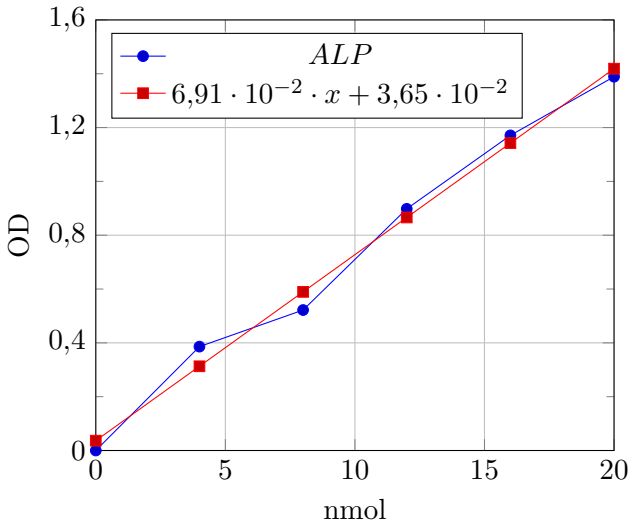

Figure 7.7: Standard curve for ALP assay.

each well.
PNPP is a phosphatase substrate which turns yellow when dephosphorylated by ALP. After mixing the samples, the plate was incubated at 25°C for 60 minutes and protected from light. The pNNP substrate is converted by the enzyme to an equal amount of coloured p-Nitrophenol (pNP).
After the incubation, 20 μL of stop solution was added to terminate the reaction, the plate was then gently shaked and optical density (OD) was measured at 405 nm using the EL 311 SX microplate autoreader. OD values were converted in nanomoles of ALP by using a standard curve previously obtained with known ALP quantities (from 4 to 20 nanomoles). The BCA Protein Assay Reagent Kit (Pierce Biotechnology, Waltham, MA, USA) was used to determine the protein content. This method combines the reduction of Cu^{+2} to Cu^{+1} by protein in an alkaline medium with colorimetric detection of Cu^{+1} using bicinchoninic acid. During the reaction, a purple coloured product is formed by chelation of two molecules of BCA with one cuprous ion. The working reagent (WR) was prepared by mixing 50 parts of BCA reagent A with 1 part of BCA reagent B. Two hundred μL WR were added to 25 μL of each sample (cell lysate) in a 96-well plate. The plate was placed on a shaker for 30 seconds, covered and then incubated at 37°C for 1 hour. After the plate was cooled to room temperature, the absorbance was measured at 570 nm on the EL 311 SX microplate autoreader. OD values were converted in microg/mL of protein by using a standard curve previously obtained with known bovine serum albumine quantities (from 5 to 125 μg/mL). For each sample, the ratio between ALP and protein content was calculated. For MSC cultures, results were expressed as percent of control cultures (no supplemented with peptides or BMP2) whereas for MC3T3-E1

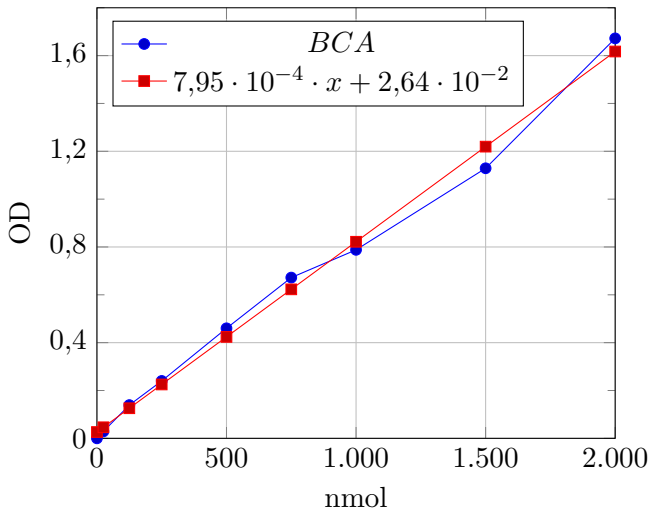

Figure 7.8: Standard curve for BCA assay.

cells as ng ALP/mg protein.

Statistical analysis

The results were expressed as a mean with the related standard deviation. The statistical analysis was performed by using Students t-test.

Part IV

Results and discussion

Chapter 8

Results and discussion for titanium alloys

In this Chapter, results and discussion of the different case studies involving titanium alloys are presented.
Details on the experimental campaign, materials and reasons that have pushed the study can be found in Section 5.1 on page 55.

8.1 Ti-APP#1: Results and discussion

In this section, the results and discussion relative of titanium alloys Ti-APP#1 are reported. Details about the experimental machining campaign are described on Section 5.1.1 on page 55.

8.1.1 Microstructural and mechanical characterization of the machined samples

Fig. 8.1 shows the microstructure of the cross section of the Ti6Al4V acetabular cups below the machined surfaces under the investigated conditions.
Sub-surface microstructural alterations are due to the thermo-mechanical loads exerted on the machined surface by the cutting process and they appear in form of elongated and deformed grains along the cutting speed direction [123].
In the case of Ti6Al4V semi-finishing turning, the temperature generated during the machining process was not sufficient to produce microstructural modifications since it did not exceed the β transus temperature. These finding are in accordance with many other results that can be found in literature concerning the machinability of Ti6Al4V [2].
Table 8.1 reports the extension of the machining-affected layers as a function of the cutting parameters. The depths of these deformed layers are comparable for the different cooling strategies, even though there is an increase in

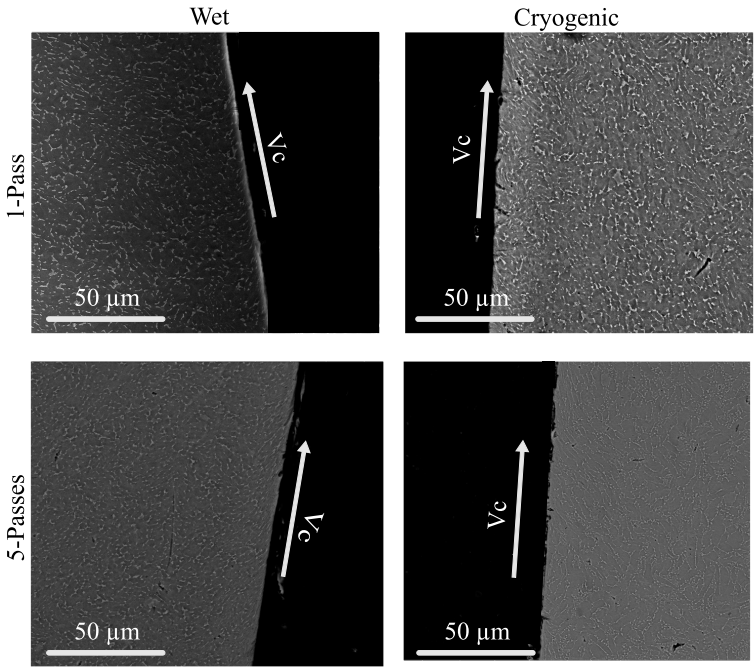

Figure 8.1: Effect of the investigated cutting parameters on the material microstructure below the machined surface.

the case of cryogenic cooling, as confirmed by Caudill et al. [124].
It is worth to notice that the mechanical properties of the EBM Ti6Al4V alloy are influenced by the thickness of the α phase lamellae, which are the result of consistent bending, stretching and grain refinement during the cutting process, and not by the extension of the machining affected layers [125].
Considering the number of passes, an increase of the deformed layer was found especially in the case of wet condition. This means that the material under the surface preserved the history of the previous passes.
The results of the micro-hardness characterization of the Ti6Al4V cups are reported in Fig. 8.2. It is worth to notice that the first point that can be evaluated with the micro-hardness measurements is set at a distance of 30 μm from the surface: this is why the measured records are not affected by the deformed layer evidenced by the micrographs, whose maximum extension is less than 30 μm (see Table 8.1).
In general, the use of liquid nitrogen induced a harder surface regardless the adopted number of passes. In fact, the hardened layer extended up to 150 μm below the machined surface. This can be ascribed by the fact that cryogenic machining contributed to reduce the cutting temperatures and promoted a hardness increment due to the combination of reduced thermal softening and greater grain refinement, as reported in several research

Table 8.1: Thickness of the machining-affected layer as a function of the adopted cutting parameters.

Cutting condition	Deformed layer (μm)
Wet-1 passes	6.6 $\pm$ 0.5
Wet-1 pass	21 $\pm$ 5.9
Cryo-1 pass	17.2 $\pm$ 2
Cryo-5 passes	29.4 $\pm$ 3

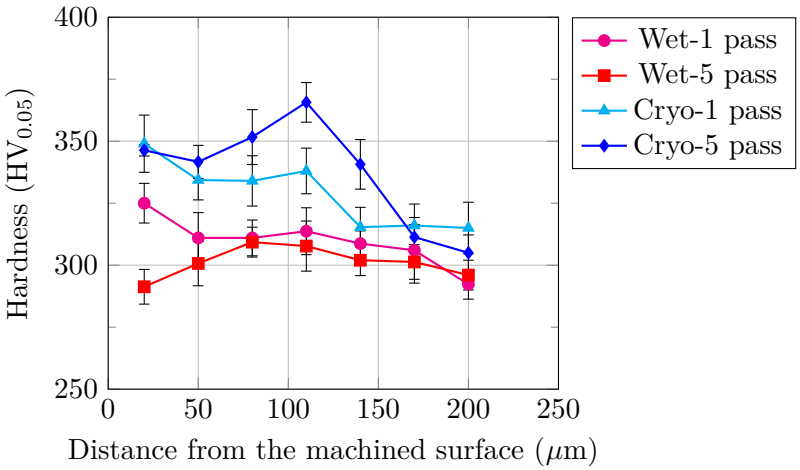

Figure 8.2: Effect of the investigated cutting parameters on the micro-hardness below the machined surface.

Table 8.2: Residual stresses as a function of the adopted cutting parameters. (σa and σt refers to the residual stress along the axial and tangential directions, respectively. σs and σd refers to the residual stress measured on the surface and at a depth of 25 μm, respectively.)

Cutting condition	σas (MPa)	σad (MPa)	σts (MPa)	σtd (MPa)
Wet-1 passes	-167	-140	-150	-121
Wet-1 pass	-50	35	-125	-102
Cryo-1 pass	-213	-195	-312	-250
Cryo-5 passes	-380	-278	-350	-286

studies. In [126], bars of Inconel 718 were turned under cryogenic cooling adopting cutting parameters values close to the ones investigated in this work: it was shown that higher values of the surface hardness were induced in case of cryogenic cooling compared to dry cutting.
In [56], the cryogenic cooling was applied in machining the wrought ZK60 magnesium alloy finding that the micro-hardness increased up to the 40% compared to the as-delivered alloy. In [11], deeper micro-hardness alterations were found in wrought Ti6Al4V samples that were cryogenically machined compared to the dry cut ones.
On the contrary, the number of passes had an effect only when cryogenic cooling was used. Actually, even if the same hardness value was reached in correspondence of 30 μm below the machined surface in the case of cryogenic cooling, layers beneath the surface were more hardened for the 5-passes machined cup. This outcome can be explained by the fact that when multiple passes were used to machine the cup, the material that was going to be cut was already hardened by the former pass compared to its as-delivered condition; however, such increment was not obtained in the case of wet cutting. In fact, the number of passes had a marginal influence on the micro-hardness values in the wet condition, as the curves are characterized by the same trend, see Fig. 8.2.

Table 8.2 reports the results of the XRD characterization. The parameter that mostly affected the residual stresses on the machined surfaces was again the cooling condition: a considerable improvement in the residual compressive stress state was obtained when the liquid nitrogen was applied.
Spraying liquid nitrogen when machining minimized the tensile stresses induced by the thermal effect and maximized the compressive stresses induced by the mechanical effect, resulting in a greater compressive residual stresses compared to the wet conditions.
Pusavec et al. [126] applied different cooling strategies in machining a nickel alloy and found that cryogenic machining showed a much larger compressive residual stresses beneath the surface on both the axial and tangential

directions compared to the other cutting conditions.
Besides this, they found a thicker compressive zone of material beneath the surface that extended to 70 μm below the surface in the case of cryogenic machining. Bicek et al. [127] came to the same conclusions, applying three lubricating conditions, namely dry, wet and cryogenic, when machining the AISI 52100 steel and quantifying the induced residual stress state.
Results showed that cryogenic machining generated the highest compressive residual stresses on the surface and beneath the surface among all the investigated conditions.
As regards the number of passes, in general a higher number of passes induced higher compressive residual stresses in case of cryogenically machined samples, whereas in case of wet machining a slight worsening was found for both the axial and tangential directions. Again, the number of passes had an influence only in the case of cryogenic turning for the aforementioned reasons.
Hardness and compressive residual stresses are two important design criteria in applications where a high wear performance is required. High surface and sub-surface hardness reduces wear, while larger compressive residual stresses improve the resistance to crack initiation, therefore both extending the service life of the finished products. On the contrary, conventional pre-machining and post-machining techniques (i.e. shot peening, laser peening, roller burnishing, etc.), generally used to improve both hardness and compressive residual stresses, require an additional step to be performed compared to cryogenic machining.
On the basis of the results of the microstructural and mechanical characterization of the machined sectioned cups, it can be stated that the cryogenic machining always improved the surface integrity, namely inducing a hardened and more compressed surface. The number of passes had an effect only when the cryogenic machining was adopted due to the fact that the underlying material was already significantly hardened and compressed by the previous passes.

8.1.2 Topography characterization of the machined samples

Fig. 8.3 shows partial profiles of the surfaces measured after machining to put evidence on differences in material distribution between the wet and cryogenic cooling conditions. Tables 8.3 and 8.4 reports the mean values of the surface texture parameters calculated on the basis of three different samples for each machining condition.

It can be seen that cryogenic cooling had a considerable effect in conditioning the obtained surface. The use of cryogenic cooling contributed to increase the surface roughness Sa, even though the increment was less than 25%.

The influence of cryogenic cooling on surface roughness has been widely

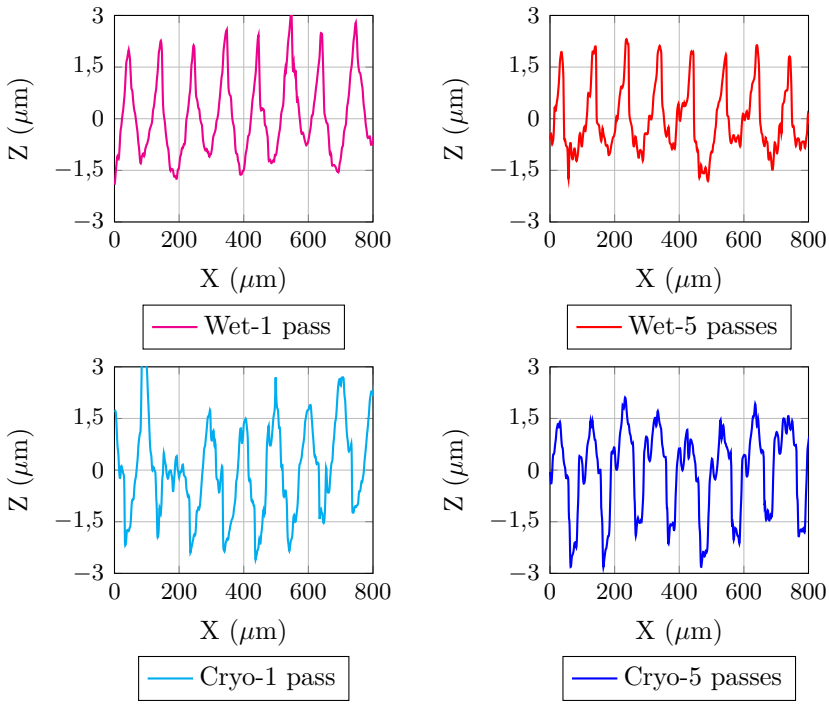

Figure 8.3: Machined surface profiles.

Table 8.3: Mean values and standard deviation of the height surface texture parameters.

Cutting condition	Sa (μm)	Ssk (μm)	Sku (μm)
Wet-1 passes	0.97 ± 0.03	0.43 ± 0.01	2.53 ± 0.02
Wet-1 pass	0.79 ± 0.02	0.72 ± 0.04	2.63 ± 0.03
Cryo-1 pass	1.13 ± 0.04	0.25 ± 0.02	2.56 ± 0.03
Cryo-5 passes	0.99 ± 0.05	-0.55 ± 0.01	2.29 ± 0.02

Table 8.4: Mean values and standard deviation of the functional surface texture parameters.

Cutting condition	Svk (μm)	Spk (μm)	Sk (μm)
Wet-1 passes	0.11 ± 0.01	1.23 ± 0.02	0.67 ± 0.02
Wet-1 pass	0.19 ± 0.08	1.27 ± 0.03	0.82 ± 0.03
Cryo-1 pass	0.41 ± 0.03	0.48 ± 0.03	1.32 ± 0.01
Cryo-5 passes	0.74 ± 0.01	0.22 ± 0.03	1.36 ± 0.02

studied, however a clearly trend has not been found. Dhananchezian et al. [128] applied liquid nitrogen when turning Ti6Al4V and a decrease of Sa between 25% and 35% compared to the wet condition was obtained, ascribable to the reduction of tool wear. On the contrary, in [129], a decrease of about 20% was achieved when dry cutting was used instead of cryogenic cooling.
Spraying liquid nitrogen onto the surface also contributed to generate rounder surface with broader valleys and shallower peaks. The skewness was the parameter most influenced by the cooling strategy: the Sku of the Cryo-1 pass surface was lower than the ones of both the wet surfaces, furthermore the skewness of the Cryo-5 passes surface decreased below zero, meaning that the cryogenic surfaces were characterized by larger peaks. The only parameter that was not affected by the cooling strategies was the kurtosis whose values did not show appreciable differences.
Grzesik et al. [130] studied the effects of cryogenic precooling of the workpiece in hard turning operations and found that surfaces with attractive service properties could be achieved; in particular, flattening surfaces with less dangerous feed marks were produced if compared to the dry cutting condition.
The effect of the number of passes is strictly linked to the adopted cooling strategy. The surface profiles obtained under wet conditions were similar regardless the number of finishing passes (see Wet-1 pass and Wet-5 passes in Fig. 8.3). On the contrary, the number of passes influenced the morphology of the profile by changing the distribution of the material in the case of cryogenic machining (see Cryo-1 pass and Cryo-5 passes in Fig. 8.3), where the material was more distributed on the roughness peaks. This contributed to shift the mean line towards higher values and, as a consequence, to increase the depth of the valleys.
These findings suggest that the cooling strategy has the major role in determining the surface topography, especially when several passes are adopted in order to machine the final shape.
A possible explanation is given by the fact that cryogenic machining is a severe plastic deformation process that significantly affects the material properties up to several tens of microns below the machined surface, as confirmed by the micro-hardness and XRD results (see Fig. 8.2and Table 8.2). In particular, 5-passes cutting operations are carried out with a material characterized by an already improved surface integrity and consequently with an already enhanced mechanical behaviour. Furthermore, cryogenic machining is a temperature-dependent process: even if the cutting operations were carried when the tool holder temperature achieved a stationary regime (as previously studied in [131]), the change from one to five passes led to an increase in the process time and allowed the Ti6Al4V bar reaching a lower temperature if compared to its conditions when machined in a single pass. These phenomena can be considered responsible to the completely different

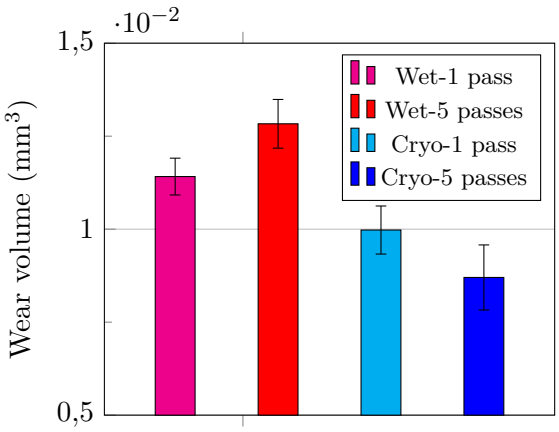

Figure 8.4: Effect of the investigated cutting parameters on the wear volume.

topography obtained varying the number of passes. As the number of passes increased, the material was hardened both by the previous passes and the low temperature induced by the influx of liquid nitrogen, and thus affected the material response to the cutting operation, resulting in enhanced surface characteristics.

8.1.3 Wear analysis

The effects of the investigated cutting parameters on the wear volume are displayed in Fig. 8.4. The cooling strategy has a crucial effect on the wear behaviour: cryogenic machined samples presented the lowest wear rate regardless of the number of finishing passes. These findings are in accordance with the results of the mechanical characterization: in fact, when liquid nitrogen is applied, the machined surface is characterized by an improved superficial condition, namely by an increased hardness and more compressed state of stress. Moreover, the results are in accordance with the Archard's wear rate law [132] that states that the wear volume is inversely proportional to the hardness of the softest contacting surface, whereas in [133] was demonstrated that large compressive residual stresses were prone to delay the crack initiation phenomena.
Considering the number of passes, cryogenic cooling had a positive effect on the wear behaviour: the Cryo- 5 passes sample presented the best surface integrity after the turning operation and was characterized as well by the lowest wear volume after the tribological test.
On the contrary, an inverse trend was detected in the case of wet conditions: even though no major differences were found after the mechanical characterization, a negative effect of the number of passes was shown, as the Wet-5 passes sample presented a higher wear volume than the Wet-1 pass samples. Although the surface conditions were very closer between one and

five passes, there was a slight worsening in terms of hardness 30 μm below the machined surface and a more tensile residual stress status for the Wet-5 passes sample, which could explain the highest wear volume.
The correlation between the wear volume and the areal surface parameters is presented in Fig. 8.5.
Fig. 8.5 shows a weak correlation between the Sa parameter and the wear volume: surfaces that were initially rougher did not necessarily wear more, as evidenced by the rougher surface of the Cryo-1 pass sample that did not provide the highest wear volume. This implies that the Sa parameter, even if it is very often associated to the wear performances, cannot be considered a comprehensive surface texture parameter to predict the wear behaviour.
On the contrary, Sk, Svk and Spk are more suitable indicators of the wear performances as an overall trend with the wear volume was identified. In fact, higher values of the mentioned parameters corresponded to higher wear volumes. The only exception was the Wet-1 pass sample that was characterized by a lower wear volume compared to the Wet-5 passes sample even if its Sk, Svk and Spk values were lower.
However, it is worth to note that the differences in the corresponding surface parameters were very restrained for Svk and Spk (at most of 0.8 μm), therefore, taking into account the experimental variability, the highlighted trend can be considered confirmed.
In general, surfaces with deep valleys are considered the most suitable for lubricating sliding applications since the valleys can work as a fluid reservoir, while surfaces with high peaks that protrude from the core are generally detrimental to wear resistance as the peak region usually wears out during the sliding process.
Moreover, higher Svk is associated to the presence of deeper valleys that can increase the probability of entrapment of the wear debris generated during the sliding process, thus avoiding their involvement on the third wear process that usually takes places on the top of the asperities. This explains why surfaces with deeper valleys and lower peaks should be preferred in the case of bearing applications.
The Ssk parameter shows the best correlation with the wear volume, indicating that lower skewness values are beneficial towards the wear phenomenon. In particular, the Cryo-5 passes surface, which had a negative skewness value, was characterized by the lowest wear volume compared to the other conditions that had positive skewness values. A positive skewness value implies relatively high surface peaks that can be easily removed during sliding, resulting in a detrimental wear behaviour. Indeed, the worst wear performance was given by the Wet-5 passes sample characterized by the highest skewness.
Therefore, it can be stated that a good bearing surface should be characterized by a negative Ssk value thanks of the presence of relatively few peaks that can quickly wear out and relatively deep valleys to retain the body fluid

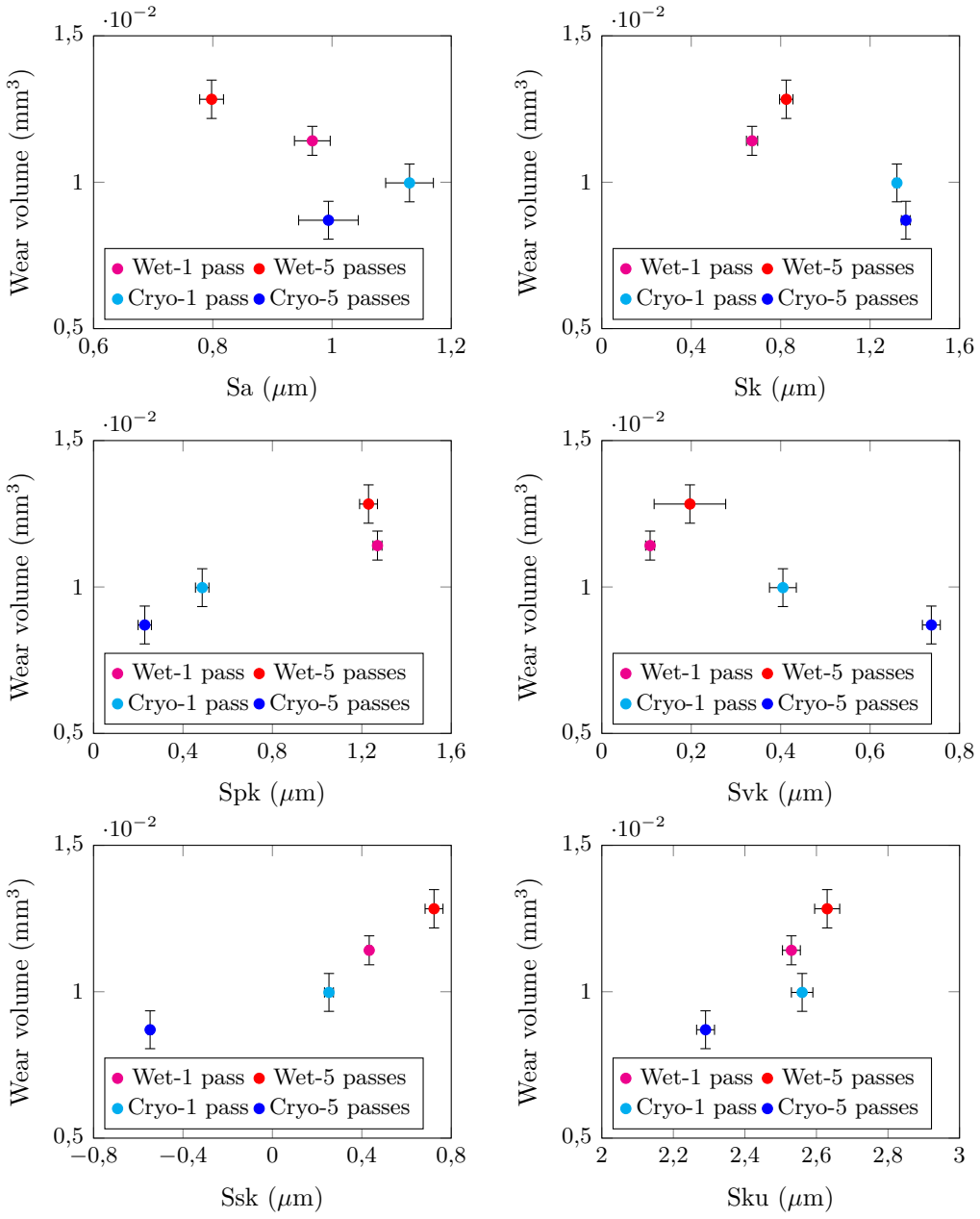

Figure 8.5: Effect of the investigated cutting parameters on the wear volume.

solution traces that can influence the tribological performances.
On the contrary, Sku could not be correlated to the wear behaviour because, although most of the samples were characterized by the same skewness values, they resulted in completely different amount of wear. Therefore, Sku cannot be considered a suitable indicator of wear performances in the case of biomedical applications.

8.1.4 Conclusions

The present work aimed at providing a correlation between machining parameters and wear behaviour making use of in-vitro testing. MoM hip joint replacements were the reference case study, where the wear behaviour of Ti6Al4V acetabular cups, machined under different cooling conditions and number of machining passes, was studied.
The following considerations may be drawn:

- A lower wear volume was detected for the cryogenically machined samples, regardless the number of passes, compared to the one of wet machined samples. The improvement is ascribed to the strengthening of the surface and sub-surface mechanical properties, namely enhanced hardening and compressive residual stresses, and to the generation of a texture completely different in terms of surface parameters, characterized by lower skewness and height of peaks, higher depth of valley and of the core roughness;

- The lowest wear volume was detected for the sample machined using five passes and adopting liquid nitrogen as cooling medium. Indeed, cryogenic machining significantly affects the material properties below the turned surface, and the strategy of use multiple passes emphasizes the effect obtained with a single pass. On this basis, the use of cryogenic cooling and the adoption of multiple passes for achieving the final shape of Ti6Al4V acetabular cups represent an optimized strategy to obtain improved wear properties.

8.2 Ti-APP#2: Results and discussion

In this section, the results and discussion relative of titanium alloys Ti-APP#2 are reported. Details about the experimental machining campaign are described on Section 5.1.2 on page 58.

8.2.1 Surface characterization after machining

The results of the surface integrity characterization for the EBM and wrought Ti6Al4V cylinders are presented in Table 8.5.
As expected, the material as-delivered conditions have a slight influence on

Table 8.5: Surface characteristics of the wrought and EBM Ti6Al4V cylinders after semi-finishing turning.

As-delivered state	Cutting condition	R_a (μm)	R_z (μm)
Wrought	Dry	0.365 ± 0.005	2.044 ± 0.11
EBM	Dry	0.354 ± 0.009	1.931 ± 0.18
Wrought	Wet	0.358 ± 0.008	1.934 ± 0.007
EBM	Wet	0.351 ± 0.009	2.212 ± 0.22
Wrough	Cryogenic	0.341 ± 0.0035	1.693 ± 0.27
EBM	Cryogenic	0.326 ± 0.0019	1.76 ± 0.11

Table 8.6: Mechanical characteristics of the wrought and EBM Ti6Al4V cylinders after semi-finishing turning.
(σa and σat refers to the residual stress along the axial and tangential directions, respectively.)

As-delivered state	Cutting condition	$HV_{0.05}$	σa (MPa)	σt (MPa)
Wrought	Dry	364 ± 6	-50	-208
EBM	Dry	370 ± 4	-28	-205
Wrought	Wet	371 ± 5	-55	-150
EBM	Wet	380 ± 3	-71	-160
Wrough	Cryogenic	391 ± 8	-67	-108
EBM	Cryogenic	400 ± 5	-87	-148

the surface roughness.
On the contrary, the cooling strategy has an important effect, considerably affecting the surface finish. The use of LN2 as coolant leads to smoother surfaces, dry machining to rougher surfaces whereas the wet condition sets in the middle.
The same trend can be found in the work of Dhananchezian et al. [128] where the influence of the cooling conditions on the surface integrity of the wrought Ti6Al4V was studied: they attributed the surface roughness reduction to the decreased cutting temperature that led to less adhesion forces between the newly generated workpiece and the tool surface resulting in lower tool wear.
On the contrary, the roughest surface was obtained with dry cutting as a consequence of the high temperature reached on the workpiece and the high friction at the workpiece-tool interface [134].
In general, the use of different cooling strategies causes a variation of the

micro-hardness regardless of the Ti6Al4V as-delivered conditions, with values higher for the EBM Ti6Al4V compared to the wrought one.
The highest hardness was recorded in all the cryogenic machined samples, with an increase up to 8% compared to the dry condition. The wet machined samples performed better than the dry machined ones, but had a lower hardness compared to the cryogenic machined samples. The use of the cutting fluid reduced indeed the temperature, although the cooling effect was not comparable with that assured by the use of the LN2.
The measurements of the residual stresses pointed out that the use of the cryogenic cooling induced higher compressive residual stresses at the surface along the axial direction, while, on the contrary, dry machining generated higher compressive residual stresses along the tangential direction. Again, the wet condition sets in the middle.
Outeiro et al. [16] studied the influence of cryogenic machining on the surface and subsurface residual stresses distribution finding that this cooling strategy could induce a slightly deeper compressive residual stress profile when compared to dry cutting especially near the surface where the material was more significantly affected by the heating generated during machining. Pusavec et al. [126] studied the surface integrity of the Inconel 718 as function of the cooling conditions, namely dry, minimum quantity lubrication and cryogenic cooling. They found that in case of cryogenic cooling not only the stresses beneath the surface decreased up to 60%, but also the affected zone was thicker.
Therefore, it can be concluded that cryogenic machining can lead to a substantial improvement in the surface finish parameters leading to a harder, smoother and more compressed surface.

8.2.2 Corrosion curves

The potentiodynamic polarization curves obtained in artificial saliva at 37°C are reported in Fig. 8.6. Table 8.7 shows the electrochemical parameters extracted from the potentiodynamic curves of the wrought and EBM Ti6Al4V as function of the different cooling conditions.
By comparing the polarization curves, it can be noted that, regardless of the Ti6Al4V as-delivered conditions, all the cryogenic machined samples presented curves that were shifted towards higher potentials, with an ennoblement of about 0.2 V in case of the EBM Ti6Al4V, and an ennoblement of about 0.1 V for the wrought Ti6Al4V.
The corrosion potential is a thermodynamic characteristic related to the material tendency of being corroded and is a measure of the nobility of the sample: the cryogenic machined samples characterized by higher Ecorr were less likely attacked by the corrosion environment than the dry machined samples characterized by lower Ecorr.
Considering instead the EBM alloy, a much more significant decrease in

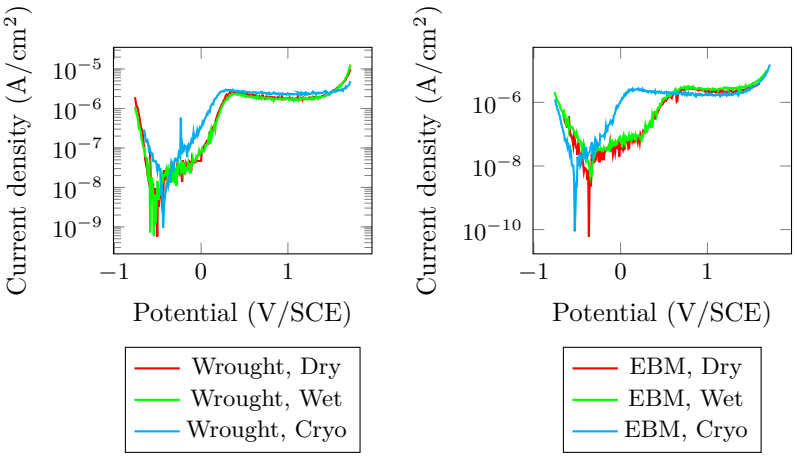

Figure 8.6: Potentiodynamic polarization curves in artificial saliva at 37°C: (a) wrought Ti6Al4V, and (b) EBM Ti6Al4V.

the corrosion current density, and so an increase in the corrosion resistance, can be observed. In terms of corrosion current density, there was a slight decrease for the cryogenic machined samples compared to the dry and wet ones in case of the wrought alloy.

As claimed in the G102-89 standard, the Icorr is linked through a directly proportional relationship to the corrosion rate; this means that an increase in Icorr corresponds to an increase in the mass lost by the Ti6Al4V implant during its service-life in the human body. This indicates that the corrosion properties are strongly influenced by the cooling conditions, proving that cryogenic machining can be an efficient method for enhancing the material corrosion properties.

In addition the material as-delivered state significantly influences the corrosion resistance: in fact, the EBM alloy is characterized by improved corrosion properties than the wrought one, thus being for the EBM alloy the cooling effect more significant. A nobler potential together with lower corrosion current density implies that the material is characterized by a better corrosion behaviour, which is a highly demanded characteristic in the case of aggressive environment like the human mouth. Thus can be ascribed to the obtained surface conditions, and, in particular, to the high compressive stress state recorded along the axial direction on the surface of the cryogenic machined samples.

The strong correlation between the compressive residual stresses and the improved corrosion performances can be found in different literature works. Takakuwa et al. [135] studied the effect of the residual stresses generated by different surface finishes on the corrosion behaviour of the austenitic stainless steel 316L finding a strong correlation between the two factors. In

Table 8.7: Corrosion potentials and corrosion current densities recorded in artificial saliva at 37°C .

As-delivered state	Cutting condition	E_{corr} (V/SCE)	I_{corr} ($\mu A/cm^2$)
Wrought	Dry	-0.5	8E-8
EBM	Dry	-0.55	3E-8
Wrought	Wet	-0.5	9E-8
EBM	Wet	-0.5	3E-8
Wrough	Cryogenic	-0.4	2E-8
EBM	Cryogenic	-0.35	1E-8

particular, they found a rapid decrease up to 70% in the current density at increasing the compressive residual stresses. They ascribed this enhanced behaviour to the formation and retention of a passive film that required lower current density when a compressive stress was introduced in the material. These results are confirmed by the studies carried out by Y. Wang [136] who reported that the surface integrity had a significant effect on the corrosion resistance of an aluminium alloy, finding a decrease in corrosion pits when a compressive residual stress state was induced in the material.
Therefore, it can be concluded that cryogenic cooling can be used as a strategy to strengthen the Ti6Al4V corrosion resistance in human mouth corrosive media.

8.2.3 Biotribological results

The evolution of the OCP with time of the titanium alloys was monitored before, during and after the sliding tests. The obtained results are reported in Fig. 8.7.

Before the beginning of the sliding, the measured OCP indicates the presence of a passive film on the alloy surface in contact with the saliva solution. An anodic shift was observed suggesting a thickening of the passive layer. An abrupt decrease of the potential was observed after the starting of the test, indicating a depassivation of the surface induced by the scratching of the passive film caused by sliding and, therefore, indicative of the exposure of fresh active titanium to the environment.
The OCP reached a minimum value immediately after the beginning of the test and then it tended to increase towards less active values as a consequence of the equilibrium reached between the mechanical depassivation and the electrochemical repassivation. The small oscillations of the OCP during sliding are indicative of this phenomenon of scratching and subsequent reformation of the passive layer. At the end of the sliding, the OCP recovered

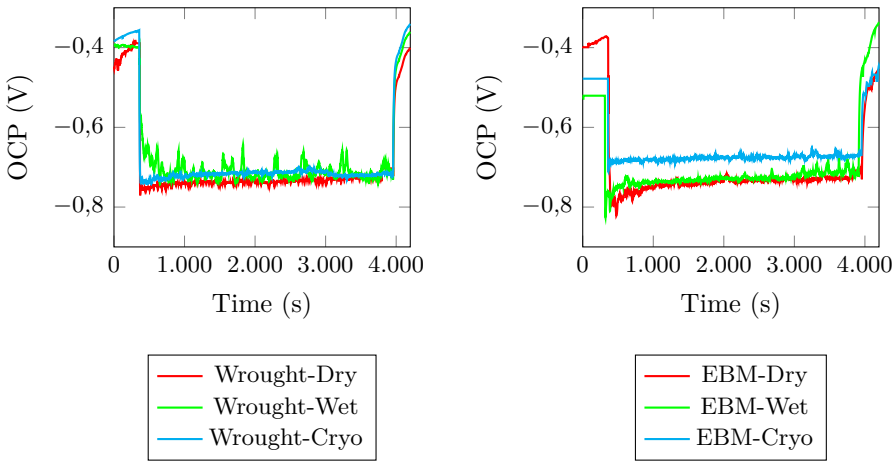

Figure 8.7: OCP evolution with time during the biotribological tests in artificial saliva at 37°C: a) wrought Ti6Al4V, and b) EBM Ti6Al4V.

towards more positive values indicating the reformation of the passive layer on the material. The values of the average potential recorded during the reciprocating sliding tests are reported in Table 8.7.

The average potential values that characterized the wrought Ti6Al4V were slightly higher than those of the EBM alloy. This outcome seems to be in disagreement with the results of the surface characterization after machining; however, similar evidences are present in literature, like the work by Licausi et al. [137] who studied the corrosion and tribocorrosion behaviour of the Ti6Al4V obtained by casting and powder metallurgy, and found that the cast alloy tribocorrosion curves set at higher potential values compared to the ones of the sintered alloy. They ascribed such behaviour to the presence of pores that increased the sintered alloy surface exposed to the test solution.

Concerning the different cooling conditions, the dry machined samples were characterized by the lowest potential values while the cryogenic machined curves were generally arranged to higher potential values. This means that, during naturally scratches of dental implant in oral mouth as tested in this study, the cryogenic machined samples are less prone to be corroded. Again, the samples machined using the cutting fluid had an intermediate behaviour between the dry and the cryogenic machined ones.

The potential sensitivity to the cooling conditions is in agreement with the results of the machined surface characterization, proving that the higher the hardness and compressive residual stresses the more improved the corrosion resistance. To this regard, the EBM sample that was cryogenically machined showed the best performance in terms of corrosion resistance.

Therefore, the OCP monitoring during the biotribological tests substan-

Table 8.8: Potential (E_{AVG}) and corrosion current ($I_{sliding}$) recorded during the biotribological tests.

As-delivered state	Cutting condition	E_{AVG} (mV)	$I_{sliding}$ (μA)
Wrought	Dry	-71 ± 9	107 ± 26
EBM	Dry	-73 ± 5	135 ± 24
Wrought	Wet	-69 ± 5	122 ± 24
EBM	Wet	-72 ± 2	107 ± 24
Wrough	Cryogenic	-69 ± 5	105 ± 26
EBM	Cryogenic	-67 ± 9	75 ± 80

tially confirmed the results recorded during the potentiodynamic polarization: the cryogenic machined samples had the best corrosions performances, even more evident in case of the EBM Ti6Al4V. Fig. 8.8 shows the current density evolution with time when a constant potential of 0.2 V was applied during the biotribological tests.
Before the sliding starting, the whole surface was passive and the anodic current was very low. When the sliding started, a sudden increase of the current occurred due to the mechanical removal of the oxide layer and the anodic dissolution of the surface active sites. At the end of the test, the current droptextsubscript since the mechanical removal effect was suppressed allowing the reformation of the oxide layer at the worn area.
Table 8.8 summarizes the average values of the current density assumed by the samples during the biotribological tests carried out at an applied passive potential. The current passing during sliding was calculated by subtracting the value of the current measured before starting the test from the current measured during sliding. Again, the most influencing parameters were the cooling conditions, showing that the dry machined samples were characterized by the highest current density while the cryogenic machined ones were characterized by the lowest value.
The considerations proposed for explaining the OPC test can be similarly applied in this case and this data confirm the previously reported ones.

According to Bazzoni et al [138], in a tribocorrosion system several mechanisms simultaneously take place resulting in material volume loss: wear accelerated corrosion (leading to a volume loss referred to as (V_{chem}) and mechanical removal of the particles (V_{mech}) in the wear track as well as corrosion (V_{corr}) outside the wear track. Therefore, the overall volume loss can be expressed according to Eq. 8.1:

$$V_{tot} = V_{mech} + V_{chem} + V_{corr} \tag{8.1}$$

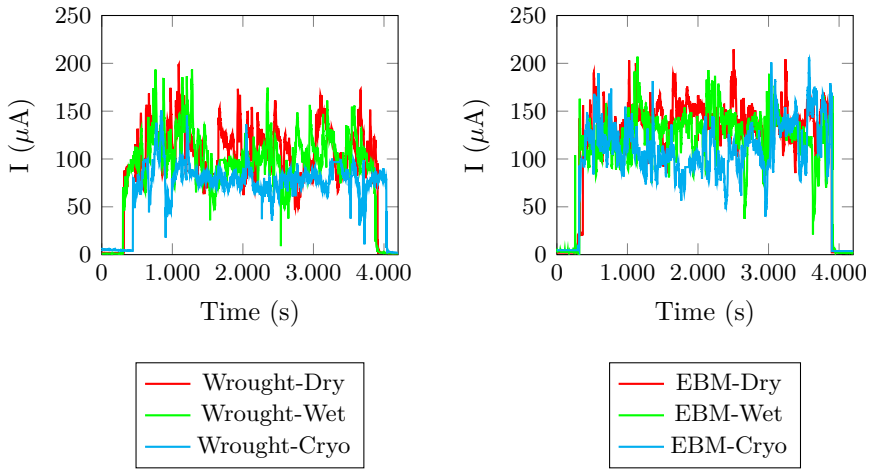

Figure 8.8: Current evolution with time at an applied potential of 0.2 V in artificial saliva at 37°C: a) wrought Ti6Al4V, and b) EBM Ti6Al4V.

Titanium alloys are prone to passivation and show very low passive dissolution rate; therefore, their volume loss caused by the corrosion outside the wear track can be neglected, and the overall material loss can be simplified as follows:

$$V_{tot} = V_{mech} + V_{chem} \tag{8.2}$$

The material removed by anodic oxidation in the wear track Vchem was calculated from the measured current values using the Faradays law (3):

$$V_{chem} = \frac{I_{sliding}}{t * M * n * F * \rho} \tag{8.3}$$

where M is the atomic mass of the alloy (46.64), n the charge number for the oxidation reaction (assumed equal to 4), F the Faradays constant (96487 C/mol), ρ the density of the alloy (4.43 g/cm^3), and t the duration of the sliding equal to 3600 s. The total wear volume was determined on the basis of the procedure described in Section 7.1.2.
Fig. 8.9 a) shows the image of the worn surface of the wrought sample machined in dry condition acquired through the profiler, while Fig. 8.9 b) shows the matching graph of the wear scar in the area highlighted by the arrows.
The obtained results are listed in Tables 8.9 and 8.10 , being the amount of V_{mech} the result of the difference between V_{tot} and V_{mech}. In case of OPC just the total wear volume is reported, as the wear-accelerated corrosion was not taken into account being its contribution negligible.
In general, as expected, the total wear volume from the tests carried out at an applied potential is higher than the one obtained during OCP tests, as a consequence of the enhancement of the corrosion induced by the sliding

Table 8.9: Average volume loss expressed in 10^{-3} mm^3 during the biotribological tests at OCP.

As-delivered state	Cutting condition	V_{tot}
Wrought	Dry	62 ± 6
EBM	Dry	70 ± 3
Wrought	Wet	39 ± 8
EBM	Wet	42 ± 7
Wrough	Cryogenic	40 ± 10
EBM	Cryogenic	37 ± 6

Table 8.10: Average volume loss expressed in 10^{-3} mm^3 during the biotribological tests at a potential fixed to E=0.2 (V).

As-delivered state	Cutting condition	V_{tot}	V_{wrac}	V_{mech}
Wrought	Dry	86 ± 5	10.51 ± 1	75.5 ± 7
EBM	Dry	88 ± 4	13.2 ± 1	74.8 ± 4
Wrought	Wet	42 ± 6	11.9 ± 1	30.1 ± 6
EBM	Wet	45 ± 6	10.5 ± 1	34.5 ± 6
Wrough	Cryogenic	43 ± 7	10.3 ± 1	32.7 ± 3
EBM	Cryogenic	44 ± 7	7.37 ± 1	36.6 ± 6

process. Another general consideration is that, since the Ti6Al4V alloy is a passive metal, mechanical wear mainly contributes to the tribocorrosion degradation whereas the wear accelerated corrosion is a small percentage of the total wear Both at OPC and at a passive potential, the total wear volume of the wrought and EBM samples are similar. Similar results were found by Licausi et al [137], who studied the influence of the fabrication process as a function of the fluoride content in artificial saliva. They demonstrated that V_{mech} at an applied passive potential of 0.2 V in case of the sintered titanium was slightly higher than in case of casting attributing this evidence to the higher amount of asperities obtained during the powder metallurgy processing route.
A more significant effect can be found considering the cooling strategy: the sample machined in dry conditions presented nearly the double amount of wear volume compared to the wet and cryogenic machined samples. Both at OPC and at a passive potential, the dry machined EBM samples were characterized by the highest amount of wear while the cryogenic machined EBM samples by the lowest one. These outcomes are in accordance with the fact that the dry machined EBM sample presented the lowest potential value and the highest corrosion current value during sliding. This sample presented also the highest amount of wear accelerated by corrosion due to the fact that its corrosion potential was the lowest between the considered cases. On the contrary, the cryogenic machined samples had a sensible lower wear volume compared to the dry machined samples due to their improved surface properties. This is in accordance with the work by S. Bruschi et al. [139] who showed that cryogenic machining could be an efficient method to reduce friction and to assure the occurrence of a higher degree of adhesive wear rather than abrasive wear on the machined cylinders, therefore limiting the scratching of the underlying material and reducing the material loss. The wet machined samples are also characterized by a smaller volume of total wear compared to the dry machined ones. These is in accordance with the results of the characterization after machining that showed the improved surface integrity obtained by using a cutting fluid during machining compared to dry cutting.
The wear volume of the wet machined samples was found to be close to the one of the cryogenic machined ones, revealing a good wear behaviour. Anyway, the wet machined samples were characterized by a higher degree of wear accelerated corrosion that could increase in most aggressive environments, as in the presence of the toothpaste fluorides.

8.2.4 Wear characterization

The SEM images of the wear scars after the biotribological tests under OCP are shown in Fig. 8.10. The wear scars of the samples worn at E=0.2 V are not included because they show similar characteristics to those collected at

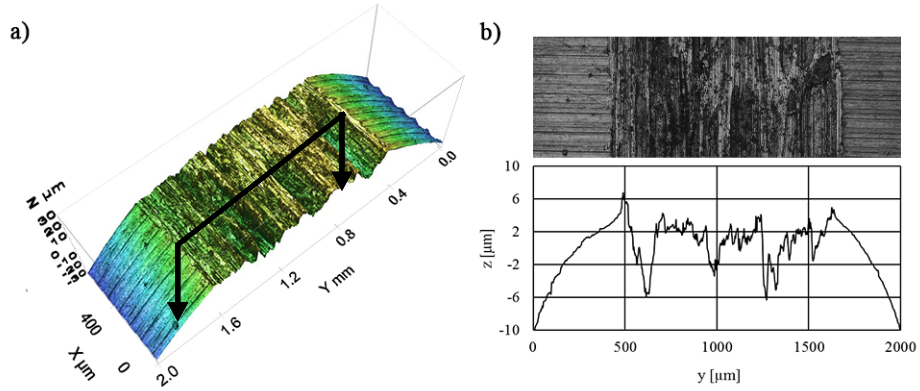

Figure 8.9: A) Profiler image of the worn area of the wrought sample machined in dry conditions; B) Section profile in correspondence of the area highlighted in A).

OCP. Figures compare the Secondary Electron and Backscattered detectors images recorded for each sample. The SE images are representative of the topography of the worn surfaces, while the BSED images add information about the surface chemical composition, namely chemical elements with different atomic number appear with different grey scale colours. In general, different wear mechanisms can be detected, namely abrasive and adhesive wear, regardless of the processing route and cooling strategies. All of the images show uniform grooves aligned with the sliding direction and perpendicular to the machining feed marks that are representative of abrasive wear, but also some adhesive wear is present, revealed by the presence of patch of material of a different nature from the substrate. By comparing the wear scars, it can be noticed that the amount of adhered material is higher for the wrought samples except in the case of the cryogenic machined one. These observations are in accordance with the amount of calculated wear volume: the EBM samples were in fact characterized by a higher amount of volume loss except in the cryogenic case. This can be ascribed to the fact that the presence of material from the counterpart can protect the underlying Ti6Al4V surface from further wear, reducing abrasion. Fig. 8.11A, in which a magnification of the wear scar of Fig. 8.10IIa is reported, confirms that: consistent adhered patches cover evenly the surface of the sample. It is worth to notice that these layers present micro-cracks perpendicular to the sliding direction as a consequence of the severe deformation they were subjected to. Considering the influence of the cooling strategy, the dry machined samples presented wider and more fragmented wear scars, and were characterized by the presence of craters that develotextsubscript as a consequence of the abrasion exerted by flakes of material removed from the surface. An example of these craters is shown in Fig. 8.11B, where a certain amount of wear debris can be also noticed, which could have enhanced the

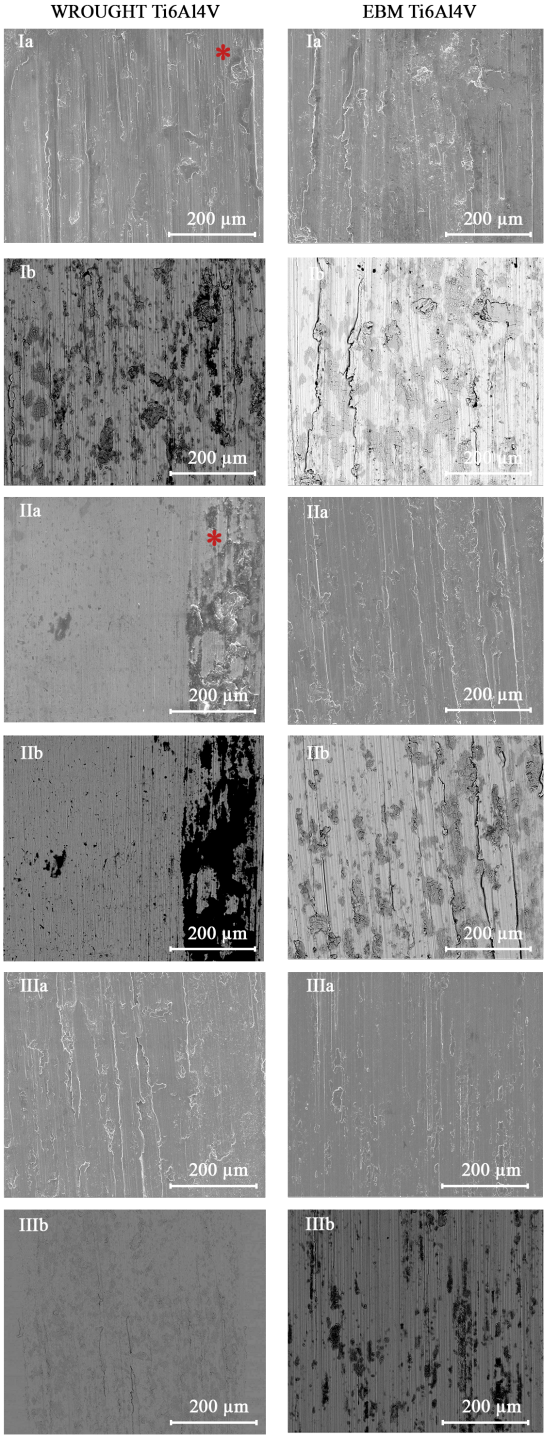

Figure 8.10: SEM images of the wear scars at OCP. Key: a) SE images, b) BSED images, I) samples machined in dry conditions, II) samples machined in wet conditions, III) samples machined in cryogenic conditions.

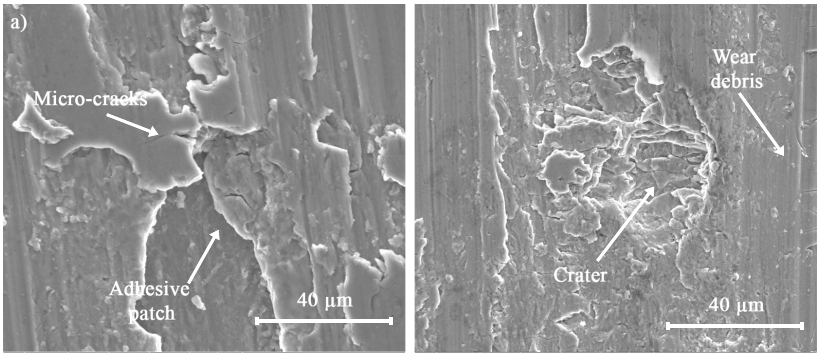

Figure 8.11: Magnified images of the wear scars reported in Fig. 5: a) 2500 image of the zone near the star in Fig. 5Ia; b) 2500Œ image of the zone near the star in Fig. 5IIa.

material wear [140].
The wear volume calculations showed that the dry machined samples were subjected to a double amount of volume loss compared to the cryogenic machined samples, which offered an improved wear behaviour thanks to their improved surface characteristics (see Table 8.6). This is in accordance with the Archard's wear rate law [132], which states that the volume of generated wear volume is inversely proportional to the hardness of the softest contacting surface.

8.2.5 Conclusions

In this work, the influence of the cooling conditions on the tribocorrosion behaviour of the Ti6Al4V titanium alloy obtained by two different fabrication process, namely wrought and Additive Manufactured through Electron Beam Melting, was investigated. Tribocorrosion tests were carried in a wet and temperature-controlled experimental apparatus in which the Ti6Al4V samples were made to slid against zirconia plates in order to reproduce as much as possible the human mouth conditions. The main results and conclusions obtained from this study can be summarized as follows:

- Cryogenic machining affected the surface properties of the EBM and wrought Ti6Al4V samples, inducing higher micro-hardness, higher compressive residual stresses and lower surface roughness than dry and wet cutting. The anodic polarization curves showed that the cryogenic machining also enhanced the corrosion behaviour properties, leading to the corrosion potential increase and corrosion current decrease. The increase in the corrosion performance was more evident for the EBM samples.

- The OCP values of the cryogenic machined samples recorded during the reciprocating sliding tests were arranged at a higher level compared

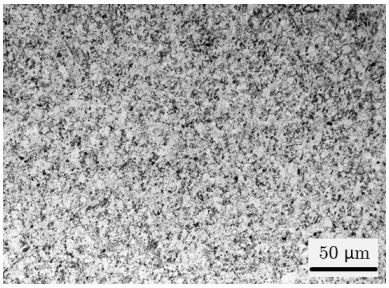

Figure 8.12: Optical micrograph of microstructure of titanium grade 2 in the as-delivered condition.

to the ones of the samples machined under wet and dry conditions, meaning they were less affected by the corrosive environment. This is a clear indication of enhanced tribocorrosion properties.

- The corrosion current values presented the same trend highlighted for the OCP values.
- The volume wear calculations confirmed the aforementioned results showing that the dry machined samples were characterized by a volume wear almost double compared to that of the cryogenic machined samples.
- The EBM samples presented an in-vitro behaviour similar to that of the wrought ones proving that this fabrication process can offer a suitable process route for manufacturing biomedical implants.

8.3 Ti-APP#3: Results and discussion

In this section, the results and discussion relative of titanium alloys Ti-APP#3 are reported. Details about the experimental machining campaign are described on Section 5.1.3 on page 60.

8.3.1 Characteristics of the substrate machined surface

The microstructure of the titanium grade 2 in the as-received condition is shown in Fig. 8.12.
Primary alpha (α)grains, intermingled with small yet noticeable pockets of beta (β) grains, can be noticed. These microstructural features are typical of the heat treatment to which the bar was subjected (see section 5.1.3 on page 60).

The microstructures of the sample A and sample C after machining are shown in Fig. 8.13, which clearly shows that the machining operation induced material alterations below the machined surface regardless of the

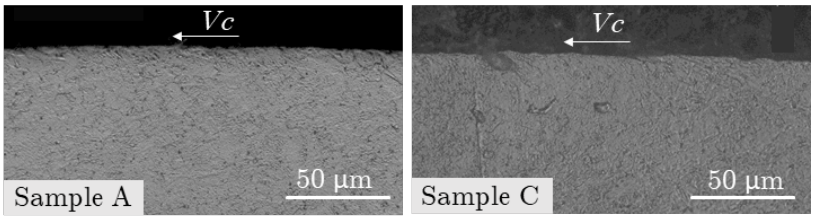

Figure 8.13: Optical micrograph of: in the left) sample A on the right) and sample C after machining and before coating deposition.

Table 8.11: Surface roughness parameters as a function of the cutting parameters reported on Table 5.4 on page 61.

	R_a (μm)	R_t (μm)
Sample A	0.54 ± 0.02	2.61 ± 0.1
Sample B	1.36 ± 0.02	6.25 ± 0.4
Sample C	0.67 ± 0.06	2.69 ± 0.1
Sample D	1.35 ± 0.03	6.08 ± 0.3

cooling strategy adopted during cutting. In both cases, the material was indeed heavily deformed along the cutting speed direction, as demonstrated by the presence of elongated grains. The depth of the machining-deformed layer below the machined surface was approximately 10 μm. Similar results were obtained for the other investigated feed.

Table 8.11 reports the values of the surface roughness parameters R_a and R_t according to the experimental plan of Table 5.4 on page 61. As expected, feed has the primary effect on the surface roughness, since it conditions the distance between two subsequent peaks. The change of feed, from 0.1 to 0.2 (mm/rev), contributes to increase Ra of approximately one order of magnitude. On the contrary, the cooling strategy marginally affects the surface finish, with just a slight difference only in the case of feed of 0.1 (mm/rev). R_t follows approximately the same trend of R_a, being influenced just by the feed.

However, the SEM analysis of the machined surfaces showed surface defects that were not possible to evidence on the basis of the surface roughness analysis. As previously indicated, preliminary BSED examinations of the surfaces revealed the total absence of adhered material from the tool. On the contrary, chip re-deposition and tearing were the main defects that characterized the machined surfaces.

From the comparison of the samples machined surfaces reported in Fig. 8.14, it can be noted that the wet cut samples are marked by a systematic redeposition of material, which can be either chip fragments or portions of

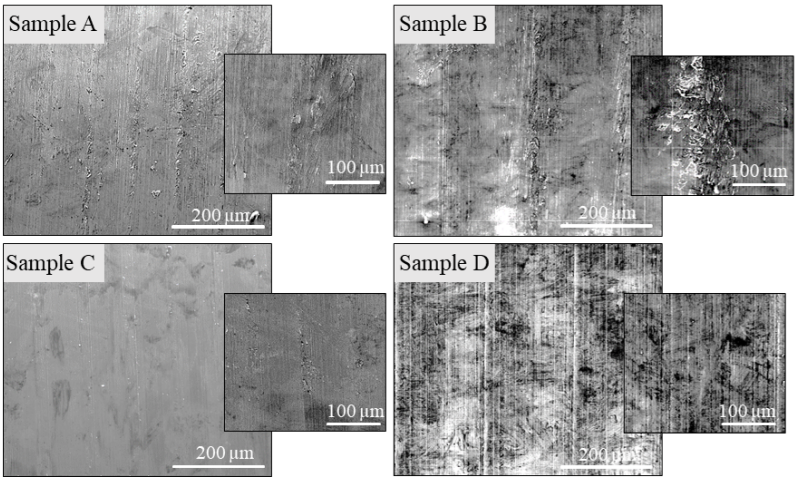

Figure 8.14: SEM images showing the surface defects as a function of the cutting parameters reported on Table 5.4 on page 61.

Built-Up Edge (BUE), smeared on the surface during the subsequent cutting operations (see the magnification of Fig. 8.14); on the contrary, the cryogenic machined samples at the same feed present a significantly less amount of the same kind of defects. Chip fragments weld on the machined surface as a consequence of the high temperatures generated in the cutting zone due to the titanium low thermal conductivity and high mechanical resistance; since cryogenic cooling allows reducing temperatures, it induces a lower density of this kind of defects [141].
Besides the aforementioned defects, the sample B is also characterized by the presence of tearing, whereas the sample D, cryogenically machined at the same feed, appears practically defects-free. Tearing may develop as a consequence of the presence of chip particles, which, acting as debris together with fragments of BUE, slide on the newly machined surface giving rise to a three-body wear mechanism. Since wear debris and BUE fragments are harder than the workpiece material, they scratch and tear away the machined surface [1]. Also the adhered material originates from fine chip particles and/or BUE fragments, which can weld onto the machined surface to form a composite surface, as a consequence of the high temperatures generated at the cutting interface that can enhance the welding/adhesion process [142]. Again, cryogenic cooling contributes to avoid these phenomena by reducing the cutting temperatures.
On this basis, it can be stated that surface defects are present on all the machined surfaces, regardless of the feed and cooling strategy, but their densities depend on the latter. In particular, the use of LN2 during machining helps in reducing significantly the formation of surface defects.

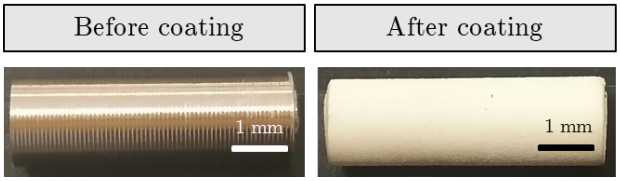

Figure 8.15: On the left: Sample B after machining and on the right) sample B after coating and sintering.

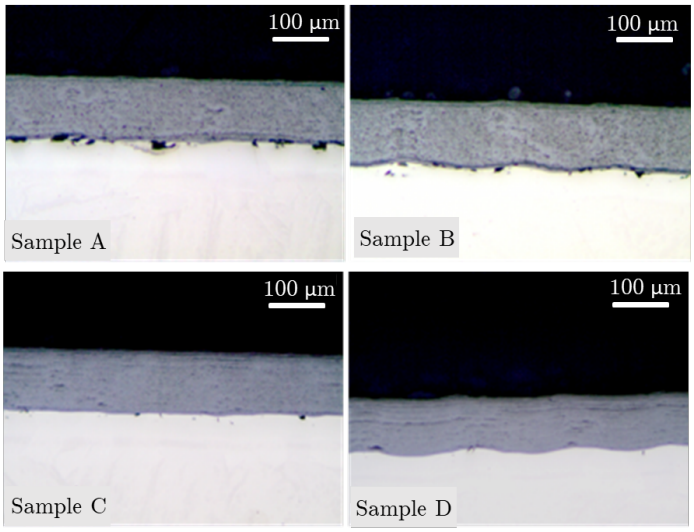

Figure 8.16: High magnification images of the area of interface between the coating and substrate as a function of the cutting parameters reported on Table 5.4 on page 61.

8.3.2 Characteristics of the coating-substrate interface

As can be observed, the sphene-based bioceramic homogeneously coats the dental implant prototype (see Fig. 8.15, for comparison after machining on the left and after coating and sintering on the right).
The coating after sintering was composed of $CaTiSiO_2$, TiO_2 and $CaTiO_3$.
The analysis of the coated samples shows that a homogeneous white coating which covers uniformly the whole surface of the samples. The coating presents always a layered structure, regardless of the strategy used to machine the substrate. The layered structure is witnessed by the images of Fig. 8.16, which represent the area of interface between the coating and substrate of the samples that were machined according to the experimental plan of Table 5.4 on page 61.
Table 8.12 reports measurements of the coating thickness for each sample. No substantial different values are induced by changing machining process parameters.
The microstructure of the A, B, C and D substrates after coating and sinter-

Table 8.12: Coating thickness of A, B, C and D samples. Cutting parameters are reported on Table 5.4 on page 61.

	Coating thickness (μm)
Sample A	119 ± 5
Sample B	121 ± 6
Sample C	116 ± 5
Sample D	113 ± 7

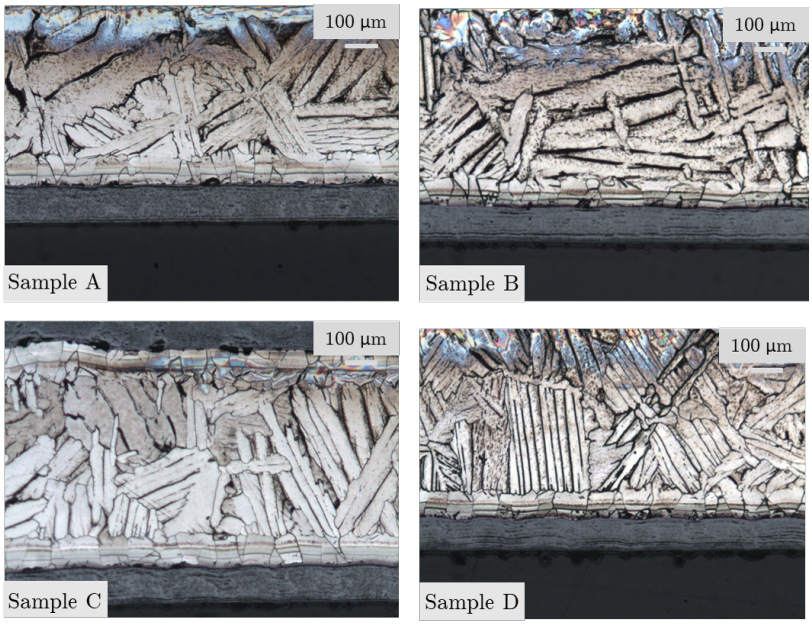

Figure 8.17: Microstructure of the substrates of the coated prototypes as a function of the cutting parameters reported on Table 5.4 on page 61.

ing is shown in Fig. 8.17. The typical titanium Widmanstatten structure can be observed, even though equiaxed grains are present close to the coating regardless of the strategy adopted to machine the prototype. The change of the alpha phase in the sub-surface layer from a lamellar morphology after machining (see Fig. 8.17) to a equiaxed morphology is a consequence of the machining-induced deformation that favours the mechanism of breaking up the alpha lamellae into globular grains during the sintering step after coating [143] [144]. In fact, globular grains are present only close to the machined surface where the machining-induced deformation is maximum.
It is worth to note that, since the cryogenic cooling induced a more strain hardened surface, it provided the driving force to the formation of a more refined microstructure compared to the wet condition. These observations

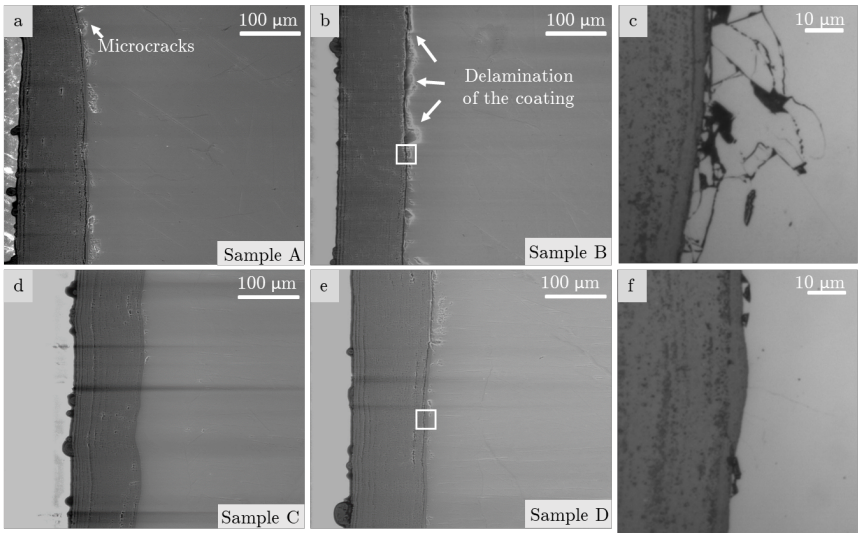

Figure 8.18: SEM images of sample sections showing the possible presence of defects at the coating-substrate interface. Cutting parameters are reported on Table 5.4 on page 61

are confirmed by the presence of small grains nearby the machined surface of the samples C and D. Furthermore, as a consequence of the long permanence at elevated temperature during sintering, the microstructure results highly coarsened with a consequent effect in reducing the material stiffness. However, this reduction is beneficial as it contributes to reduce stress shielding phenomena between the implant and the human bone, expecting to improve the implant performance on the long term.
The quality of the substrate-coating interface is improved when the substrate was machined using LN2, as can be observed in Fig. 8.18, where SEM images of polished sections are reported. The samples A and B show the presence of spread micro-cracks in correspondence of the interface, which may increase the probability of delamination of the coating. On the contrary, the samples C and D present significantly less amount of defects. These evidences are confirmed in Fig. 8.18c) and f), which shows a magnification of the areas reported in Fig. 8.18. The presence of defects at the coating-substrate interface may affect the coating adhesion, which was evaluated based on nano-indentation measurements.
Fig. 8.19 shows the nano-hardness maps of the samples A, B, C and D, with indication of the coating, interface and substrate areas. Each nano-hardness map corresponds to the array of indentations described in Section 7.1.4 . As expected, a considerable variation in hardness between the coating and the substrate is evident, being the titanium substrate much softer than the sphene coating (medium values range from 5 GPa for the titanium substrate to 13 GPa for the ceramic coating and 6 GPa for the interface). However,

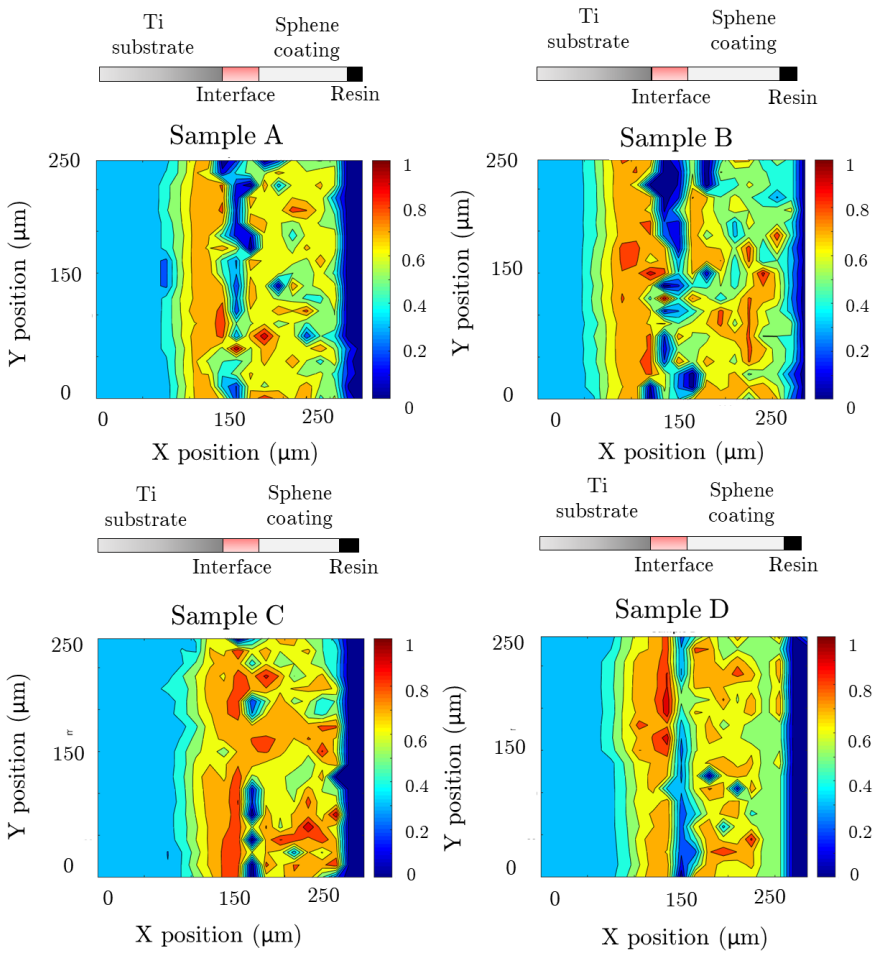

Figure 8.19: Nano-hardness as a function of the cutting parameters reported on Table 5.4 on page 61.

in each sample, the highest hardness values are present at both sides of the implant-coating interface zone. This may be ascribed to the combined effect of the more equiaxed titanium structure at the interface, which is more resistant than the lamellar one of the substrate, and of the migration of some hard elements from the coating to the substrate as observed in [145].
In addition, in [122], where hardness was measured at the interface by microhardness test using a Knoop indenter, values ranged between 1 and 4.5 GPa: in this case, the substrate was traditionally machined, double etched and sand blasted, whilst in this work the samples were cryogenic machined without any additional treatment to the surface.
The highest hardness values at the interface area are shown by the samples whose substrate was cryogenic machined (see the highest presence of red zones in the interface areas of Fig. 8.18 c and f), which is a proof of the highest resistance of the interface. The improvement induced by cryogenic cooling is attributable to the well-known Hall-Petch relationship, stating that the hardness is inversely proportional to the grain size.
The maps also confirm that cryogenic machined substrates provoked limited delamination of the coating compared to the corresponding wet machined ones, since the amount of blue-spots, which correspond to hardness values close to zero, are more diffused. These results are in agreement with those presented in Fig. 8.18, in which a defects mapping of the interface was carried out.
On the contrary, a clear influence of the feed and, therefore, of the surface roughness, cannot be identified, confirming previous research works [146] [147].

8.3.3 Conclusions

In the present study, dental implants prototypes made of pure titanium were turned with different feeds and cooling strategies.
After machining, the implants were coated with sphene ceramics and the coating-substrate interface behaviour was evaluated as a function of the cutting parameters.
The main results can be summarized as follows:

- All the machined surfaces were successfully coated, with a homogenous coating layer of 120 μm thickness, regardless of the cutting parameters.;

- A microstructural change of the titanium substrate, from a lamellar to an equiaxed structure, was found close to the coating, together with a general grain coarsening. The former change is due to the machining-altered layer that favoured the breaking up of the titanium lamellae during the sintering step after coating, whereas the latter was a consequence of the permanence at high temperature for a long period

during sintering. Overall, this contributes to reduce stress-shielding phenomena between the implant and the human bone.

- The feed applied during the turning operation had the main effect on the machined surface roughness; nevertheless, it did not significantly change the characteristics of the coating-substrate interface.

- The cooling strategies remarkably influenced the machined surface quality: cryogenic machining greatly contributed to generate a lower amount of defects on the machined surface compared to machining with a conventional cutting fluid. Similarly, a reduced amount of defects at the interface between the titanium substrate and the coating was found. Nano-hardness measurements showed that both the hardness of the cryogenic machined-coated surfaces were characterized by higher values than that of the same surfaces machined with a conventional cutting fluid, indicating a better adhesion of the coating. This improvement can be attributed to reduced delamination phenomena at the interface, as a consequence of the lower amount of defects on the substrate surface, together with the Hall-Petch effect that induced the formation of more refined, and thus more resistant structure, close to the machined surface.

- It is demonstrated that the newly proposed method, which combines cryogenic machining of the substrate and bioceramic synthesis and deposition, is capable of producing a bioceramic coating on pure titanium substrates characterized by a strong interface with no need of secondary operations such as etching and sand blasting of the substrate.

Chapter 9

Results and discussion for magnesium alloys

In this Chapter, results and discussion of the different case studies involving magnesium alloys are presented.
Details on the experimental campaign, materials and reasons that have pushed the study can be found in Section 5.2 on page 61.

9.1 Mg-APP#1: Results and discussion

In this section, the results and discussion relative of magnesium alloys Mg-APP#1 are reported. Details about the experimental machining campaign are described on Section 5.2.1 on page 61.

9.1.1 Microstructural and mechanical characterization of the machined surfaces

BF TEM images and SAD patterns of the samples sub-surface after machining are shown in Fig. 9.1.
The reported microstructures indicate severe grain refinement leading to the formation of nano-scale structures close to the machined surfaces, regardless of the adopted cooling strategy. The presence of nanostructures is confirmed by the SAD images that show a ring-like pattern indicative of high misorientation angle structures. In the case of dry cut sample (Fig. 9.1a), the diffraction pattern proves also the presence of grains of micrometre size just below the nano-crystalline layer, which is significantly less extended compared to the ones of the wet and cryogenic machined samples (Fig. 9.1b and 9.1c). On the contrary, the cryogenic machined sample presents the highest extension of the nano-crystalline layer, being four times and almost twice wider than the ones of the dry and wet cut samples, respectively (see table in Fig. 9.1).

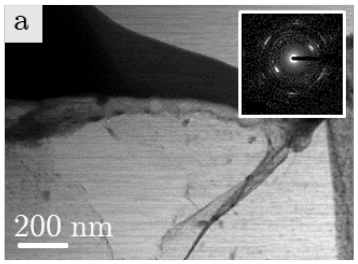

d

Cooling strategy	Nano-crystalline layer extension (μm)
Dry	1 ± 0.5
Wet	3 ±0.3
Cryo	4.5 ± 0.2

Figure 9.1: BF TEM micrographs and SAD patterns of: (a) dry, (b) wet and (c) cryogenic machined samples; (d) nano-crystalline layer extension.

These evidences are irrespective of the applied feed.
The nano-hardness measurements confirm a drastic increase of mechanical resistance compared to the base alloy as a consequence of the significant grain refinement (Hall-Petch effect), regardless of the cooling condition (see Table 9.1). Similar values are obtained at varying feed.
Depth profile of the residual stresses is shown in Fig. 9.2, whereas data are reported in Table 9.2: the presence of compressive residual stresses in the radial direction is highlighted for the cryogenic machined sample, whereas both the dry and wet cut samples always show tensile residual stresses.
The maximum residual stress (σmax) is 270 MPa (tensile) in dry condition, decreases to 110 MPa (tensile) in wet condition, and is further reduced to -143 MPa (compressive) in the cryogenic case.
On the contrary, the thickness of the layer affected by residual stresses is not sensitive to the cooling strategy, as approximately 200 μm below the machined surface every machining condition shows null stress.
The area interested by residual stresses (Ars) is significantly higher in the dry than in the cryogenic case, but always under a tensile state of stress (see table 9.2).
The reported results are for a feed equal to 0.01 mm/rev, but similar outcomes are found for the other feeds.

9.1.2 Wettability

Fig. 9.3 shows the feed and cooling strategy effect on the machined surface wettability, expressed in terms of contact angle: as expected, lower feed has a primary effect in increasing the contact angle, with cryogenic cooling en-

Table 9.1: Nano-hardness and Youngs modulus at the machined surfaces.

	Nano-hardness (GPa)	Youngs modulus (GPa)
As-delivered	1.35 ± 0.5	54 ± 3
Dry	2.09 ± 0.5	63 ± 3
Wet	1.73 ± 0.4	57 ± 3
Cryogenic	2.12 ± 0.5	70 ± 1

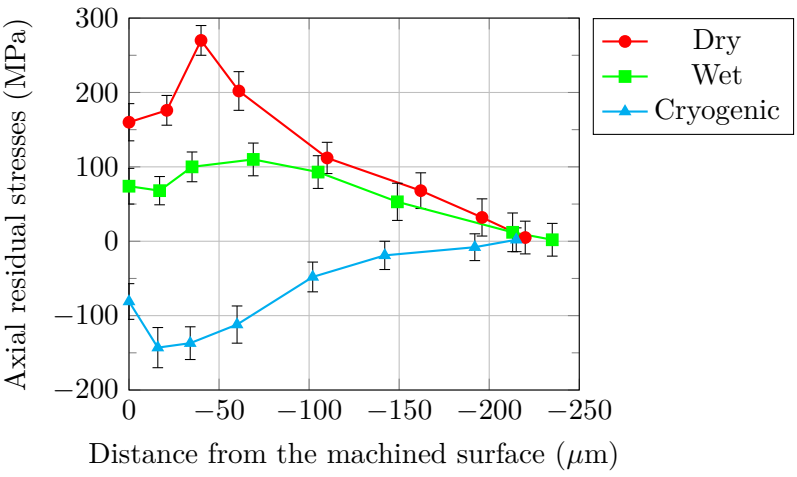

Figure 9.2: Depth profile of the radial residual stresses.

Table 9.2: Residual stresses parameters for 0.01 mm/rev feed.

Cooling strategy	σ_{max} (GPa)	Ars (MPa*μm)
Dry	270	33568
Wet	110	517858
Cryogenic	-143	-14630

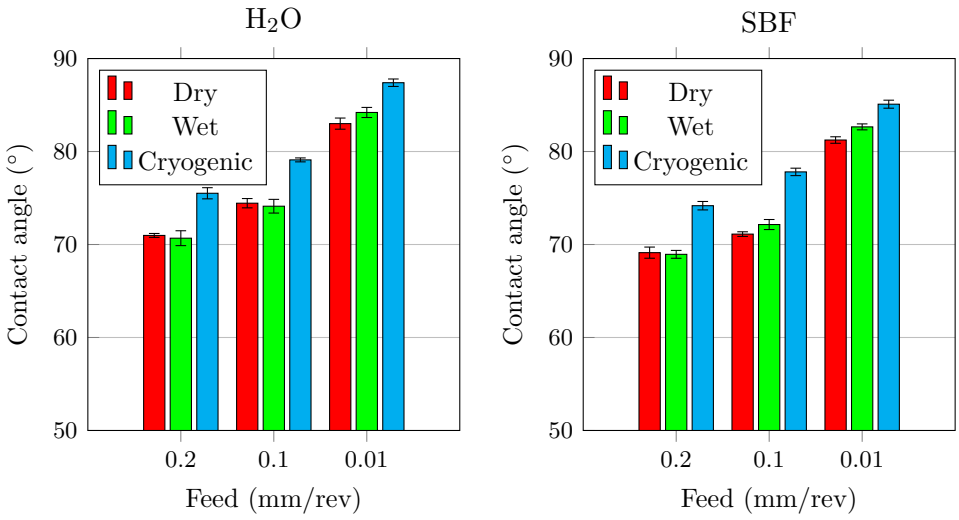

Figure 9.3: Effect of feed and cooling strategy on the contact angle in: (a) distilled water, and (b) SBF solution.

hancing this.

Both surface texture and surface energy play a role in influencing wettability: the former includes shape, size, aspect ratio, periodicity, orientation, and directionality of the surface as key-parameters, while the latter is mainly governed by the residual stress state [148] [149].

A number of surface parameters were analysed to correlate the machining-induced features to wettability; the ones that were physically significant and showed a correlation with wettability are here reported in Table 9.3, in addition to Sa that is listed as general information only. On the basis of the results reported in Table 9.3, it can be reasoned that the cooling strategy proves to affect mainly the shape of the feed marks.

The higher contact angles in both distilled water and SBF solution induced by cryogenic cooling can be indeed ascribed to the material displacement to the peaks (higher Spk values are obtained), which are also less spiky, as demonstrated by the decrease of the Sku.

Moreover, cryogenic machined samples are characterized by higher values of the skewness, which pertains to surfaces characterized by more peaks that protrude above the mean line. Overall, this contributes to increase the contact area supporting the liquid droplets, therefore inducing higher contact angles.

It is worth emphasizing that compressive residual stresses contribute to decrease wettability, amplifying the effect of the topography.

As expected, feed conditions in a much more sensible way wettability as determines the periodicity of the generated surface texture. This is clearly

Table 9.3: Areal surface texture parameters. Relative standard deviations: Sa< 10%, Spk < 10%, Sku < 15%, Ssk < 10% and Sal < 1%.

Feed (mm/rev)	Cooling strategy	Sa (μm)	Spk (μm)	Sku	Ssk	Sal (μm)
0.2	Dry	0.81	0.83	3.88	0.23	0.041
0.2	Wet	1.05	0.78	3.57	0.28	0.041
0.2	Cryogenic	1.24	1.05	1.92	0.72	0.045
0.1	Dry	0.37	0.34	3.34	0.36	0.021
0.1	Wet	0.38	0.47	3.85	0.29	0.023
0.1	Cryogenic	0.39	0.59	2.56	0.59	0.016
0.01	Dry	0.12	0.14	4.02	1.28	0.011
0.01	Wet	0.16	0.17	4.62	1.38	0.013
0.01	Cryogenic	0.10	0.24	3.11	1.54	0.008

evidenced also by the autocorrelation length parameter, which provides spatial information of the surface morphology [150].
Fig. 9.4 shows that the correlation between the contact angle and Sal parameter is independent of the cooling strategy. Surfaces with smaller Sal tend to have more peaks at any given height above the mean line [151], therefore show an increased contact area supporting the liquid droplets.
This is also confirmed by the increase of Ssk at decreasing feed. Furthermore, feed modifies the aspect ratio of the peaks whose height and width decrease at decreasing feed, as confirmed also by Spk.
In this case, the surface energy effect is irrelevant since feed does not influence the residual stresses.
The SEM evaluation of the machined surfaces shows defects at increasing feed. Regardless of the cooling strategy, systematic tearing of the surface is found at 0.2 mm/rev, whereas a totally defect-free surface is obtained at 0.01 mm/rev (see Fig. 9.5 a) and b).

9.1.3 Corrosion behaviour of the machined surfaces

The electro-chemical corrosion data from the potentiodynamic polarisation tests are reported in Table 9.4.
The corrosion potential of the cryogenic machined samples is always higher than the one of the other samples, regardless of the feed, indicating reduced tendency to be attacked by the corrosive media, therefore, a nobler behaviour.
Since the corrosion current density is directly proportional to the corrosion

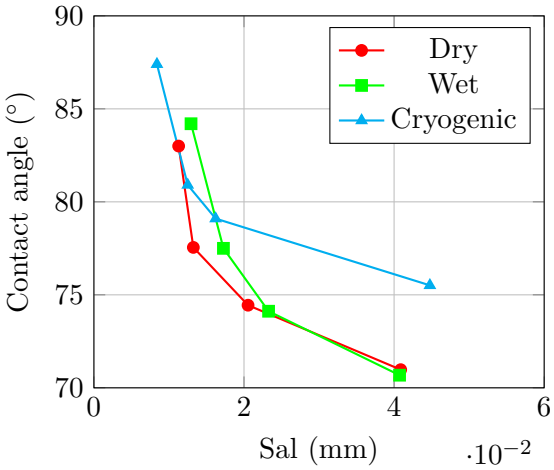

Figure 9.4: Correlation between Sal and contact angle after testing at feeds in the range 0.2-0.01 mm/rev (lower Sal values correspond to lower feeds)

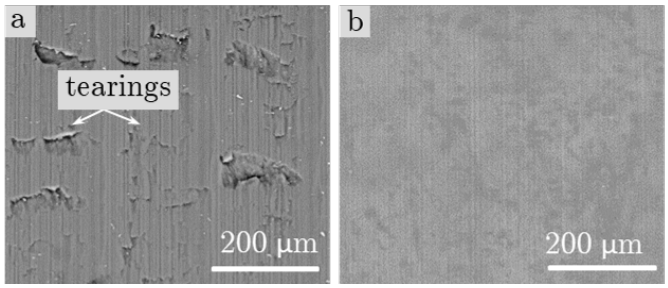

Figure 9.5: Surfaces cryogenic machined at: (a) 0.2 and (b) 0.01 mm/rev.

Table 9.4: Electro-chemical corrosion data.

	Feed (mm/rev)	E_{corr} (V/SCE)	I_{corr} (μmA/cm^2)
As-delivered	0.2	-1.84 ± 0.02	10 ± 3
Dry	0.2	-1.68 ± 0.02	10 ± 3
Wet	0.2	-1.79 ± 0.01	5.5 ± 2
Cryogenic	0.2	-1.77 ± 0.03	2 ± 1
Dry	0.1	-1.87 ± 0.015	5 ± 2
Wet	0.1	-1.79 ± 0.025	5 ± 2
Cryogenic	0.1	-1.79 ± 0.03	2 ± 0.5
Dry	0.01	-1.79 ± 0.03	7 ± 3
Wet	0.01	-1.8 ± 0.01	3 ± 1
Cryogenic	0.01	1.69 ± 0.01	1 ± 0.5

rate, a significant enhancement of the corrosion resistance, an order of magnitude, is found in the case of cryogenic machined samples, at the lowest feed, as compared to the pre-machined sample.
It is worth noting that, even if the dry and wet cut samples show a nanocrystalline layer like the cryogenic one, they also show a residual tensile state of stress, which is detrimental for the corrosion resistance.
The feed reduction to 0.01 mm/rev has a further positive effect since it allows the reduction of the corrosion current density, regardless of the cooling condition, thanks to the reduced wettability (see Fig. 9.3) and the generation of a defect-free surface (see Fig. 9.5).
Fig. 9.6 a) reports the measurements of hydrogen amount and pH level in the SBF solution, which indicate a controlled-time dependence of corrosion desirable for biodegradable implants [97].
Both the curves represent indeed a fast first stage when the corrosion starts, a second stage, during which the degradation process reaches a stationary level, and is favourable for the bone healing and anchoring without loosing mechanical resistance, and a third stage during which the corrosion process recommences at a much higher rate.
During the first stage, magnesium quickly reacts with water to form magnesium hydroxide, which, in turn, reacts with the present inorganic species to form hydroxyapatite and calcium phosphate that slow down the corrosion process during the second stage, acting as a protective layer.
After approximately one week, the magnesium hydroxide starts interacting with the Cl- ions present in the solution to form magnesium chloride, which speeds up the magnesium dissolution and increases the pH level. Therefore, within the third stage, the magnesium is much more susceptible to be eroded and corrosion pits form.
Fig. 9.6 shows that samples machined with different cooling strategies have similar hydrogen production, but the corrosion morphology is significantly different.
The profiles of the corroded surfaces in Fig. 9.7 confirm indeed that the corrosion pits of dry and wet cut samples are more evident than those of the cryogenic machined sample.
To this regard, residual stresses play a fundamental role, as a residual tensile state of stress contributes to broaden corrosion features such as pits.
Fig. 9.8 reports the section of the corroded samples after one week of hydrogen evolution tests. The dark grey coloured zone is indicative of not-corroded surface, while the white zones indicate corroded areas.
The dry machined sample is characterized by a much more severe attack than the wet and cryogenic machined samples: this can be attributed to its much less extended nano-crystalline layer compared to the other samples, which may accelerate the degradation process.
While the results in Fig. 9.8 are for a feed equal to 0.01 mm/rev, similar outcomes are found for the other feeds.

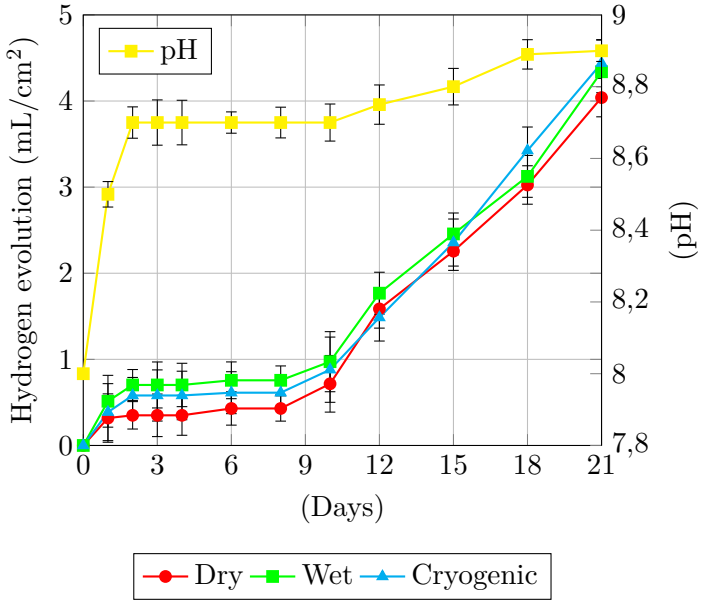

Figure 9.6: Hydrogen evolution and pH measurements.

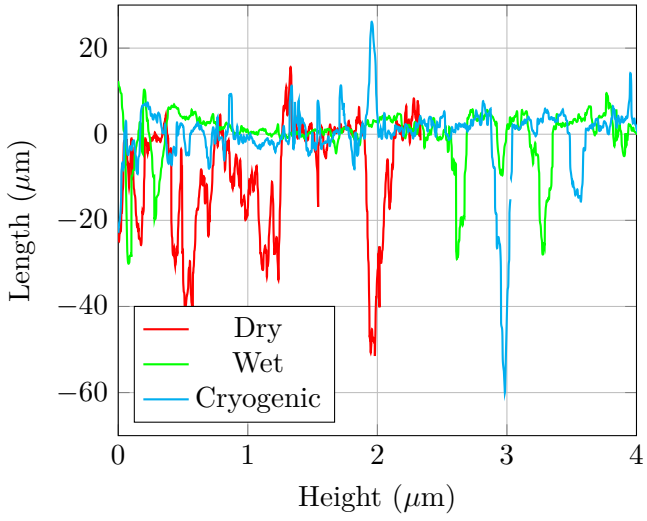

Figure 9.7: 2D line profiles of the corroded surfaces for samples machined under different cooling conditions at 0.1 mm/rev.

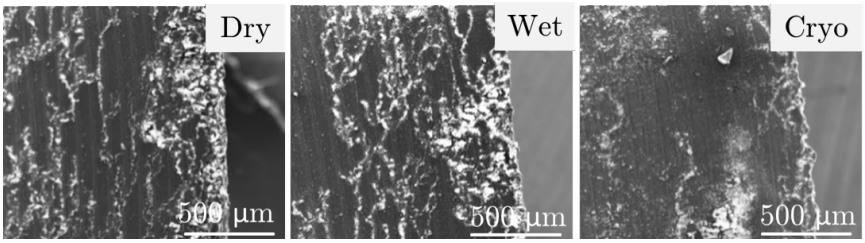

Figure 9.8: SEM images of the corroded surfaces as a function of different cooling conditions.

9.1.4 Cytocompatibility results

Fig. 9.9 shows the cytotoxicity of the samples expressed as % cell viability with respect to the control, which is represented by a standard polymer flat surfaces.
All of the samples exhibited good viability towards MC3T3-E1 cells. Statistically, no significant difference was observed among all the samples.
Fig. 9.10 shows the SEM images of cells adhering on the surface of the samples.
After 24 h of incubation, cells started to form groups and interconnect themselves on the substrates. Dry and cryogenic samples show cell adhesion similar to each other.
After 72 h, cells continues to growh and they covered the entire surface of the substrate.
Cell spreading and interconnections among the cells indicate the excellent biocompatibility nature of the magnesium.
No significantly differences bewteen the surfaces were found, proving that cryogenic does not alter the compatibility of the alloy and it can be taken into consideration as alternative manufacturing chain for manufacture biomedical devices.

9.1.5 Conclusions

Different cooling conditions, namely dry wet and cryogenic, and feed, namely 0.2, 0.1 and 0.01 mm/rev, were used to machine the biodegradable AZ31 magnesium alloy.
The main conclusions can be summarized as follows:

- Even if each cooling methods led to the formation of a SPD layer near the machined surface, only cryogenic machining contributes induce a compressive residual stress state into the machined workpiece;
- The strategy of decreasing the feed rate was used in order to modify the machined surface topography and, as consequences, to reduce the machined surface wettability. A reduction in wettability of 13% was

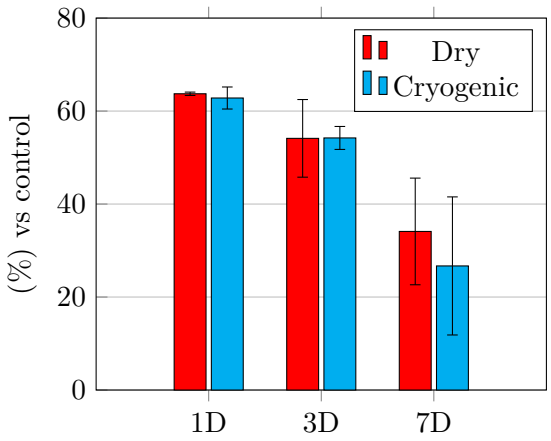

Figure 9.9: Cell adhesion on machined magnesium surfaces and control ones at 1 day, 3 days and 7 days from seeding.

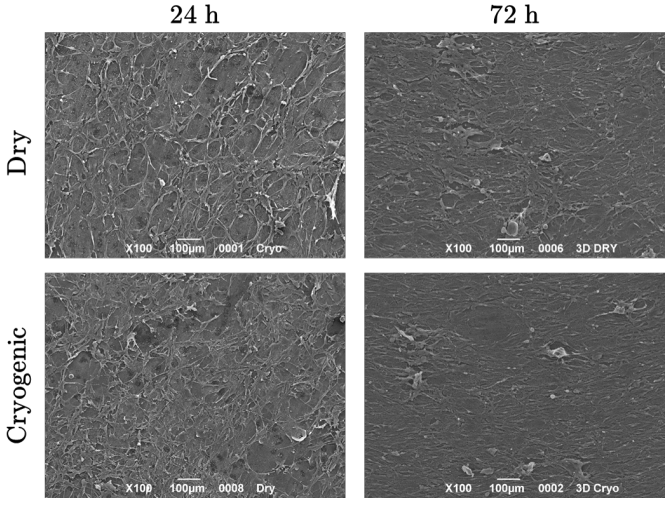

Figure 9.10: SEM images of cells adhered on machined substrates in dry and cryogenic conditions.

reached when a feed rate was decreased of an order of magnitude. Such changes is well explained by the generated profiles, which result characterized by an higher amount of peaks that protrude above the mean line in the case of the lowest feed, enhanced in the case of cryogenic cooling conditions;

- Potentyodynamic polarization curves and degradation studies showed that an improvement in corrosion behaviour was achieved by combining the aforementioned machining strategies. The obtained results demonstrated that a careful choice of the machining process parameters brought important changes in terms of both microstructure and topography that can be exploited to enhance the corrosion resistance of magnesium alloy biomedical devices inside the human body.

9.2 Mg-APP#2: Results and discussion

In this section, the results and discussion relative of magnesium alloys Mg-APP#2 are reported. Details about the experimental machining campaign are described on Section 5.2.2 on page 63.

9.2.1 Chip morphology

Fig. 9.11 shows pieces of chips obtained under the cutting conditions of Table 5.8 on page 65.
The LSEM process was able to suppress the chip segmentation, exploiting the combination of pressure and heat arisen from the plastic work.
In fact, it is worth noting that the obtained chips were always continuous, except for the C1 case in which fractures at regular intervals of 50 mm were found. This can be attributed to the low cutting speed, and, therefore, higher cutting time compared to the other cases, during which the temperature was kept very low by the constant liquid nitrogen adduction, which contributed to reduce the material plasticity.
On the other hand, as regards the D1 case, the temperature was high enough to form continuous chips, but not enough to avoid the presence of cracks along the chip section.
In the C2 case, the temperature rises due to cutting promoted a sensible reduction of the shear bands, even though they were still present.
On the contrary, the chip obtained under D2 conditions was perfectly continuous and defect-free.
At the highest cutting speed, the increase of shear strain rate induced a localized heat generation in the deformation zone, which enhanced the material plasticity and helped avoiding shear banding of the chips; therefore, even in cryogenic conditions, the chips were found continuous and defects-free.

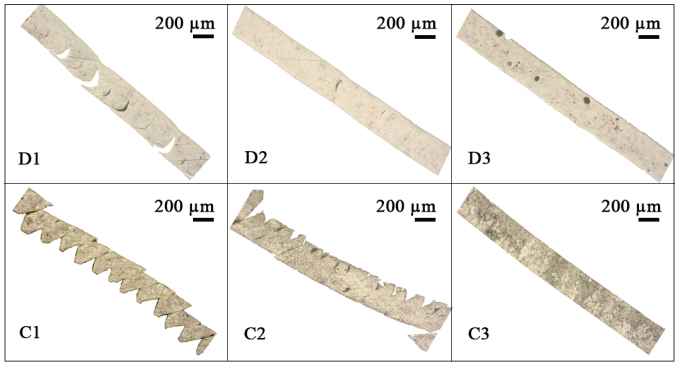

Figure 9.11: Chips obtained under the cutting conditions of Table 5.8.

9.2.2 Microstructural and mechanical characterization of the LSEMed surfaces

Fig. 9.12 shows the cross-section microstructure of an LSEMed sample.
The presence of two different zones, namely a UFG region and a deformed region, both pertinent to the deformation layer generated by LSEM, is highlighted.
The UFG region lies at most within the first 50 μm below the LSEMed surface.
Table 9.5 reports the thickness of the UFG region as a function of the cutting conditions. The UFG region is formed by heavily deformed grains, strained and elongated along the cutting speed direction. Ultrafine grains are present, drastically reduced in size compared to the ones of the annealed structure. In fact, the severe plastic deformation imposed by LSEM provoked the subdivision of the original coarse grains into finer twin platelets. At increasing strain in the sample, dislocation movement, cross slips and dislocation arrays were formed within the twin platelets, leading to their very significant reduction in size (see Fig. 9.12(b)).
The deformed region corresponds to a domain that is not severely strained as the first zone, but is still characterized by a large amount of twins within the grains typical of the alloy in the as-delivered condition. Below the aforementioned zones, the grain structure recovers the initial annealed microstructure condition.
Fig. 9.13 shows two different microstructures obtained under dry and cryogenic cooling conditions at the same cutting speed.
The comparison proves that under cryogenic cooling a higher grain refinement can be achieved.
Moreover, as reported in Table 9.5, the extension of the UFG region was slightly increased when LN_2 in LSEM, was applied especially when the highest cutting speed was adopted. In addition, the microstructural analysis showed that the density of the twinning lamellas in the deformed region of

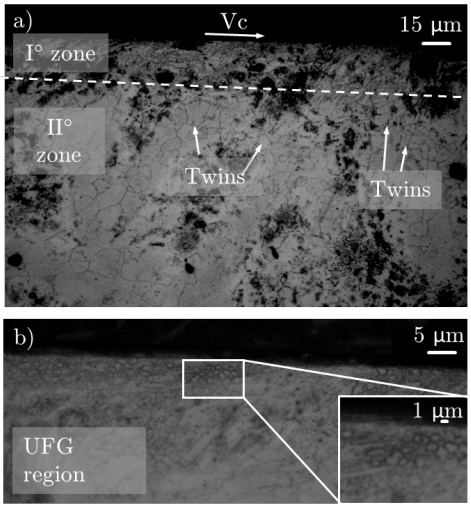

Figure 9.12: (a) Example of the obtained microstructure on the workpiece after LSEM for the C2 case. (b) Magnified images of the UFG region present in (a).

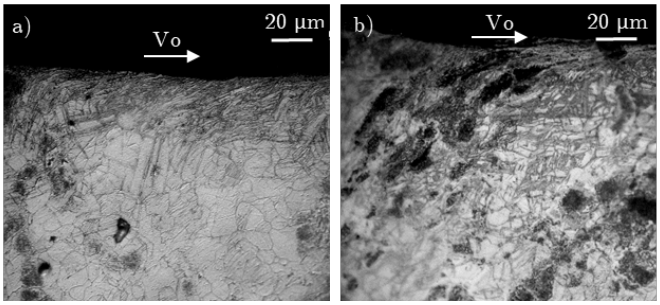

Figure 9.13: Microstructures of (a) the D3 sample, and (b) of the C3 sample. Cutting conditions are reported on Table 5.8.

Table 9.5: Thickness of the UFG zone as a function of the cutting conditions of Table 5.8.

Test ID	UFG region thickness (μm)
D1	27.7 ± 4
D2	30.7 ± 4
D3	33.9 ± 6
C1	26.5 ± 2
C2	32.8 ± 2
C3	45 ± 4

Table 9.6: Average grain size of the obtained chips as a function of the cutting conditions reported on Table 5.8.

Test ID	Average grain size (μm)
Annealed	15 ± 4
D1	9.6 ± 4
D2	3.0 ± 2
D3	3.0 ± 1.8
C1	9.8 ± 5
C2	10.6 ± 4
C3	10.0 ± 6

the cryogenic machined samples was higher compared to the dry cut ones. Table 9.5 shows also that the cutting speed increase influences the extension of the UFG region. The change of the cutting speed from 30 m/min to 120 m/min contributes to significantly increase the thickness of the affected layer.
Fig. 9.14 shows the variation of micro-hardness from the LSEMed surface to the substrate of the workpiece.
A severe hardening that extends up to several tens of microns beneath the surface is present in all the investigated conditions. In particular, the C1 case presents the highest micro-hardness among all the conditions, reaching an increase up to 64% compared to the base alloy.
In general, cryogenic machined samples present higher micro-hardness compared to the dry cut ones, especially at the lowest cutting speed.

9.2.3 Microstructural and mechanical characterization of the LSEM-ed chips

Fig. 9.15 shows optical micrographs of typical LSEM-ed chip microstructures, while table 9.6 reports their average grain size.
Chips of the D2 and D3 cases (Fig. 9.15a) show an equiaxed and defects-free microstructure indicative of the occurrence of dynamic recrystallization [21]. The average grain size of the D2 case chips is 3 μm, meaning a five times refinement of the grain size with respect to the one of the base alloy after the annealing treatment. A similar equiaxed microstructure was observed in the D3 case: doubling the cutting speed from 60 m/min to 120 m/min did not provide any evident microstructural change in terms of grain growth.
This can be attributable to the achievement of a saturation value for the cutting speed, above which the temperature, which is the main driving force to the grain growth, does not increase anymore proportionally with the cut-

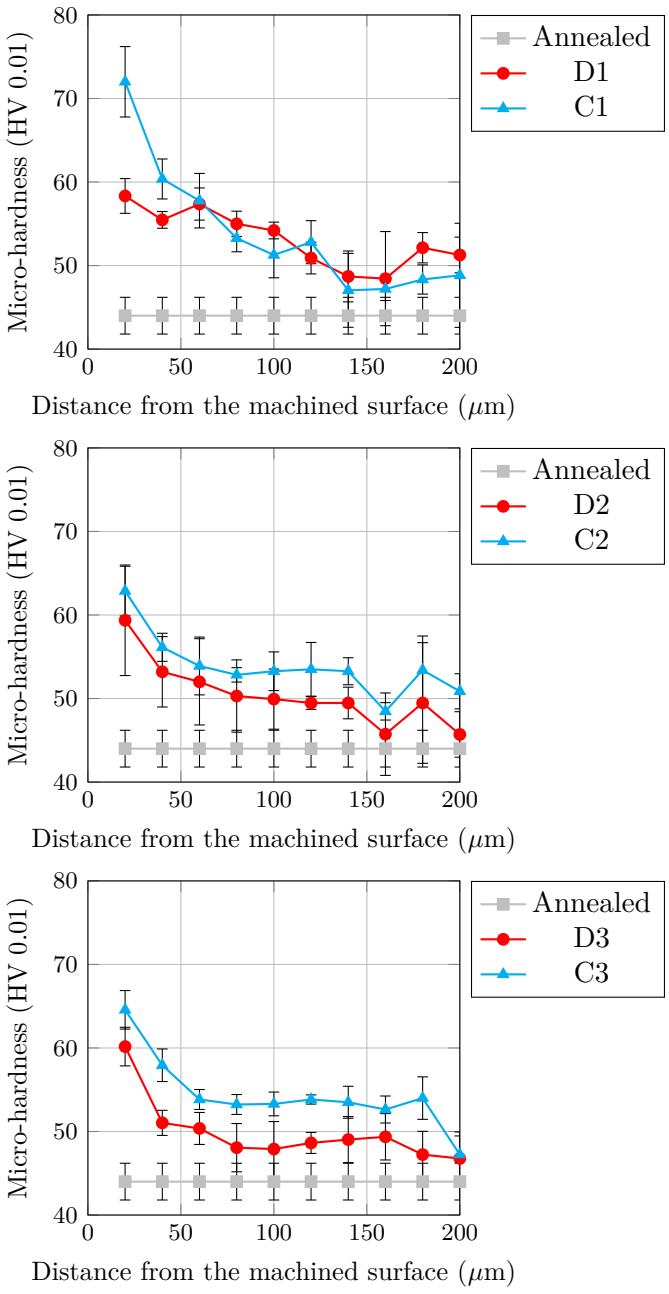

Figure 9.14: Micro-hardness as a function of the cutting conditions of Table 5.8.

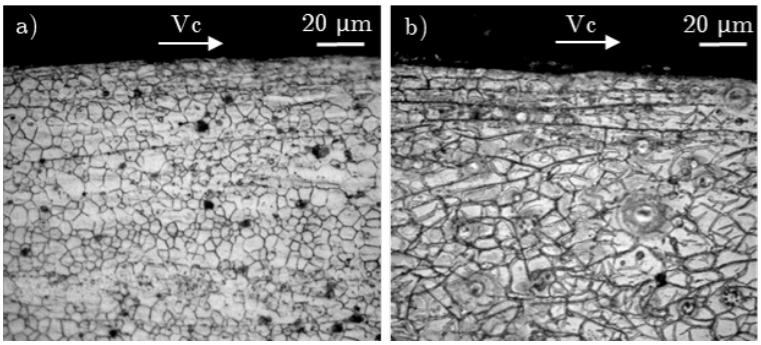

Figure 9.15: Microstructures of the LSEMed chips: (a) D3 case, and (b) C3 case. Cutting conditions are reported on Table 5.8.

ting speed [21].
To be noticed that the relatively low standard deviations in Table 9.6 are a sign of very homogenous microstructures.
On the contrary, the LSEM-ed chips obtained in cryogenic conditions together with the D1 case chips show a microstructure similar to the one in Fig. 9.15(b) for the C3 case, which reflects a cold-worked type microstructure, confirmed by the presence of twins within the grains and microstructural features that cannot be resolved through optical microscopy.
Table 9.6 shows also that the resulting grain sizes are higher compared to the D2 and D3 cases. As regards the cryogenic cases, regardless of the cutting speed, this can be attributable, to the application of liquid nitrogen, whereas, in D1 case, to the relatively low cutting speed; in both conditions, the temperature remains always below 200°C, namely the threshold value necessary to start recrystallization phenomena in magnesium alloys [152].
Fig. 9.16 shows the micro-hardness values of the LSEM-ed chips as a function of the cutting parameters.
In general, the abduction of liquid nitrogen leads to a micro-hardness increase.
In particular, the C1 case chip presents the highest microhardness, with an increase of more than 90% compared to the base alloy, reflecting what happened to the machined bar (see Section 9.2.2).
This behavior can be explained by the fact that coldworked microstructures preserve dislocations and twins that both contribute to increase hardness, as a result of the lowest process temperature kept for the longest time. Within dry cases, D1 chips present the highest micro-hardness due to the preservation of a cold-worked microstructure. The strength decrease found in the D2 and D3 cases is compatible with recrystallized microstructures, where dislocations are annihilated due to the nucleation of new grains.

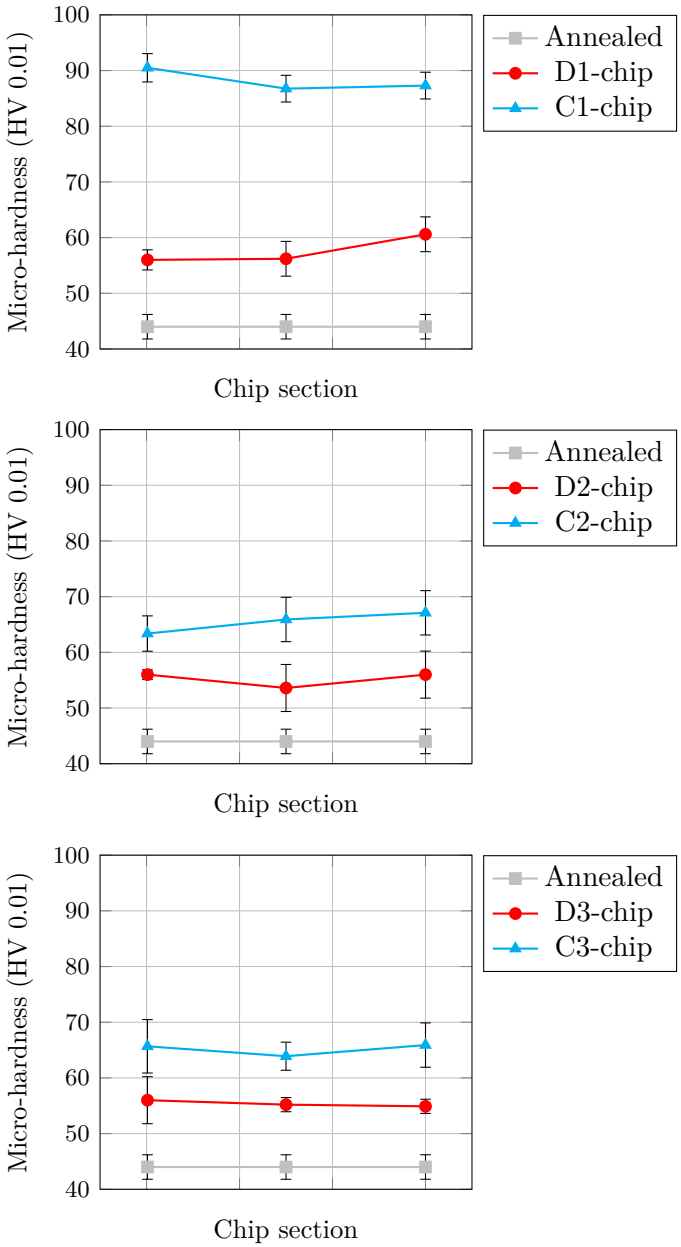

Figure 9.16: Micro-hardness of the LSEMed chips as a function of the cutting conditions reported on Table 5.8.

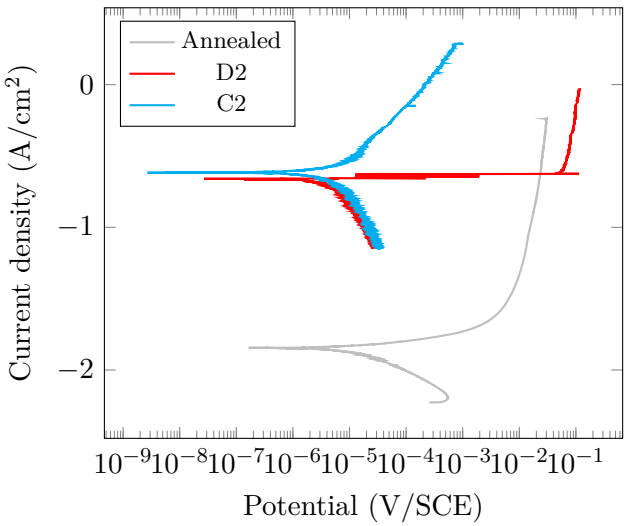

Figure 9.17: Potentiodynamic polarisation curves in SBF solution at 37°C of the machined bar obtained when machining under D3 and C3 conditions. Cutting conditions reported on Table 5.8.

9.2.4 Corrosion behavior of the LSEMed surfaces

Fig. 9.17 reports the potentiodynamic polarization curves of the D2 and C2 cases as well as the one of the base alloy in annealed conditions.
Very similar corrosion curves were obtained for the other cutting conditions, and therefore, not here reported.
Table 9.7 reports the electrochemical data derived from the potentiodynamic polarization curves for all the investigated conditions.
In general, an improvement of the corrosion performances can be found compared to the annealed condition as the curves are all shifted towards higher potentials and lower corrosion densities.
Cryogenic cooling led to a slight improvement of the corrosion resistance, and in particular to a very different trend of the anodic branch of the curve. As a matter of fact, in case of the dry LSEMed samples, at a potential equal to 0.65 V, the corrosion curve presents a plateau. This is a sign of an increase of the corrosion tendency, as the corrosion current presents a sudden increase, reaching an extremely high value comparable to that of the annealed condition.
The corrosion current has in fact a direct relationship with the corrosion rate: this means that an increase of Icorr corresponds to an increase of the mass lost by the implant during its service-life in the human body.
As regards the cutting speed, also in this case a clear influence cannot be identified.
After LSEM, the machined bar grain size decreased in a sensible way compared to the initial one, as shown in Fig. 9.12.

Table 9.7: Electrochemical corrosion data of the LSEMed surfaces as a function of the cutting conditions reported on Table 5.8.

Test ID	E_{corr} (V/SCE)	I_{corr} ($\mu A/cm^2$)
Annealed	-1.84	10
D1	-0.72	7
D2	-0.66	6
D3	-0.58	10
C1	-0.69	9
C2	-0.62	2
C3	-0.59	2

Previous studies [153], [154] reported that finer grains could enhance the corrosion properties of magnesium alloys. Finer grains are usually associated with the formation of a strengthened passive film [155].
The presence of a plateau in the corrosion curves relevant to dry cutting can be attributed to a breakdown of the material surface oxide. The higher refinement provided by cryogenic conditions gave enough strength to the surface oxide to avoid its rupture.

9.2.5 Corrosion behavior of the LSEMed chips

Fig. 9.18 reports the potentiodynamic polarization curves of the chips obtained under D3 and C3 cutting conditions as well as the one of the base alloy in annealed condition, while Table. 9.8 reports the electrochemical data derived from the curves.
It is worth to underline that only the LSEMed chips with the best surface quality for each cooling condition were tested for corrosion, namely the D3 and C3 cases, since the presence of cracks drastically increases the surface exposed to the aggressive environment, therefore altering the corrosion curves. Both the curves relevant to chips machined under dry and cryogenic conditions are shifted towards higher potential compared to the base alloy. The D3 case shows a corrosion current that is halved compared to the one of the base alloy, whereas the cryogenic chip shows an increase of a half.
The improvement of the corrosion performances in the D3 case chip can be attributed to its grain refinement, since the grain boundaries act as a physical corrosion barrier [156].
C3 LSEMed chips present coarser grains than the D2 case chips, but finer than the base alloy, and, unexpectedly, they are characterized by higher corrosion current than the latter.
This can be attributable to the presence of dislocation features characteris-

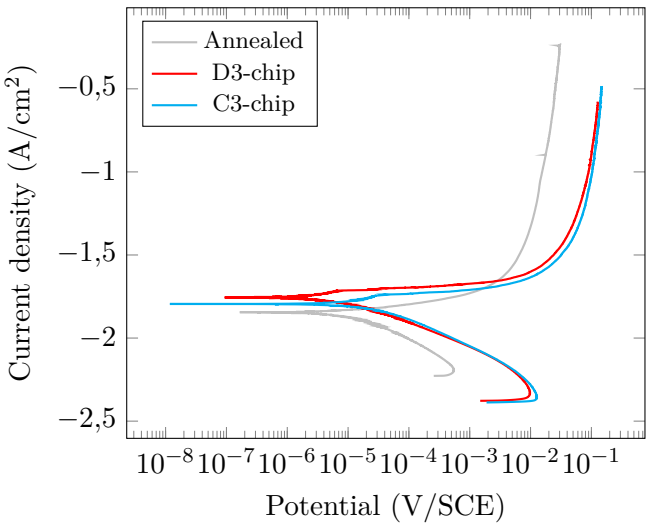

Figure 9.18: Potentiodynamic polarisation curves in SBF solution at 37°C of the chips obtained when machining under D3 and C3 conditions. Cutting conditions are reported on Table 5.8.

Table 9.8: Electrochemical corrosion data of the obtained chips. Cutting conditions are reported on Table 5.8.

Test ID	E_{corr} (V/SCE)	I_{corr} (μA/cm^2)
Annealed	-1.84	10
D3	-1.82	5
C3	1-1.8	15

tic of cold-worked microstructure, which accelerate the anodic metal dissolution, as a consequence of a local reduction of equilibrium potential in the vicinity of dislocations [157].

9.2.6 Conclusions

In this study, LSEM was used to induce surface modifications on AZ61 magnesium alloy workpieces.
Different cooling strategies and cutting speeds were applied and their effects on the surface integrity and corrosion resistance were evaluated. The main findings can be summarized as follows:

- The strategy of applying liquid nitrogen showed potentialities to obtain a machined surface with enhanced mechanical and corrosion characteristics.
  In fact, the cryogenic-machined surfaces were characterized by a greater

grain refinement and slightly more extended SPD layer compared to the corresponding dry ones.
In addition, harder surfaces were observed when liquid nitrogen was applied.
Also the corrosion properties were positively influenced, as the characteristic plateau of the corresponding dry curves, indicative of a lower corrosion resistance, was not detected.
On the contrary, the main effect of the cutting speed, regardless of the cooling strategy, is limited to the formation of a thicker UFG region on the subsurface of LSEMed samples at increasing cutting speed.

- In general, hard chips characterized by a cold-worked microstructure are obtained when machining with liquid nitrogen, which can be the cause of the defects they present, as a consequence of the overall reduction of the process temperature, especially when low cutting speeds are set.
  On the contrary, the adoption of dry cutting and higher cutting speeds favors the formation of softer and completely recrystallized chips.
  Corrosion results indicate that LSEMed chips obtained under dry conditions are characterized by a reduced corrosion current with the respect to the annealed condition.

9.3 Mg-APP#3: Results and discussion

In this section, the results and discussion relative of magnesium alloys Mg-APP#3 are reported. Details about the experimental machining campaign are described on Section 5.2.3 on page 64.

9.3.1 Microstructural and mechanical characterization of the UVTed samples

The optical metallographic analysis reported on Fig. 9.19 did not demonstrate presence of any grain structure different from that observed in the bulk, non-machined state of this alloy.
A thin layer (5-10 μm) characterized by heavily deformed grains along the cutting direction appeared just under the machined surface.
The thickness of that layer seems not been influenced by turning techniques, namely CT and UVT.
Fig. 9.20 reports the measured nano-hardness values as a function of the distance from the machined surface.
The absence of significant hardness changes confirms what evidenced by micrograph observations, namely that only a very thin layer was influenced by the cutting process.
Nano-hardness confirm that no significant differences between CT and UVT

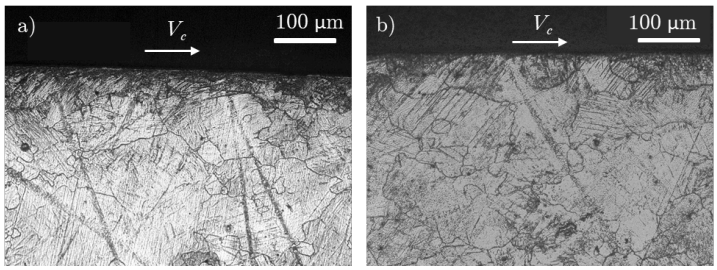

Figure 9.19: Microstructures of the samples: (a) Sample 1 case, and (b) Sample 2 case. Cutting conditions are reported on Table 5.9.

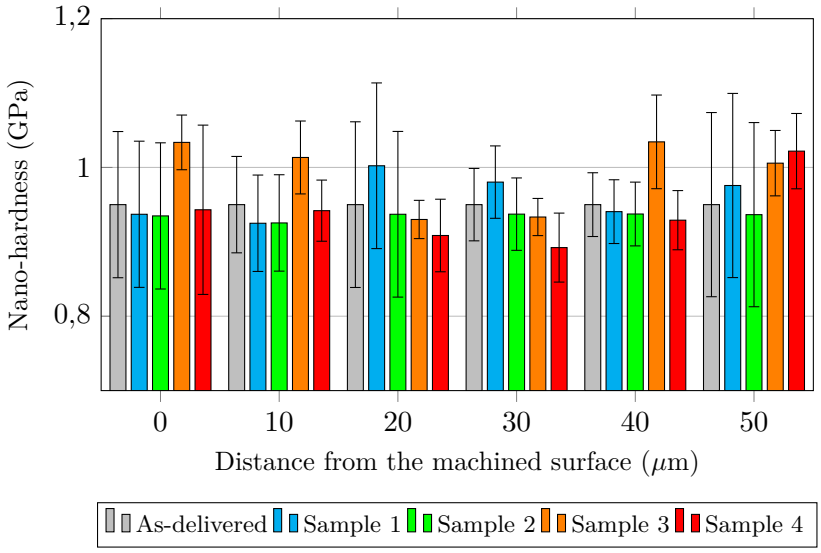

Figure 9.20: Nano-hardness of the UVT-ed samples as a function of the cutting conditions reported on Table 5.9.

are present. The fact that ultrasonically machined surfaces show hardness comparable to those of CT is beneficial since the bulk hardness of the material is preserved.

9.3.2 Surface finish characterization of the UVTed samples

In this Section, surface finish measurements are reported.
First, the influence of CT and UVT on surface topography parameters is addressed; then, the effect of UVT process parameters is evaluated.

Comparison between CT and UVT

Fig. 9.21 reports the comparison between surface area parameters obtained after CT and UVT for all the investigated conditions.
The obtained results show that UVT influences notably the morphology of

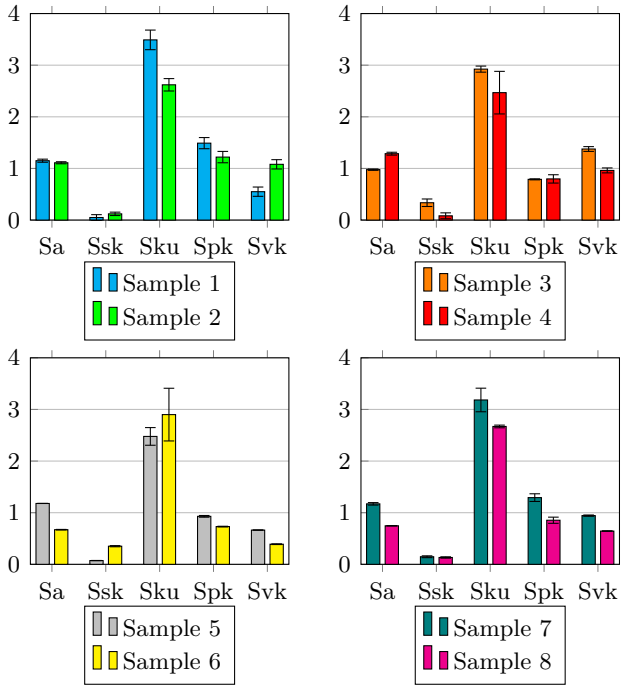

Figure 9.21: Surface texture parameters as a function of the cutting conditions reported on Table 5.9.

the profile by changing the material distribution, as demonstrated by the different values of all the reported surface texture parameters.
It is worth to note that a clear trend cannot be identified, since surface roughness parameters depend also from the other cutting parameters adopted.
Sa, which is still the most important parameter for general application, is reduced when a DoC of 0.1 mm is adopted in the case of UVT, regardless the cutting speed adopted.
Also functional parameters, like Svk and Spk, resulted dependent from other variables like DoC or cutting speed.
In particular, it can be found two different situations: in the case of fixed DoC, the profile along the feed is not influenced by UVT process and the roughness parameter do not present any clear trend.
In the case of fixed cutting speed, changing DoC contributes also to vary the form of peaks along the feed direction, besides the vibration's one. In that case, it is impossible to attribute the changing into roughness parameters only to the presence of the texture introduced by the vibration of the cutting tool.
Thus, suggest that the investigated parameters are not suitable to describe the texture generated by UVT. Thus can be clearly demonstrated by looking at the partial profiles of the surfaces measured after machining reported in Fig. 9.22.

Changing the cutting speed, the profile along the feed is only sligthly influenced by UVT process, while on the perpendicular direction is random for CT while textured for UVT. In the case of a DoC of 0.1 mm instead, the profile along also profile along the feed is influenced and this is well reflected by the surface roughness parameters.
Thus confirm that surface roughness parameter are well indicators of what happened along the feed profile but they cannot describe well the generation of a texture by UVT.
Fig. 9.23 shows the main defects found on the surface of the samples machined using CT and UVT.
SEM analysis of the machined surfaces is essential to identify defects that are not possible to detect by the surface roughness measurements, therefore providing an evaluation of the machined surface nano-texture.
Tearing and feed marks irregularities represent the only defect-type found in the samples machined using both CT and UVT.
Tearing can develop from the action of debris of the cutting tool, formed as a consequence of tool wear, together with fragments of Built-Up Edge (BUE), which slide on the newly machined surface giving rise to a three-body wear mechanism. Since wear debris and BUE fragments are harder than the workpiece material, they scratch and tear away the machined surface.
Deformation of feed marks occurs as a result of the material plastic flow during cutting.

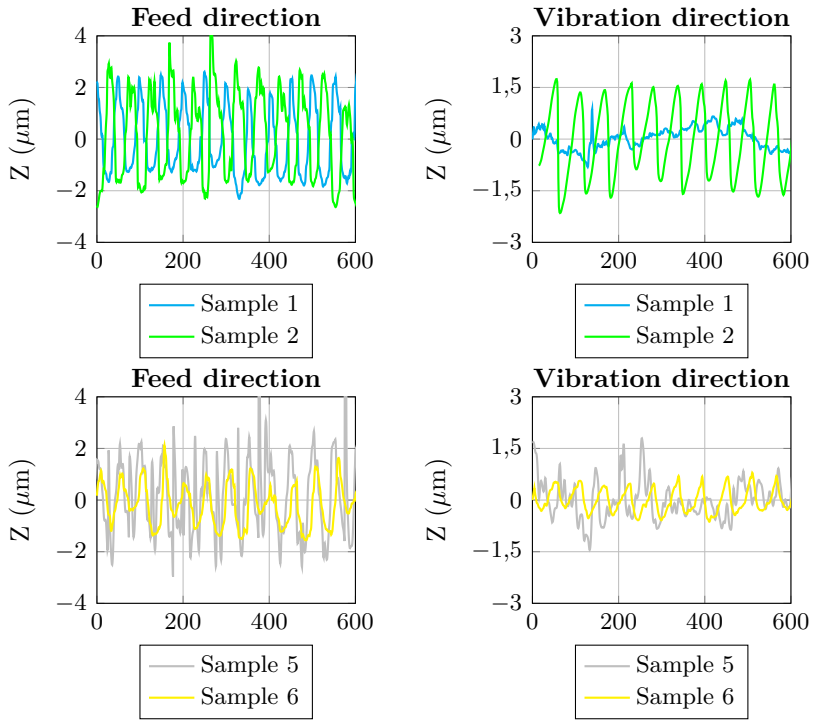

Figure 9.22: 2D profiles along both the feed and vibration as a function of the cutting conditions reported on Table 5.9.

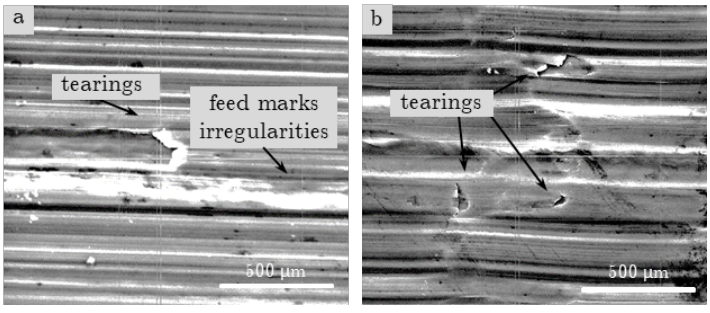

Figure 9.23: Examples of surface defects found after: a) CT (Sample 1) and b) UVT (Sample 2). Cutting conditions are reported on Table 5.9.

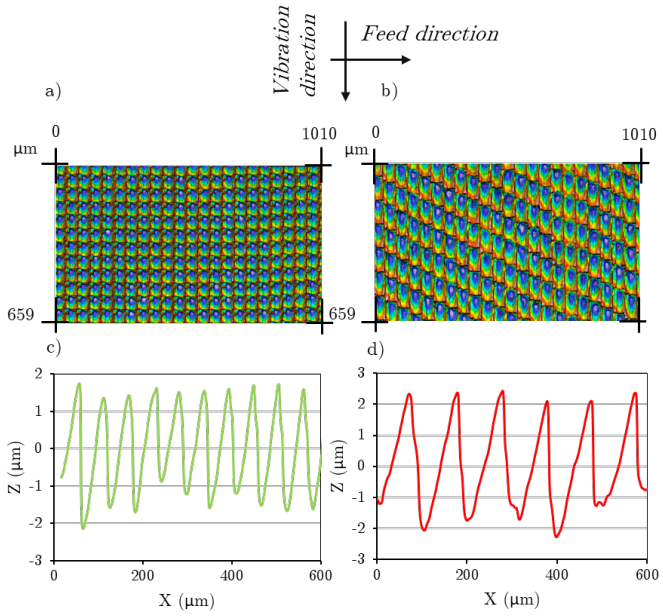

Figure 9.24: (a) Topography of the Sample 2 case; b) topography of the Sample 4 case; c) 2D profile along vibration direction of Sample 2 case; c) 2D profile along vibration direction of Sample 4 case.
Cutting conditions are reported on Table 5.9.

As tearing appears on the surface of samples machined using conventional and ultrasonic approach, it can be stated that this type of defect is not generated by the tool vibration.

Comparison between different UVTed samples

The surface topography of two samples machined using the UVT system at 100 m/min and 200 m/min, respectively, with DoC equal to 0.05 mm, is shown in Fig. 9.24.
It is worth to note that the designed topography in terms of distance between two subsequent gaps was readily obtained. This distance can be expressed through Eq. 9.1:

$$d_{\text{gap}} = \frac{V_c * 10^6}{60f} \tag{9.1}$$

where d_{gap} is expressed in μm, V_c is the cutting speed in m/min, and f the frequency of vibration in Hz.
The texture obtained on the surface is regular and the pattern is repeated periodically (see Fig. 9.24) confirming the direct proportionality between dimples distance and cutting speed, and, therefore, proving that the UVT

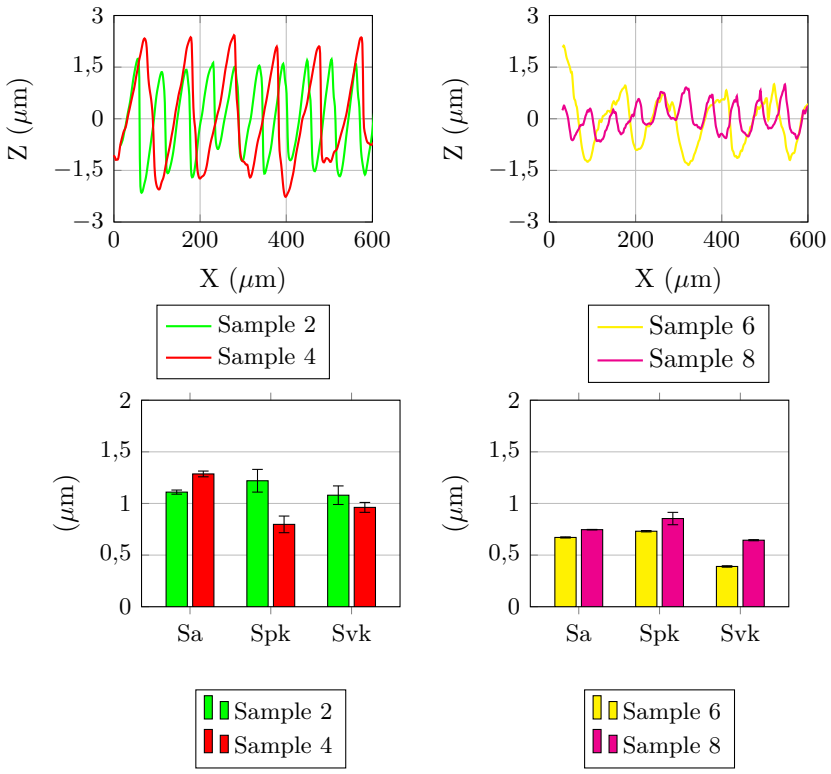

Figure 9.25: 2D profiles and relative main surface roughness parameters as a function of the cutting condition reported on Table 5.9.

system works within its design limits, vibrating the tool along a space-fixed axis with sufficient stiffness.

Fig. 9.25 shows the effects of machining parameters adopted during UVT on the main effective surface texture parameters, while Table 9.9 reports measurements of average peak's aspect ratio.
Increasing the cutting speed from 100 m/min to 200 m/min, the pattern of microstructures become sparser along the vibration direction, as predicted by Eq. 9.1. However, cutting speed does not contribute to modify peaks substantially on both their size and shape. A confirmation of that is that a clear trend of surface roughness cannot be identified, since they have an opposite trend for different depth of cut.
Data reported on table 9.9 confirm that also peaks's aspect ratio does not present a clear trend.
Increasing the cutting speed, peaks' aspect ratio is reduced in the case of DoC of 0.05 mm while, on the contrary, resulted increased in the case of DoC equal to 0.1 mm.
On this basis, it can be concluded that the cutting speed has not a clear

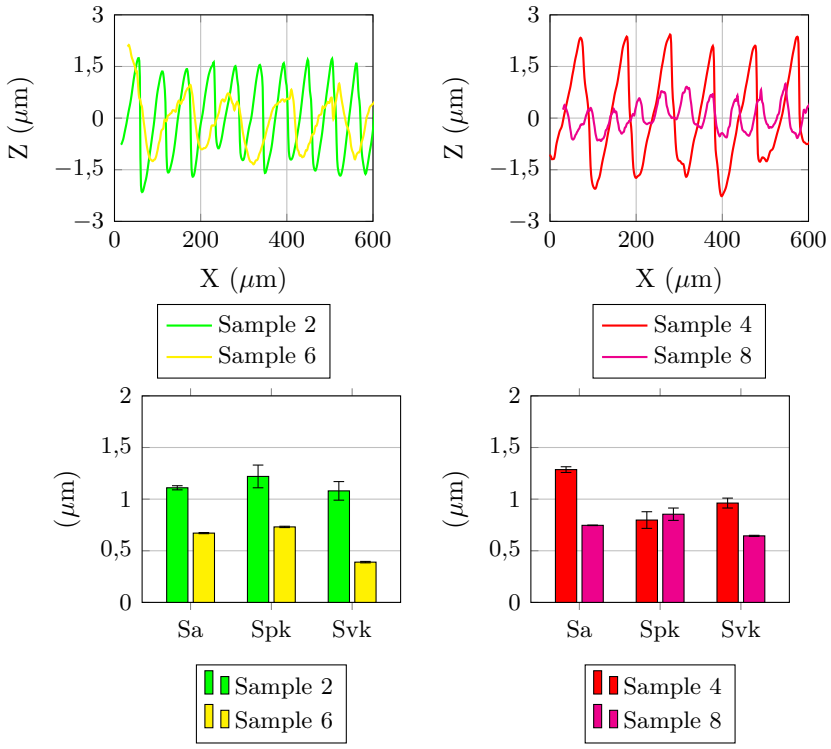

Figure 9.26: 2D profiles and relative main surface roughness parameters as a function of the cutting condition reported on Table 5.9

Table 9.9: Average measurements of depth, length and aspect ratio of the UVT induced dimples as a function of the cutting conditions reported on Table 5.9.

Test ID	Average depth (μm)	Average length (μm)	Aspect ratio
Sample 2	3.1 ± 0.3	55	0.06
Sample 4	4.4 ± 0.2	111	0.04
Sample 6	0.6 ± 0.3	55	0.01
Sample 8	2.1 ± 0.3	111	0.02

influence on the form of peaks and, as a consequence, on the surface roughness parameters.
On the contrary, DoC influences dimple' aspect ratio (Table 9.9) and, as a consequence, roughness parameters to a significant extent.
Figs 9.26 and 9.25 shown these evidences. As the DoC is increased, the aspect ratio of the peaks decrease, namely they become larger and shorter. Sa, Svk and Spk are reduced when DoC is doubled.
Therefore, the depth of cut has an important influence on the arrangement of microstructures along the vibration direction.

9.3.3 Wettability

In this Section, liquid droplet angles results are reported.
First, the influence of CT and UVT on wettability is addressed; then, the effect of UVT process parameters is evaluated.

Comparison between CT and UVT

Water droplet contact angle on the surfaces created by the process of CT (Sample 1) and UVT (Sample 2) are reported on Fig. 9.27. Similar results are found for others cutting conditions and, therefore, are not reported.
As can be seen, UVT contributes to increase wettability (lowering the contact angle). The increment of wettability is of 17% compared to CT surfaces. Top view of droplet confirm that the droplet assumes a more isotropic configuration in the case of UVT surface, covering in a more homogeneus way the surface along the cutting direction. The shape of the water is symmetric along the feed and vibration direction, while in the case of CT is elongated towards the feed direction.
Thus means that UVT contribute to the formation of a more isotropic surface, since tends to remain spherical, not assuming preferential direction [28].
Wettability behaviour mainly depends on two factors: the first factor is the level of surface energy which is dependent on the chemical composition of the surface. Materials with high surface energy create more hydrophilicity (as the surface of these materials needs more energy to break molecular bonds between the surface and the liquid in contact with it) [158].
However, from results reported on Section 9.3, no sensible differences were noticed between the mechanical properties of CT and UVT samples. On this basis, the surface energy would have not been influenced.
The second factor that influence wettability is the roughness and the topography of the surface. The creation of microtextured surfaces can boost both hydrophilicity and hydrophobicity.
In this case, the generation of a pattern along the vibration direction contribute to increase wettability. Such increment cannot be explained by a surface roughness parameters change, since, as demonstrated in section 9.3.2,

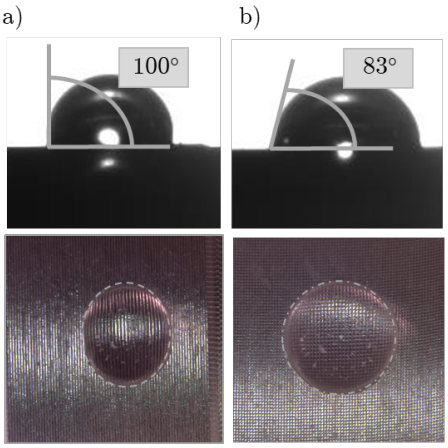

Figure 9.27: Water droplet on the surface machined at: a) CT (Sample 1) and b) UVT (Sample 2). Cutting conditions are reported on Table 5.9.

Table 9.10: Measured contact angles and their standard deviations as a function of the cutting conditions reported on Table 5.9.

Test ID	Sample 2	Sample 4	Sample 6	Sample 8
Contact angle (deg)	83	90	95	83
Standard deviation	2.4	1.8	1.4	1.9

the creation of a regular pattern on the vibration direction is not well described by the roughness parameters taken into consideration in this study. However, in general, the generation of a regular and well determined pattern contribute to increase isotropy and therefore increasing wettability.

Comparison between different UVT samples

Table 9.10 reports contact angle measurements as a function of UVT process parameters.
As can be seen, no clear influence of the cutting speed or DoC on contact angle can be highlighted.
Thus, can be ascribed to the fact that UVT introduces a texture surface perpendicular to the feed direction but, for doing wettability measurements on cylindrical surfaces, samples are measured perpendicular to their axis, and therefore the contribute of UVT texture can be slightly appreciated.

9.3.4 Corrosion behaviour of UVTed samples

The effect of the application of ultrasonic vibration to turning process on the corrosion behaviour is reported in Fig. 9.28 in which the comparison

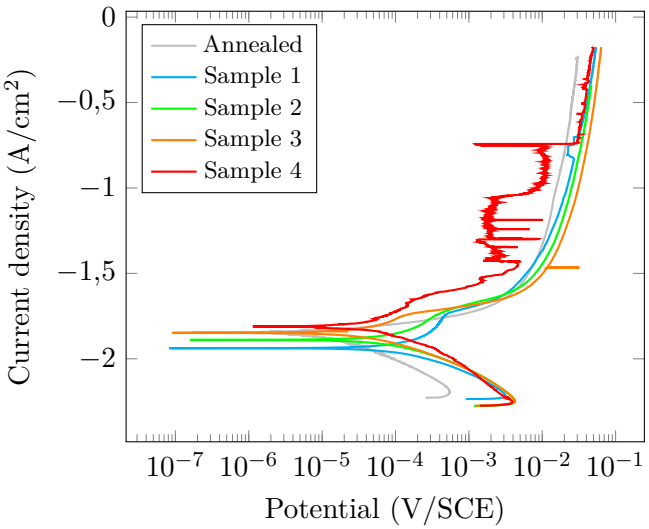

Figure 9.28: Potentiodynamic polarisation curves of UVT-ed samples in SBF solution at 37°C. Cutting conditions are reported on Table 5.9.

Table 9.11: Electrochemical corrosion data of the UVT-ed samples as a function of the cutting conditions reported on Table 5.9.

Test ID	E_{corr} (V/SCE)	I_{corr} (μA/cm^2)
Annealed	-1.84	10
Sample 1	-1.93	5.5
Sample 2	-1.88	6
Sample 3	-1.81	4
Sample 4	-1.88	6

between the main investigated conditions is shown.
Table 9.11 summaries the electrochemical data obtained from Fig. 9.28.
Results shown a slight worsening in corrosion resistance for UVT samples, as demonstrated by the increase into the corrosion current.
Thus can be attributable to both the absence of substantial change into the mechanical properties by the application of the ultrasonic vibration during cutting and to the increased wettability.

9.3.5 Conclusions

Ultrasonic Vivration Turning was exploited to modify the surface texture of the AZ31 magnesium alloy in order to increase its corrosion resistance in human-like environment.

The following conclusions can be drawn:

- The UVT system demonstrated the expected functionality on the basis of the design requirements: the machined surface topography showed a regular pattern reflecting the proper stiffness of the tool and process parameter-independent tool tip trajectory;
- The obtained surface texturing was periodical and the distance between two subsequent dimples could be controlled by varying the vibration frequency, feed and cutting speed.
- UVT sligthly influences the mechanical properties, since the microstructure under the machined surface and the nanohardness do not change with the introduction of vibration;
- UVT is shown to great influence the surface roughness parameters; anyway the way in which they are influenced depends on the other process parameters adopted;
- Among the UVTed surfaces, it was demonstrated that the cutting speed mainly determine the distance between two subsequent peaks, whereas the DoC strictly influences the peaks's aspect ratio. Increasing DoC, peakes become shorter and larger;
- Wettability of UVTed surfaces resulted increased regardless the cutting parameters adopted; thus is attributed to the generation of a pattern perpendicular to the feed direction which enhances the symmetry of the water droplet;
- No subtantial difference among the UVTed samples are found. Thus can be attributed to limit given by the measurement method which allow to measure contact angle only in one direction;
- No substantial improvement on the corrosion resistance is found between CT and UVT sampples. Thus can be ascribed to the absence of drastic change into the mechanical properties together with an enhancement of wettability.

Part V

Conclusions

Chapter 10

Conclusions and future works

In this chapter, the findings and results of the current research are summarized with final remarks and conclusions. The concluding remarks are given in order of appearance in the chapters.
The directions and recommendations of the future work are discussed briefly based on the results and observations presented in this dissertation.

10.0.1 Titanium alloys

In the Ti-APP#1, the influence of the machining parameters and cooling strategies on the wear behavior of theTi6Al4V titanium alloy acetabular cups was investigated.
Wear tests were carried out in reciprocating sliding motion against wrought CoCrMo cylinders in a wet and temperature controlled system.
In the Ti-APP#2, different cooling strategies were applied in machining wrought and additive manufactured Ti6Al4V samples and their influence on the alloys tribocorrosion behaviour was investigated.
Tribocorrosion tests were carried in a wet and temperature-controlled experimental apparatus in which the Ti6Al4V samples were made to slid against zirconia plates in order to reproduce as much as possible the human mouth conditions.
In the Ti-APP#3, prototypes of commercially pure titanium dental implants were machined using different cutting strategies, and were then coated with sphene by spray coating using an automatic airbrush. The strength of the interface between the substrate and the coating was evaluated by means of nano-hardness indentations maps.
Based on the results of this research,the following conclusions can be drawn:

- Results show that cryogenic machining promote the formation of harder and more compressed surfaces. Thus effects is emphasizes by increasing the number of passes used to obtain the final shape. In addition,

cryogenic cooling leads to the formation of rougher surfaces (higher Sa) with lower amount of peaks (lower Ssk) which protrude above the mean line. Results show that the wear volume is conditioned by both the mechanical properties of the subsurface and by the machining induced roughness profile. The lowest wear volume is obtained when machining in cryogenic conditions and with the highest number of passes. In a general sense, it can be stated that a well-finished surface, usually identified by a low Sa value, does not necessarily provide a high wear resistance; on the contrary, it was proved that the Ssk and Svk parameters were better indicators, and can be properly used to qualify the wear characteristics of Ti6Al4V acetabular cups and to effectively design the machining parameters to produce MoM connections characterized by an enhanced wear resistance;

- Cryogenic machining affected the surface properties of the EBM and wrought Ti6Al4V samples, inducing higher micro-hardness, higher compressive residual stresses, lower surface roughness and better corrosion behaviour than dry and wet cutting. As a consequence of these surface integrity improvements, higher values of open circuit potential together with lower values of corrosion current density characterized the cryogenic machined samples. Similarly, the lowest wear volume is achieved in the case of cryogenic condition.
  Therefore, cryogenic cooling appears as the best way to manufacture dental implants with improved functional properties.
  On the contrary, the processing route does not lead to significant improvement into tribo-corrosion behaviour as well as to the wear behaviour.

- The surface characteristics of the machined prototypes greatly influenced the coating-substrate interface behaviour. Even if the coating thickness is not influenced neither by the feed nor by the cooling strategies, the microstructure appears more refined in the latter case. Moreover, cryogenic cooling promotes lower amount of defects on the machining surface compared with traditional cutting fluid, and in similar way, also the cryogenic interfaces resulted characterized by lower density of defects.
  As a consequences, nano-hardness measurements showed that both the hardness and the elastic modulus of the cryogenic machined-coated surfaces were characterized by higher values than that of the same surfaces machined with a conventional cutting fluid.
  On these basis, the use of cryogenic machining in manufacturing the substrate resulted in a better deposition of the coating, since the adhesion to the substrate is improved.

10.0.2 Magnesium alloys

In the Mg-APP#1, the effect of different machining parameters, namely the cooling strategy and feed rate, on the degradation behavior and wettability of the AZ31 magnesium alloy was investigated.
In the Mg-APP#2, LSEM was used to induce surface modifications on AZ61 magnesium alloy workpieces. Different cooling strategies and cutting speeds were applied and their effects on the surface integrity and corrosion resistance were evaluated.
In the Mg-APP#3, UVT was used to modify the surface texture of the AZ31 magnesium alloy in order to change the wettability and therefore, modifying its corrosion resistance in human-like environment.
Based on the results of this research, the following conclusions can be drawn:

- Different cooling conditions, namely dry, wet and cryogenic, were used to machine the biodegradable AZ31 magnesium alloy. Even all the cooling methods led to the formation of a nanostructure near the machined surface, only in the case of cryogenic machining a thicker nonostructure layer together with a compressive residual stress state were obtained.
  The strategy of decreasing the feed rate was used in order to modify the machined surface topography and, as consequences, to reduce the machined surface wettability. A reduction in wettability of 13% was reached when a feed rate was decreased of an order of magnitude.
  Moerover, completely defects free surfaces were obtained only in the case of the lowest feed.
  Potentyodynamic polarization curves and degradation studies over three weeks showed that an improvement in corrosion behaviour was achieved by combining the aforementioned machining strategies. The obtained results demonstrated that a careful choice of the machining process parameters brought important changes in terms of both microstructure and topography that can be exploited to enhance the corrosion resistance of magnesium alloy biomedical devices inside the human body;

- Since cryogenic cooling is promoted as alternative way to substitue conventional lubricating technologies, citocompatibility studies were performed. Results show that magnesium is characterized by excellent biocompatibility and that cryogenic cooling leaves unchanged this importan characteristic;

- LSEM is a suitable way to induce a significant deformation on the machined workpiece surface, which appears in form of a harder and more refined SPD layer compared to the annealed alloy. The presence of such surface-modified region contributes to improve the corrosion

resistance of the alloy, shifting the related corrosion curves towards higher potentials and lower current densities.
The strategy of applying liquid nitrogen showed potentialities to obtain a surface with enhanced mechanical and corrosion characteristics. In fact, the cryogenic-machined surfaces were characterized by a greater grain refinement and slightly more extended SPD layer compared to the corresponding dry cases. In addition, harder surfaces were observed when liquid nitrogen was applied. Also the corrosion properties were positively influenced, as the characteristic plateau of the corresponding dry curves, indicative of a lower corrosion resistance, was not detected.
In general, higher cutting speeds led to the formation of a thicker UFG region in the LSEMed samples. On the other hand, lower cutting speeds generally promoted harder surfaces. However, a clear effect of the cutting speed on the corrosion behavior was not found.
From the obtained results, it can be stated that, regardless the adopted cutting speed, cryogenic cooling can be effectively applied to enhance the surface integrity and corrosion resistance of the AZ61 magnesium alloy processed under LSEM;

- Chip formation during LSEM is facilitated by the increase of temperature generated by the localized deformation process; therefore the application of liquid nitrogen reduces the formabillity of the chip inducing the presence of defects compared to dry condition, especially at the lowest cutting speed.
  Corrosion curves indicate an reduction of corrosion current density for chips obtained in dry condition compared to the annealed starting alloy, thanks to the refinement of the grain.
  Therefore, dry LSEM remais the best method to easily create a continous chip without defects;

- Micro-textured surfaces were fabricated successfully through experimental tests of the UVT. Both cutting speed and depth of cut play an important role in influencing the patterns and shapes of microstructures. With the increasing of spindle speed, the distance between adjacent dimples along cutting direction decreases. On the contrary, increasing the depth of cut contributes to decrease the aspect ratio of the generated patterns. Therefore, shape and distance of microdimples are dependent from machining parameters used.
  According to wetting tests, the experimental textured surfaces present different wetting properties, which provides a foundation for further application. An increase in hydrophily was obtained by UVT, regardless the cutting parameters. As a consequences, the corrosion resistance is not improved compared to conventional turned surfaces.

UVT is proved to be a relatively simple and effective way to fabricate micro-textured surfaces. Unfortunately, since no improvements in corrosion reistance were obtained is not suitable to improve functional performances of magnesium alloys.

10.1 Future research directions

10.1.1 Titanium alloys

- To validate the results of the in-vitro wear testing, the optimized process parameters found in this research work will be applied to machine real biomedical implants, namely acetabular cups and dental prosthesis, and then they will be tested in an in vitro experimental apparatus;

- The biological reactions to wear debris, generated as a consequences of the sliding of bearing surfaces, have been shown to result in osteolysis and loosening of total hip arthroplasties. In addition to local responses, metal debris may spread over the whole body via systemic circulation (i.e., lymph and blood).
  Wear debris particles are detrimental for human health because they have a unique morphology in terms of shape and size, and surface topography in terms of roughness and texture. These characteristics are derived from the deterioration process or wear mode by which they were produced, therefore, they are strictly connected to the state of the surface.
  With this in mind, wear studies can be used to assess how process parameters, especially cryogenic cooling, affected the morphology of the wear debris generated.

10.1.2 Magnesium alloys

- Biomedical implants are simultaneously subjected to cyclic load and corrosive environment, leading to corrosion assisted cracking phenomena and corrosion fatigue; therefore, the optimized machining parameters found in this research work, will be tested to these corrosion assisted cracking phenomena and, then, compared to conventionally machined alloy.
  It is worth to note that the experimental apparatus is already designed and partial results are already achieved;

- Micro-machining or micro-forming processes can be apply to the chips obtained by LSEM to manufacture small-scale components with enhanced structural performance.
  Dissolvable surgical clips and wrapped cylinders are examples of small biomedical magnesium implants devices that can be manufactured by

the combined techniques of LSEM and micro-machining.
Future studies will focus on the generation of a completely defects-fee chips as semifinished products for the manufacture of small biomedical devices.

- The unique micro texture, composed by subsequent dimples, generated by UVT can be exploited as a potential way to realize a surface that can be more easily coated.

References

[1] A Ginting and M Nouari. "Surface integrity of dry machined titanium alloys". In: *International Journal of Machine Tools and Manufacture* 49.3-4 (2009), pp. 325–332.

[2] Durul Ulutan and Tugrul Ozel. "Machining induced surface integrity in titanium and nickel alloys: A review". In: *International Journal of Machine Tools and Manufacture* 51.3 (2011), pp. 250–280.

[3] ARC Sharman, JI Hughes, and K Ridgway. "Workpiece surface integrity and tool life issues when turning Inconel 718 nickel based superalloy". In: *Machining Science and Technology* 8.3 (2004), pp. 399–414.

[4] CH Che-Haron and A Jawaid. "The effect of machining on surface integrity of titanium alloy Ti–6% Al–4% V". In: *Journal of materials processing technology* 166.2 (2005), pp. 188–192.

[5] CH Che-Haron. "Tool life and surface integrity in turning titanium alloy". In: *Journal of Materials Processing Technology* 118.1-3 (2001), pp. 231–237.

[6] YB Guo, W Li, and IS Jawahir. "Surface integrity characterization and prediction in machining of hardened and difficult-to-machine alloys: a state-of-art research review and analysis". In: *Machining Science and Technology* 13.4 (2009), pp. 437–470.

[7] AB Sadat and JA Bailey. "Residual stresses in turned AISI 4340 steel". In: *Experimental Mechanics* 27.1 (1987), pp. 80–85.

[8] R Msaoubi et al. "Residual stress analysis in orthogonal machining of standard and resulfurized AISI 316L steels". In: *Journal of materials processing technology* 96.1-3 (1999), pp. 225–233.

[9] SM Darwish. "The impact of the tool material and the cutting parameters on surface roughness of supermet 718 nickel superalloy". In: *Journal of Materials Processing Technology* 97.1-3 (2000), pp. 10–18.

[10] AKM Nurul Amin, Ahmad F Ismail, and MK Nor Khairusshima. "Effectiveness of uncoated WC–Co and PCD inserts in end milling of titanium alloyTi–6Al–4V". In: *Journal of Materials Processing Technology* 192 (2007), pp. 147–158.

[11] G Rotella et al. "The effects of cooling conditions on surface integrity in machining of Ti6Al4V alloy". In: *The International Journal of Advanced Manufacturing Technology* 71.1-4 (2014), pp. 47–55.

[12] Domenico Umbrello, Fabrizio Micari, and IS Jawahir. "The effects of cryogenic cooling on surface integrity in hard machining: A comparison with dry machining". In: *CIRP Annals-Manufacturing Technology* 61.1 (2012), pp. 103–106.

[13] Florian Ambrosy et al. "An experimental study of cryogenic machining on nanocrystalline surface layer generation". In: *Procedia CIRP* 13 (2014), pp. 169–174.

[14] Fritz Klocke et al. "High performance cutting of gamma titanium aluminides: Influence of lubricoolant strategy on tool wear and surface integrity". In: *Wear* 302.1-2 (2013), pp. 1136–1144.

[15] Zi-He He, Xiao-Ming Zhang, and Han Ding. "Comparison of residual stresses in cryogenic and dry machining of Inconel 718". In: *Procedia CIRP* 46 (2016), pp. 19–22.

[16] Jose Carlos Outeiro, António Castanhola Batista, and Maria Jose Marques. "Residual stresses induced by dry and cryogenic cooling during machining of AZ31B magnesium alloy". In: *Advanced Materials Research*. Vol. 996. Trans Tech Publ. 2014, pp. 658–663.

[17] Franci Pusavec et al. "Residual Stresses, Plastic Work, and Microhardness in Cryogenic Machining of Inconel 718". In: *The 4th International Swedish Production Symposium. Lund, Sweden. 3rd–5th of May 2011*. Swedish Production Academy. 2011, pp. 283–288.

[18] IS Jawahir et al. "Cryogenic manufacturing processes". In: *CIRP annals* 65.2 (2016), pp. 713–736.

[19] Ranajit Ghosh, Zbigniew Zurecki, and John H Frey. "Cryogenic machining with brittle tools and effects on tool life". In: *ASME 2003 International Mechanical Engineering Congress and Exposition*. American Society of Mechanical Engineers. 2003, pp. 201–209.

[20] W Grzesik and K Żak. "Producing high quality hardened parts using sequential hard turning and ball burnishing operations". In: *Precision Engineering* 37.4 (2013), pp. 849–855.

[21] Mert Efe et al. "Mechanics of large strain extrusion machining and application to deformation processing of magnesium alloys". In: *Acta Materialia* 60.5 (2012), pp. 2031–2042.

[22] R Calistes et al. “Controlling gradation of surface strains and nanostructuring by large-strain machining”. In: *Scripta Materialia* 60.1 (2009), pp. 17–20.

[23] D Sagapuram et al. “Enabling shear textures and fine-grained structures in Magnesium sheet by machining-based deformation processing”. In: *IOP Conference Series: Materials Science and Engineering*. Vol. 63. 1. IOP Publishing. 2014, p. 012155.

[24] Yao Liu et al. “Enhancing surface integrity by high-speed extrusion machining”. In: *The International Journal of Advanced Manufacturing Technology* 89.5-8 (2017), pp. 2141–2150.

[25] Vadim V Silberschmidt et al. “Surface-roughness improvement in ultrasonically assisted turning”. In: *Procedia CIRP* 13 (2014), pp. 49–54.

[26] N Ahmed et al. “Analysis of material response to ultrasonic vibration loading in turning Inconel 718”. In: *Materials Science and Engineering: A* 424.1-2 (2006), pp. 318–325.

[27] Chandra Nath and M Rahman. “Effect of machining parameters in ultrasonic vibration cutting”. In: *International Journal of Machine Tools and Manufacture* 48.9 (2008), pp. 965–974.

[28] Ping Guo et al. “Generation of hierarchical micro-structures for anisotropic wetting by elliptical vibration cutting”. In: *CIRP Annals-Manufacturing Technology* 63.1 (2014), pp. 553–556.

[29] Xianfu Liu, Debao Wu, and Jianhua Zhang. “Fabrication of micro-textured surface using feed-direction ultrasonic vibration-assisted turning”. In: *The International Journal of Advanced Manufacturing Technology* (2018), pp. 1–9.

[30] Yong Lu et al. “Experimental studies of wettability control on cylindrical surfaces by elliptical vibration texturing”. In: *The International Journal of Advanced Manufacturing Technology* 76.9-12 (2015), pp. 1807–1817.

[31] S Amini, H Nouri Hosseinabadi, and SA Sajjady. “Experimental study on effect of micro textured surfaces generated by ultrasonic vibration assisted face turning on friction and wear performance”. In: *Applied Surface Science* 390 (2016), pp. 633–648.

[32] U Sudeep, RK Pandey, and N Tandon. “Effects of surface texturing on friction and vibration behaviors of sliding lubricated concentrated point contacts under linear reciprocating motion”. In: *Tribology International* 62 (2013), pp. 198–207.

[33] A Molinari et al. “Dry sliding wear mechanisms of the Ti6Al4V alloy”. In: *Wear* 208.1-2 (1997), pp. 105–112.

[34] G Straffelini and A Molinari. “Dry sliding wear of Ti–6Al–4V alloy as influenced by the counterface and sliding conditions”. In: *Wear* 236.1-2 (1999), pp. 328–338.

[35] F Borgioli et al. “Improvement of wear resistance of Ti–6Al–4V alloy by means of thermal oxidation”. In: *Materials Letters* 59.17 (2005), pp. 2159–2162.

[36] BKC Ganesh et al. “Effect of shotpeening on sliding wear and tensile behavior of titanium implant alloys”. In: *Materials & Design (1980-2015)* 56 (2014), pp. 480–486.

[37] PH Morton and T Bell. “Surface engineering of titanium”. In: *Sixth World Conference on Titanium. IV*. 1988, pp. 1705–1712.

[38] Che Chengwei et al. “Influence of rapidly solidified structures on wear behavior of Ti-6AI-4V laser alloyed with TiC”. In: *Tribology transactions* 38.4 (1995), pp. 875–878.

[39] S Anand Kumar et al. “Influence of Surface Mechanical Attrition Treatment on Fretting Wear Behaviour of Ti-6Al-4V”. In: *Advanced Materials Research*. Vol. 463. Trans Tech Publ. 2012, pp. 316–320.

[40] V Fridrici, S Fouvry, and Ph Kapsa. “Effect of shot peening on the fretting wear of Ti–6Al–4V”. In: *Wear* 250.1-12 (2001), pp. 642–649.

[41] Shitu Jindal et al. “Enhanced osteoblast proliferation and corrosion resistance of commercially pure titanium through surface nanostructuring by ultrasonic shot peening and stress relieving”. In: *Journal of Oral Implantology* 40.S1 (2014), pp. 347–355.

[42] Kevin K Liu and Michael R Hill. “The effects of laser peening and shot peening on fretting fatigue in Ti–6Al–4V coupons”. In: *Tribology International* 42.9 (2009), pp. 1250–1262.

[43] Mehdi Kheradmandfard et al. “Significant improvement in cell adhesion and wear resistance of biomedical β-type titanium alloy through ultrasonic nanocrystal surface modification”. In: *Journal of Alloys and Compounds* 762 (2018), pp. 941–949.

[44] S Affatato et al. “The predictive power of surface profile parameters on the amount of wear measured in vitro on metal-on-polyethylene artificial hip joints”. In: *Proceedings of the Institution of Mechanical Engineers, Part H: Journal of Engineering in Medicine* 220.3 (2006), pp. 457–464.

[45] Anke Turger et al. “Manufacturing conditioned roughness and wear of biomedical oxide ceramics for all-ceramic knee implants”. In: *Biomedical engineering online* 12.1 (2013), p. 84.

[46] Robert K Whittaker et al. "Variation in taper surface roughness for a single design effects the wear rate in total hip arthroplasty". In: *Journal of Orthopaedic Research* 35.8 (2017), pp. 1784–1792.

[47] YF Zheng, XN Gu, and F Witte. "Biodegradable metals". In: *Materials Science and Engineering: R: Reports* 77 (2014), pp. 1–34.

[48] RK Singh Raman, Sajjad Jafari, and Shervin Eslami Harandi. "Corrosion fatigue fracture of magnesium alloys in bioimplant applications: A review". In: *Engineering fracture mechanics* 137 (2015), pp. 97–108.

[49] P Gunde et al. "High-strength magnesium alloys for degradable implant applications". In: *Materials Science and Engineering: A* 528.3 (2011), pp. 1047–1054.

[50] H Hornberger, S Virtanen, and AR Boccaccini. "Biomedical coatings on magnesium alloys–a review". In: *Acta biomaterialia* 8.7 (2012), pp. 2442–2455.

[51] D Ahmadkhaniha et al. "Corrosion behavior of severely plastic deformed magnesium based alloys: A review". In: *Surface Engineering and Applied Electrochemistry* 53.5 (2017), pp. 439–448.

[52] N Saikrishna et al. "Influence of bimodal grain size distribution on the corrosion behavior of friction stir processed biodegradable AZ31 magnesium alloy". In: *Journal of magnesium and alloys* 4.1 (2016), pp. 68–76.

[53] YH Jang et al. "Corrosion behaviour of friction stir welded AZ31B Mg in 3· 5% NaCl solution". In: *Corrosion engineering, science and technology* 42.2 (2007), pp. 119–122.

[54] Z Pu et al. "Grain refined and basal textured surface produced by burnishing for improved corrosion performance of AZ31B Mg alloy". In: *Corrosion Science* 57 (2012), pp. 192–201.

[55] Z Pu et al. "Enhanced surface integrity of AZ31B Mg alloy by cryogenic machining towards improved functional performance of machined components". In: *International journal of machine tools and manufacture* 56 (2012), pp. 17–27.

[56] S Dinesh et al. "Effect of cryogenic cooling on machinability and surface quality of bio-degradable ZK60 Mg alloy". In: *Materials & design* 87 (2015), pp. 1030–1036.

[57] B Ratna Sunil et al. "In vitro and in vivo studies of biodegradable fine grained AZ31 magnesium alloy produced by equal channel angular pressing". In: *Materials Science and Engineering: C* 59 (2016), pp. 356–367.

[58] Hao Wang et al. "The effect of pre-processing and grain structure on the bio-corrosion and fatigue resistance of magnesium alloy AZ31". In: *Advanced Engineering Materials* 9.11 (2007), pp. 967–972.

[59] G Ben Hamu, D Eliezer, and L Wagner. "The relation between severe plastic deformation microstructure and corrosion behavior of AZ31 magnesium alloy". In: *Journal of alloys and compounds* 468.1-2 (2009), pp. 222–229.

[60] B Denkena and A Lucas. "Biocompatible magnesium alloys as absorbable implant materials–adjusted surface and subsurface properties by machining processes". In: *CIRP Annals-Manufacturing Technology* 56.1 (2007), pp. 113–116.

[61] Yuebin Guo, Michael P Sealy, and Changsheng Guo. "Significant improvement of corrosion resistance of biodegradable metallic implants processed by laser shock peening". In: *CIRP Annals-Manufacturing Technology* 61.1 (2012), pp. 583–586.

[62] Renlong Xin et al. "Influence of texture on corrosion rate of AZ31 Mg alloy in 3.5 wt.% NaCl". In: *Materials & design* 32.8-9 (2011), pp. 4548–4552.

[63] Guang-Ling Song, Raja Mishra, and ZhenQing Xu. "Crystallographic orientation and electrochemical activity of AZ31 Mg alloy". In: *Electrochemistry Communications* 12.8 (2010), pp. 1009–1012.

[64] Guang-Ling Song and Zhenqing Xu. "Crystal orientation and electrochemical corrosion of polycrystalline Mg". In: *Corrosion Science* 63 (2012), pp. 100–112.

[65] R Walter and M Bobby Kannan. "Influence of surface roughness on the corrosion behaviour of magnesium alloy". In: *Materials & Design* 32.4 (2011), pp. 2350–2354.

[66] TL Nguyen et al. "On the role of surface roughness in the corrosion of pure magnesium in vitro". In: *Journal of Biomedical Materials Research Part B: Applied Biomaterials* 100.5 (2012), pp. 1310–1318.

[67] Göran Garellick et al. "Swedish Hip Arthroplasty Register: Annual Report, 2008". In: *Department of Orthopaedics, Sahlgrenska University Hospital* (2009).

[68] B Valdez and M Schorr. "Handbook of Materials for Medical Devices". In: *Corrosion* 61.8 (2005), p. 832.

[69] Hamid Reza Seyyed Hosseinzadeh, Alireza Eajazi, and Ali Sina Shahi. "The bearing surfaces in total hip arthroplasty–options, material characteristics and selection". In: *Recent advances in arthroplasty*. InTech, 2012.

[70] Aikaterini Tsaousi. "The Genotoxic Potential of Novel Materials Used in Modern Hip Replacements for Young Patients". In: *Orthopedic Surgery*. InTech, 2012.

[71] R Dattani. "Femoral osteolysis following total hip replacement". In: *Postgraduate medical journal* 83.979 (2007), pp. 312–316.

[72] Garima Bhardwaj and Thomas J Webster. "Reduced bacterial growth and increased osteoblast proliferation on titanium with a nanophase TiO2 surface treatment". In: *International journal of nanomedicine* 12 (2017), p. 363.

[73] Andrea Mombelli and Lakshman P Samaranayake. "Topical and systemic antibiotics in the management of periodontal diseases". In: *International dental journal* 54.1 (2004), pp. 3–14.

[74] Stefan Renvert and G Rutger Persson. "Periodontitis as a potential risk factor for peri-implantitis". In: *Journal of clinical periodontology* 36 (2009), pp. 9–14.

[75] Maria Beatriz Maximo et al. "Short-term clinical and microbiological evaluations of peri-implant diseases before and after mechanical anti-infective therapies". In: *Clinical Oral Implants Research* 20.1 (2009), pp. 99–108.

[76] HV Cruz et al. "Tribocorrosion and bio-tribocorrosion in the oral environment: the case of dental implants". In: *Biomedical tribology* (2011), pp. 1–33.

[77] Siegfried Martin Heckmann et al. "Stress and inflammation as a detrimental combination for peri-implant bone loss". In: *Journal of dental research* 85.8 (2006), pp. 711–716.

[78] Ameen Khraisat et al. "Stability of the implant/abutment joint in a single-tooth external-hexagon implant system: clinical and mechanical review". In: *Clinical implant dentistry and related research* 6.4 (2004), pp. 222–229.

[79] Marianthi G Manda et al. "Observations on an in-vivo failure of a titanium dental implant/abutment screw system: a case report". In: *Journal of Biomedical Materials Research Part B: Applied Biomaterials: An Official Journal of The Society for Biomaterials, The Japanese Society for Biomaterials, and The Australian Society for Biomaterials and the Korean Society for Biomaterials* 89.1 (2009), pp. 264–273.

[80] FH Jones. "Teeth and bones: applications of surface science to dental materials and related biomaterials". In: *Surface Science Reports* 42.3-5 (2001), pp. 75–205.

[81] Lina Engelen et al. “The effect of saliva composition on texture perception of semi-solids”. In: *Archives of Oral Biology* 52.6 (2007), pp. 518–525.

[82] Rama Bansil, Eugene Stanley, and J Thomas LaMont. “Mucin biophysics”. In: *Annual Review of Physiology* 57.1 (1995), pp. 635–657.

[83] Stefano Mischler. “Triboelectrochemical techniques and interpretation methods in tribocorrosion: a comparative evaluation”. In: *Tribology International* 41.7 (2008), pp. 573–583.

[84] SC Ferreira et al. “Tribocorrosion behaviour of ZrOxNy thin films for decorative applications”. In: *Surface and Coatings Technology* 200.22-23 (2006), pp. 6634–6639.

[85] MT Mathew et al. “Significance of tribocorrosion in biomedical applications: overview and current status”. In: *Advances in tribology* 2009 (2009).

[86] Ana C Fernandes et al. “Tribocorrosion behaviour of plasma nitrided and plasma nitrided+ oxidised Ti6Al4V alloy”. In: *Surface and Coatings Technology* 200.22-23 (2006), pp. 6218–6224.

[87] Manfred F Maitz. “Applications of synthetic polymers in clinical medicine”. In: *Biosurface and Biotribology* 1.3 (2015), pp. 161–176.

[88] S Ramakrishna et al. “Biomedical applications of polymer-composite materials: a review”. In: *Composites science and technology* 61.9 (2001), pp. 1189–1224.

[89] Anja C Hänzi, Alla S Sologubenko, and Peter J Uggowitzer. “Design strategy for new biodegradable Mg–Y–Zn alloys for medical applications”. In: *International journal of materials research* 100.8 (2009), pp. 1127–1136.

[90] Mark P Staiger et al. “Magnesium and its alloys as orthopedic biomaterials: a review”. In: *Biomaterials* 27.9 (2006), pp. 1728–1734.

[91] Mirco Peron, Jan Torgersen, and Filippo Berto. “Mg and its alloys for biomedical applications: exploring corrosion and its interplay with mechanical failure”. In: *Metals* 7.7 (2017), p. 252.

[92] Charles Z Deng et al. “Magnesium alloys for bioabsorbable stents: a feasibility assessment”. In: *Magnesium technology 2011*. Springer, 2011, pp. 413–418.

[93] Christian Plaass et al. “Bioabsorbable magnesium versus standard titanium compression screws for fixation of distal metatarsal osteotomies–3 year results of a randomized clinical trial”. In: *Journal of Orthopaedic Science* 23.2 (2018), pp. 321–327.

[94] Frank Witte et al. "In vivo corrosion of four magnesium alloys and the associated bone response". In: *Biomaterials* 26.17 (2005), pp. 3557–3563.

[95] Colleen Bettles and Matthew Barnett. *Advances in wrought magnesium alloys: fundamentals of processing, properties and applications*. Elsevier, 2012.

[96] K Gusieva et al. "Corrosion of magnesium alloys: the role of alloying". In: *International Materials Reviews* 60.3 (2015), pp. 169–194.

[97] M Esmaily et al. "Fundamentals and advances in magnesium alloy corrosion". In: *Progress in Materials Science* 89 (2017), pp. 92–193.

[98] Wolf-Dieter Mueller. "Electrochemical techniques for assessment of corrosion behaviour of Mg and Mg-alloys". In: *BioNanoMaterials* 16.1 (2015), pp. 31–39.

[99] Guangling Song, Andrej Atrens, and David StJohn. "An Hydrogen Evolution Method for the Estimation of the Corrosion Rate of Magnesium Alloys". In: *Essential Readings in Magnesium Technology*. Springer, 2016, pp. 565–572.

[100] KV Rybalka. "Determination of metal corrosion rate using the pH-metry by the method of compensating additives". In: *Russian Journal of Electrochemistry* 50.5 (2014), pp. 500–502.

[101] Milton Clayton Shaw and JO Cookson. *Metal cutting principles*. Clarendon press Oxford, 1984.

[102] Travis L Brown et al. "A study of the interactive effects of strain, strain rate and temperature in severe plastic deformation of copper". In: *Acta Materialia* 57.18 (2009), pp. 5491–5500.

[103] C Saldana et al. "Micro-scale components from high-strength nanostructured alloys". In: *Materials Science and Engineering: A* 503.1-2 (2009), pp. 172–175.

[104] Srinivasan Swaminathan et al. "Large strain deformation and ultrafine grained materials by machining". In: *Materials Science and Engineering: A* 410 (2005), pp. 358–363.

[105] E Moreno et al. "Design and construction of a bolt-clamped Langevin transducer". In: *Electrical and Electronics Engineering, 2005 2nd International Conference on*. IEEE. 2005, pp. 393–395.

[106] Milan Naď. "Ultrasonic horn design for ultrasonic machining technologies". In: (2010).

[107] DM Razak et al. "A new approach using palm olein, palm kernel oil, and palm fatty acid distillate as alternative biolubricants: improving tribology in metal-on-metal contact". In: *Tribology Transactions* 58.3 (2015), pp. 511–517.

[108] S Williams et al. "In vitro analysis of the wear, wear debris and biological activity of surface-engineered coatings for use in metal-on-metal total hip replacements". In: *Proceedings of the Institution of Mechanical Engineers, Part H: Journal of Engineering in Medicine* 217.3 (2003), pp. 155–163.

[109] Yu Yan, Anne Neville, and Duncan Dowson. "Biotribocorrosion of CoCrMo orthopaedic implant materialsassessing the formation and effect of the biofilm". In: *Tribology international* 40.10-12 (2007), pp. 1492–1499.

[110] Nadine Freifrau von Maltzahn, Jan Holstermann, and Philipp Kohorst. "Retention Forces between Titanium and Zirconia Components of Two-Part Implant Abutments with Different Techniques of Surface Modification". In: *Clinical implant dentistry and related research* 18.4 (2016), pp. 735–744.

[111] Rachele Bertolini et al. "Fretting Corrosion Behavior of Additive Manufactured and Cryogenic-Machined Ti6Al4V for Biomedical Applications". In: *Advanced Engineering Materials* 19.6 (2017), p. 1500629.

[112] R M'Saoubi et al. "A review of surface integrity in machining and its impact on functional performance and life of machined products". In: *International Journal of Sustainable Manufacturing* 1.1-2 (2008), pp. 203–236.

[113] IS Jawahir et al. "Surface integrity in material removal processes: Recent advances". In: *CIRP Annals-Manufacturing Technology* 60.2 (2011), pp. 603–626.

[114] Philip J Withers and HKDH Bhadeshia. "Residual stress. Part 1–measurement techniques". In: *Materials science and Technology* 17.4 (2001), pp. 355–365.

[115] Alistair PD Elfick et al. "The influence of femoral head surface roughness on the wear of ultrahigh molecular weight polyethylene sockets in cementless total hip replacement". In: *Journal of Biomedical Materials Research: An Official Journal of The Society for Biomaterials, The Japanese Society for Biomaterials, and The Australian Society for Biomaterials and the Korean Society for Biomaterials* 48.5 (1999), pp. 712–718.

[116] Leonardo De Chiffre et al. "Quantitative characterisation of surface texture". In: *CIRP Annals-Manufacturing Technology* 49.2 (2000), pp. 635–652.

[117] David J Whitehouse. *Surfaces and their Measurement*. Elsevier, 2004.

[118] Ken J Stout and Liam Blunt. *Three dimensional surface topography*. Elsevier, 2000.

[119] Kenneth Langstreth Johnson and Kenneth Langstreth Johnson. *Contact mechanics*. Cambridge university press, 1987.

[120] Nicholas LeCain. "Tutorial of Hertzian Contact Stress Analysis". In: *College of Optical Sciences, University of Arizona, Tucson, pp-1 to* 6.3 (2011).

[121] Eriberto Bressan et al. "Experimental and computational investigation of Morse taper conometric system reliability for the definition of fixed connections between dental implants and prostheses". In: *Proceedings of the Institution of Mechanical Engineers, Part H: Journal of Engineering in Medicine* 228.7 (2014), pp. 674–681.

[122] Lisa Biasetto and Hamada Elsayed. "Sphene silicate ceramic coatings on cpTi substrates: Process upgrade". In: *Surface and Coatings Technology* 321 (2017), pp. 416–424.

[123] D Umbrello et al. "3D finite element modelling of surface modification in dry and cryogenic machining of EBM Ti6Al4V alloy". In: *CIRP Journal of Manufacturing Science and Technology* 18 (2017), pp. 92–100.

[124] J Caudill et al. "Enhancing the surface integrity of Ti-6Al-4V alloy through cryogenic burnishing". In: *Procedia CIRP* 13 (2014), pp. 243–248.

[125] SS Al-Bermani et al. "The origin of microstructural diversity, texture, and mechanical properties in electron beam melted Ti-6Al-4V". In: *Metallurgical and materials transactions a* 41.13 (2010), pp. 3422–3434.

[126] F Pusavec et al. "Surface integrity in cryogenic machining of nickel based alloyInconel 718". In: *Journal of Materials Processing Technology* 211.4 (2011), pp. 773–783.

[127] M Biček et al. "Cryogenic machining as an alternative turning process of normalized and hardened AISI 52100 bearing steel". In: *Journal of Materials Processing Technology* 212.12 (2012), pp. 2609–2618.

[128] M Dhananchezian and M Pradeep Kumar. "Cryogenic turning of the Ti–6Al–4V alloy with modified cutting tool inserts". In: *Cryogenics* 51.1 (2011), pp. 34–40.

[129] A Bordin et al. "Analysis of tool wear in cryogenic machining of additive manufactured Ti6Al4V alloy". In: *Wear* 328 (2015), pp. 89–99.

[130] W Grzesik et al. "Effects of cryogenic cooling on surface layer characteristics produced by hard turning". In: *Archives of Materials Science* 6 (2012), p. 6.

[131] A Bordin et al. “Feasibility of Cryogenic Cooling in Finishing Turning of Acetabular Cups Made of Additive Manufactured Ti6Al4 V”. In: *Procedia CIRP* 46 (2016), pp. 615–618.

[132] JeFoa Archard. “Contact and rubbing of flat surfaces”. In: *Journal of applied physics* 24.8 (1953), pp. 981–988.

[133] Kwai S Chan. “Roles of microstructure in fatigue crack initiation”. In: *International Journal of Fatigue* 32.9 (2010), pp. 1428–1447.

[134] Iwona Wstawska and Krzysztof Ślimak. “The influence of cooling techniques on cutting forces and surface roughness during cryogenic machining of titanium alloys”. In: *Archives of Mechanical Technology and Materials* 36.1 (2016), pp. 12–17.

[135] Osamu Takakuwa and Hitoshi Soyama. “Effect of residual stress on the corrosion behavior of austenitic stainless steel”. In: *Adv. Chem. Eng. Sci* 5 (2015), pp. 62–71.

[136] Yi Wan et al. “Stress influence on corrosion resistance of aluminum alloy surface”. In: *Advanced Materials Research*. Vol. 1017. Trans Tech Publ. 2014, pp. 287–291.

[137] MARIE-PIERRE Licausi, A Igual Muñoz, and V Amigó Borrás. “Influence of the fabrication process and fluoride content on the tribocorrosion behaviour of Ti6Al4V biomedical alloy in artificial saliva”. In: *Journal of the mechanical behavior of biomedical materials* 20 (2013), pp. 137–148.

[138] A Bazzoni, S Mischler, and N Espallargas. “Tribocorrosion of pulsed plasma-nitrided CoCrMo implant alloy”. In: *Tribology Letters* 49.1 (2013), pp. 157–167.

[139] S Bruschi et al. “Influence of the machining parameters and cooling strategies on the wear behavior of wrought and additive manufactured Ti6Al4V for biomedical applications”. In: *Tribology International* 102 (2016), pp. 133–142.

[140] RA Buchanan, ED Rigney Jr, and JM Williams. “Wear-accelerated corrosion of Ti-6Al-4V and nitrogen-ion-implanted Ti-6Al-4V: Mechanisms and influence of fixed-stress magnitude”. In: *Journal of biomedical materials research* 21.3 (1987), pp. 367–377.

[141] S Sartori, A Ghiotti, and S Bruschi. “Temperature effects on the Ti6Al4V machinability using cooled gaseous nitrogen in semi-finishing turning”. In: *Journal of Manufacturing Processes* 30 (2017), pp. 187–194.

[142] Emmanuel O Ezugwu et al. “Surface integrity of finished turned Ti–6Al–4V alloy with PCD tools using conventional and high pressure coolant supplies”. In: *International Journal of Machine Tools and Manufacture* 47.6 (2007), pp. 884–891.

[143] Xiong Ma et al. “The kinetics of dynamic globularization during hot working of a two phase titanium alloy with starting lamellar microstructure”. In: *Materials Science and Engineering: A* 548 (2012), pp. 6–11.

[144] Stefania Bruschi, Rachele Bertolini, and Andrea Ghiotti. “Coupling machining and heat treatment to enhance the wear behaviour of an Additive Manufactured Ti6Al4V titanium alloy”. In: *Tribology International* 116 (2017), pp. 58–68.

[145] Lisa Biasetto et al. “Polymer-derived sphene biocoating on cp-Ti substrates for orthopedic and dental implants”. In: *Surface and Coatings Technology* 301 (2016), pp. 140–147.

[146] A Jemat et al. “Effects of TiO2 on microstructural, mechanical properties and in-vitro bioactivity of plasma sprayed yttria stabilised zirconia coatings for dental application”. In: *Ceramics International* 44.4 (2018), pp. 4271–4281.

[147] Hyung-Jun Kim and Young-Gak Kweon. “Elastic modulus of plasma-sprayed coatings determined by indentation and bend tests”. In: *Thin Solid Films* 342.1-2 (1999), pp. 201–206.

[148] AAG Bruzzone et al. “Advances in engineered surfaces for functional performance”. In: *CIRP annals* 57.2 (2008), pp. 750–769.

[149] Ajay Malshe et al. “Bio-inspired functional surfaces for advanced applications”. In: *CIRP Annals* 62.2 (2013), pp. 607–628.

[150] WP Dong, PJ Sullivan, and KJ Stout. “Comprehensive study of parameters for characterising three-dimensional surface topography: IV: parameters for characterising spatial and hybrid properties”. In: *Wear* 178.1-2 (1994), pp. 45–60.

[151] Yilei Zhang and Sriram Sundararajan. “The effect of autocorrelation length on the real area of contact and friction behavior of rough surfaces”. In: *Journal of applied physics* 97.10 (2005), p. 103526.

[152] Dinakar Sagapuram et al. “Deformation temperature effects on microstructure and texture evolution in high strain rate extrusion-machining of Mg-AZ31B”. In: *Materials Science Forum*. Vol. 1517. 702. 2011, p. 52.

[153] M Alvarez-Lopez et al. “Corrosion behaviour of AZ31 magnesium alloy with different grain sizes in simulated biological fluids”. In: *Acta Biomaterialia* 6.5 (2010), pp. 1763–1771.

[154] KD Ralston and N Birbilis. “Effect of grain size on corrosion: a review”. In: *Corrosion* 66.7 (2010), pp. 075005–075005.

[155] Camillus Sunday Obayi et al. “Effect of grain sizes on mechanical properties and biodegradation behavior of pure iron for cardiovascular stent application”. In: *Biomatter* 6.1 (2016), e959874.

[156] Naing Naing Aung and Wei Zhou. “Effect of grain size and twins on corrosion behaviour of AZ31B magnesium alloy”. In: *Corrosion Science* 52.2 (2010), pp. 589–594.

[157] M Andrei et al. “DC and AC polarisation study on magnesium alloys Influence of the mechanical deformation”. In: *Materials and corrosion* 53.7 (2002), pp. 455–461.

[158] H Nouri Hosseinabadi, SA Sajjady, and S Amini. “Creating micro textured surfaces for the improvement of surface wettability through ultrasonic vibration assisted turning”. In: *The International Journal of Advanced Manufacturing Technology* (2018), pp. 1–15.